POLITECNICO DI MILANO

School of Industrial and Information Engineering

DEPARTMENT OF ENERGY

MASTER OF SCIENCE IN NUCLEAR ENGINEERING

NUMERICAL INVESTIGATION OF NUCLEAR FUSION RELEVANT PLASMAS IN LINEAR DEVICES THROUGH THE SOLPS-ITER CODE

Advisor:
Prof. Matteo Passoni

Co-Advisor:
Dr. Andrea Uccello

Graduation thesis of:
Elena Tonello
878358

ACADEMIC YEAR 2017-2018

ABSTRACT

The use of increasingly sophisticated numerical codes to simulate complex physical phenomena such as those happening in boundary plasma of magnetic devices, finds always more room in the framework of magnetic confinement nuclear fusion research (MFC). In this thesis work, the latest version of the SOLPS (Scrape-Off Layer Plasma Simulator) code, namely SOLPS-ITER, has been applied to simulate plasma characteristics of the linear magnetic confinement system GyM of IFP-CNR. The exploitation of this kind of code to simulate linear plasma devices has been only seldom exploited in the past, if compared to the much more extended literature on tokamak applications. Nevertheless, these studies are of keen interest among the international nuclear fusion community, since the importance of these machines in the study of plasma-wall interaction (PWI) and other edge plasma phenomena.
This thesis work shows the concrete possibility to apply this code to linear geometries, with plasma densities and fluxes much lower than those typically simulated in tokamaks and other linear devices. Both the fluid and fluid-Monte Carlo coupled versions of SOLPS-ITER have been used so simulate argon and deuterium plasmas. The standalone fluid mode has been employed to address numerical issues, such as convergence and the effects of spatial and temporal discretization, while in coupled fluid-Monte Carlo mode, sensitivity analysis of different physical parameters of the code, e. g. neutral density, radial transport coefficients and external power, have been done. The thus obtained results, although they have to be considered preliminary achievements, are in good agreements with experimental data.

SOMMARIO

L'impiego di codici numerici sempre più sofisticati per simulare fenomeni fisici complessi come quelli che avvengono nel plasma di bordo in macchine a confinamento magnetico, sta trovando sempre più spazio nel contesto della ricerca sulla fusione nucleare a confinamento magnetico (MCF). In particolare all'interno di questo lavoro di tesi, l'ultima versione del codice SOLPS (Scrape-Off Layer Plasma Simulator), chiamata SOLPS-ITER, è stata usata per simulare le caratteristiche del plasma generato dalla macchina lineare a confinamento magnetico GyM di IFP-CNR. L'applicazione di questi codici a macchine lineari, anche se ad oggi ha trovato limitata applicazione in confronto a quanto sviluppato nel caso di tokamak, trova interesse da parte della comunità scientifica internazionale, data l'importanza di questa classe di devices per lo studio dell'interazione plasma-prima parete (PWI) ed altri fenomeni che avvengono nel plasma di bordo.
Questo lavoro di tesi dimostra la possibilità di applicare questa tipologia di codici a macchine con geometria lineare e con caratteristiche di densità di plasma e flussi di particelle molto inferiori rispetto a quelle tipicamente simulate nel caso di tokamak e altre macchine lineari. Il codice è stato utilizzato in entrambe le sue versioni, fluido e fluido/Monte Carlo, per simulare plasmi di argon e di deuterio. La versione fluida *standalone* è stata utilizzata per studiare aspetti di carattere numerico, come la convergenza del codice e gli effetti di discretizzazione spaziale e temporale, mentre nella versione accoppiata fluido/Monte Carlo, sono state fatte analisi di sensitività sia variando parametri fisici del sistema, come la densità di neutri, la potenza e i coefficienti di trasporto radiali. I risultati ottenuti, seppur frutto di un'indagine ancora preliminare, risultano essere in buon accordo con i dati sperimentali disponibili.

ESTRATTO

Nel quadro attuale di continua crescita della domanda energetica mondiale, l'energia nucleare deve essere considerata uno strumento fondamentale in vista della necessità di soddisfare la richiesta di energia elettrica in modo pulito, sostenibile ed affidabile. In particolare, da decenni la comunità scientifica internazionale si interroga sulla possibilità di sfruttare l'energia prodotta dalla fusione nucleare di nuclei leggeri attraverso un processo noto come *fusione termonucleare controllata*. In questo contesto, la strategia più studiata prevede l'utilizzo come combustibile di una miscela di deuterio e trizio allo stato di *plasma*. Il plasma, considerato il quarto stato della materia oltre a solido, liquido e gassoso, si viene a formare quando ad un gas inizialmente neutro viene fornita sufficiente energia affinché avvenga il processo di ionizzazione degli atomi che lo compongono. Il risultato è uno stato in cui elettroni, ioni molecolari ed atomici ed atomi neutri interagiscono tra loro. Le proprietà peculiari di questo stato della materia sono legate alle interazioni elettromagnetiche tra le particelle cariche che lo compongono, le quali danno logo a fenomeni di tipo collettivo tipicamente assenti negli altri stati di aggregazione.
La fusione di nuclei ionizzati di idrogeno tuttavia è un processo tutt'altro che banale dal momento che è necessario portare le due particelle a distanze tali per cui la forza nucleare che media la reazione di fusione vinca la repulsione Colombiana. Perché ciò avvenga è necessario somministrare al sistema enormi quantità di energia che si traducono in un aumento della temperatura del plasma al di sopra dei 100 milioni di gradi centigradi. Volendo sfruttare questo processo in modo controllato, è necessario individuare una strategia di confinamento in grado di comprimere il plasma a densità sufficientemente elevate affinché si inneschi il processo di fusione. A riguardo, due diverse strategie di confinamento sono state principalmente studiate negli anni: la fusione nucleare a confinamento inerziale (ICF) e quella a confinamento magnetico (MCF). La fusione a confinamento magnetico, contesto all'interno del quale si sviluppa questo lavoro di tesi, prevede l'utilizzo di intesi campi magnetici per confinare il plasma all'interno della camera del vessel. In particolare sono state studiate due configurazioni di campo magnetico: i così detti, sistemi a configurazione aperta e chiusa. Tali definizioni fanno riferimento alla topologia delle linee di campo magnetico, le quali sono rispettivamente aperte, solitamente comprese tra due superficie solide, oppure chiuse, nel senso che si avvolgono infinitamente su se stesse, ricoprendo una regione di spazio di forma toroidale. Alla prima classe di sistemi magnetici appartengono le macchine lineari in configurazione *magnetic mirror*. L'impiego di questo tipo di macchine al fine della realizzazione di un reattore a fusione nucleare è largamente superato al giorno d'oggi. I due sistemi

più promettenti per quanto riguarda il confinamento del plasma sono dunque rappresentati da sistemi chiusi di forma toroidale e sono tokamak e stellarator. In particolare il *tokamak*, il cui nome è l'acronimo russo per *camera toroidale con bobine magnetiche*, è ad oggi la configurazione più studiata da questo punto di vista. A questo proposito, la comunità scientifica internazionale che si occupa di fusione nucleare sta impiegando vaste risorse nella realizzazione del progetto ITER, *la via* in latino. Si tratta del più avanzato e imponente tokamak mai costruito ed ha l'obiettivo di essere il primo reattore sperimentale in grado di produrre un guadagno di energia termica pari ad un fattore dieci rispetto all'energia assorbita dal plasma. È infatti importante notare che in qualsiasi schema d'interesse per produrre energia elettrica attraverso reazioni di fusione nucleare, il reattore è progettato per funzionare da amplificatore di energia in quanto il riscaldamento e la compressione del plasma richiedono l'assorbimento di ingenti quantità di energia.

Lo studio del comportamento del plasma all'interno dei tokamak ha presto messo in evidenza che il confinamento delle particelle cariche nella direzione ortogonale alle superfici di campo magnetico è molto più imperfetto di quanto ci si aspettasse. Sin dai primi esperimenti su questo tipo di macchine infatti, si è riscontrato che la diffusione del plasma in direzione radiale è caratterizzato da coefficienti di trasporto alcuni ordini di grandezza superiori a quelli calcolati con modelli di trasporto classici. Per questo motivo, si parla di *teoria del trasporto anomala*. Tale fenomeno ha portato al riconoscimento che ai fini di un adeguato confinamento e riscaldamento del sistema, la regione più esterna del plasma ricopre un ruolo di cruciale importanza. Le particelle che si trovano in questa regione, infatti, possono impattare contro la parete solida della camera da vuoto all'interno della quale il plasma è contenuto, causandone l'erosione per sputtering. La generazione di impurità a seguito dell'erosione della *prima parete* del vessel e la loro conseguente diffusione all'interno del plasma, comporta una rapida dissipazione di energia attraverso processi radiativi, i quali diminuiscono fortemente la temperatura del sistema. Una profonda ed accurata comprensione dei fenomeni che avvengono nella ragione di bordo plasma, indicata in questo contesto come *scrape-off layer (SOL)*, è dunque di fondamentale rilevanza ai fini della realizzazione stessa del processo di fusione. L'indagine sia teorica che sperimentale di questi fenomeni e dei meccanismi d'interazione tra plasma e prima parete (*plasma-wall interaction, PWI*) è dunque largamente incentivata.

Per quanto riguarda l'aspetto teorico/numerico sono stati messi a punto complessi codici numerici in grado di simulare il trasporto del plasma di bordo. In particolare, questi codici sono stati ideati ed applicati per supportare l'attività sperimentale su tokamak attuali e, a scopo predittivo, per simulare i flussi di particelle che saranno raggiunti nei futuri reattori. Tali modelli numerici sono tipicamente basati sull'accoppiamento di codici per la descrizione del plasma in approssimazione fluida e codici cinetici per contemplare le interazioni tra

plasma e particelle neutre. La trattazione fluida delle diverse specie cariche presenti nel plasma prevede la risoluzione di equazioni di conservazione per densità, momento e temperatura per ciascuna specie, mediante metodi a volumi finiti. Il modello fluido adottato utilizza coefficienti di trasporto in direzione parallela a **B** ottenuti in ambito di una *teoria del trasporto classico*, mentre in direzione ortogonale alle superfici di campo magnetico, in assenza di una teoria consistente, i coefficienti di diffusione sono tipicamente utilizzati come parametri liberi. In aggiunta questi codici offrono la possibilità di simulare contemporaneamente diverse specie ioniche, al fine di tenere in considerazione anche le impurezze presenti nel plasma. Questo è importante sia per capire l'effetto delle particelle erose per sputtering, sia per investigare l'efficacia, in termini di attenuazione dei flussi termici in direzione della parete, di impurezze di gas neutro iniettate nella camera. Per quanto riguarda la trattazione del trasporto e dell'interazione delle particelle neutre presenti nel plasma, i codici cinetici impiegati utilizzano metodi Monte Carlo per stimare l'effetto di reazioni di ionizzazione, scattering e scambio di carica sui termini di sorgente delle equazioni fluide.
Dal punto di vista sperimentale, lo studio dei fenomeni che avvengono nel plasma di bordo vengono studiati mediante campagne sperimentali sugli attuali tokamak, oppure piuttosto frequentemente vengono costruite delle macchine a configurazione magnetica aperta, che abbiano lo scopo primario di studiare la PWI o altri fenomeni fisici importanti come il riscaldamento del plasma, il trasporto turbolento e la realizzazione di sistemi di diagnostica. L'introduzione di macchine di questo tipo, comunemente chiamate *macchine lineari* offre il vantaggio di poter ottenere a costi piuttosto ridotti condizioni di plasma che saranno tipiche dei futuri sistemi per la fusione nucleare e che al contrario non sono raggiunte nei tokamak attuali.

La motivazione fondamentale alla base di questo lavoro è il tentativo di sfruttare i codici numerici sviluppati per descrivere il SOL dei tokamak, applicandoli a macchine lineari. Indagini di questo tipo stanno incontrando crescente interesse, vista la notevole importanza di questa configurazione magnetica nello studio di fenomeni di bordo plasma e della PWI. In particolare, in questo contesto il l'ultima versione del codice SOLPS (Scrape Off-Layer Plasma Simulator), chiamata SOLPS-ITER, è stata applicato alla macchina lineare *GyM*. Questo progetto è stato svolto nell'ambito di una collaborazione tra il Politecnico di Milano e l'*Istituto di Fisica del Plasma (IFP)* del CNR, dove GyM è stato progettato e costruito.
L'obiettivo primario del lavoro svolto è stato dimostrare l'applicabilità del codice SOLPS-ITER su geometrie lineari ed in particolare per le condizioni di *medium-flux* che si riescono ad ottenere in GyM. Densità di plasma e flussi di particelle per questa macchina sono infatti diversi ordini di grandezza inferiori a quelli usualmente simulati sia in tokamak che in altre macchine lineari esistenti nel contesto internazionale. Basse densità di plasma comportano in generale

un allungamento dei liberi cammini medi delle particelle e minori frequenze di collisione. Questo a sua volta implica che alcune delle approssimazioni fatte dal codice valgano in maniera più limitata e vadano testate specificamente.
In virtù degli obiettivi appena esposti, è stato necessario in primo luogo conoscere il codice e le equazioni in esso implementate studiando la letteratura disponibile. Per comprendere aspetti più tecnici, si è riprodotto un caso di benchmark del tokamak Asdex UpGrade (AUG) proposto come esempio dagli sviluppatori del codice. Nel presentare i risultati si questa simulazione di test, ci si è concentrati soprattutto sull'andamento della convergenza del codice nelle due versioni fluida-standalone ed accoppiata. In particolare si è visto come i residui delle equazioni fluide convergano alla precisione di macchina nel caso standalone, mentre questo non sia possibile nel caso accoppiato a causa del rumore statistico intrinseco delle simulazioni Monte Carlo. Per appurare la convergenza del codice in questa modalità di utilizzo, si preferisce dunque guardare il raggiungimento del bilancio di particelle ed energia nel sistema mediante script appositamente implementati all'interno del codice. La convergenza si considera realizzata quando la somma delle sorgenti positive e negative di particelle ed energia raggiunge un valore nullo e stabile nel tempo. In particolare, l'oscillazione del bilancio di particelle attorno allo zero stima le fluttuazioni statistiche legate al utilizzo di metodi Monte Carlo.
Per quanto riguarda aspetti specificamente legati all'applicazione del codice a GyM, per prima cosa è stato necessario introdurre e descrivere le caratteristiche fondamentali della macchina, con riferimento alla configurazione magnetica di equilibrio e alle caratteristiche della sorgente di plasma. Il campo magnetico all'interno della macchina è stato calcolato in approssimazione di *magnetoidrodinamica (MHD) ideale* ed è servito per costruire la griglia computazionale utilizzata dal codice fluido. Questa è formata da celle di forma rettangolare in cui due dei lati sono allineati con la direzione delle linee di forza del campo magnetico. Tale griglia deve estendersi tra le due basi del cilindro, senza intersecare le pareti laterali della macchina. Al contrario, la griglia a celle triangolari per le simulazioni accoppiate si estende in tutta la regione interna alla macchina e per costruirla è stato necessario definire i segmenti corrispondenti alle pareti della camera, includendo anche i dotti delle pompe e del misuratore di pressione. Per simulare il flusso di particelle in ingresso, si è considerata un'ulteriore superficie trasparente posta a ridosso di una delle basi del cilindro in corrispondenza della posizione dell'ugello per l'immissione di gas in camera. È importante sottolineare che la possibilità di definire questo tipo di superfici per il gas puffing internamente alla griglia fluida è stata implementata solamente in SOLPS-ITER ed è stata una delle principali ragioni per cui si è scelto di utilizzare questa versione del codice piuttosto che le precedenti.
Un altro punto importante nella descrizione di GyM è legato al modo in cui la sorgente di plasma è modellizzata ed implementata come input del codice. Quando un'onda elettromagnetica con frequenza pari alla frequenza ciclotron-

ica $\nu = eZB/2\pi m$ si propaga all'interno di un plasma magnetizzato, si verifica un efficace trasferimento di energia dall'onda al plasma. Questo meccanismo è chiamato *risonanza ciclotronica* elettronica (ECR) o ionica (ECI), rispettivamente se la frequenza d'interesse è quella del moto di girazione attorno al campo magnetico di elettroni o ioni. In GyM, la cui sorgente emette a 2.45 GHz, questo si verifica quando il campo magnetico assume il valore di $B_{res} = 0.0875\,\mathrm{T}$, corrispondente al valore risonante per gli elettroni. Il fenomeno di ECR, considerato l'unico meccanismo attivo in grado di trasferire energia al plasma, è stato modellizzato nelle simulazioni descritte in questo lavoro, come un termine di sorgente esterno nell'equazione per la temperatura elettronica la cui forma sul dominio del plasma rispecchia l'andamento della linea di campo a $B(\mathbf{x}) = B_{res}$. Parte di questo lavoro di modellizzazione si è basato su una precedente esperienza di applicazione del codice SOLPS 5.1 a GyM [48], tuttavia si è arricchito il grado di conoscenza legato alla costruzione della mesh sia per il codice fluido che per quello accoppiato e si è migliorato il modeling della sorgente.
Una volta che il lavoro preliminare di *modeling* del sistema è stato portato a termine, sono state svolte simulazioni di plasmi di argon e deuterio, utilizzando sia la versione fluida del codice che quella accoppiata. L'obiettivo primario di tali simulazioni è stato quello di comprendere gli effetti sulle caratteristiche del plasma di parametri di natura numerica e fisica, opportunamente variati all'interno degli input del codice. In generale, in tutte le simulazioni è stata considerata una sola specie di plasma, senza impurezze o stati di carica multipli. Inoltre, sono stati trascurati i termini di *drift* nelle equazioni fluide.
La prima serie di simulazioni svolte aveva l'obiettivo di descrivere plasmi di argon, considerando solamente la parte fluida del codice e trascurando gli effetti di pompaggio e puffing delle specie neutre. In questo caso, la situazione fisica descritta è chiaramente influenzata dalle condizioni iniziali scelte, poiché il numero di particelle all'interno del sistema è arbitrariamente fissato. Per questo motivo, tali simulazioni sono state usate per comprendere aspetti di carattere numerico del codice piuttosto che utilizzarle come strumento per cogliere l'evoluzione fisica del sistema. In questo contesto, sono stati valutati aspetti legati alla convergenza della soluzione, riuscendo a portare i residui delle equazioni fluide vicino alla precisione di macchina, e si è indagato l'effetto dei parametri di discretizzazione temporale e spaziale del codice, con l'obiettivo di fissare passo temporale e dimensione della griglia ottimali. Inoltre, partendo dalle medesime condizioni fisiche iniziali, si sono confrontati risultati di due simulazioni ottenute con due versioni differenti del codice, specificamente SOLPS-ITER e SOLSP 5.1, mettendo in evidenza le differenze riscontrate.
Per effettuare analisi di sensitività dei parametri fisici, si è invece passati ad utilizzare la modalità accoppiata del codice. A questo proposito si è deciso di simulare plasmi di argon, in quanto la natura atomica del gas in questione semplifica grandemente i processi d'interazione che possono avvenire tra le diverse specie del plasma, comportando per altro una forte riduzione del tempo

computazionale legato alla soluzione del trasporto dei neutri mediante metodo Monte Carlo. I parametri che sono stati modificati riguardano la concentrazioni di neutri nel sistema, la potenza esterna assorbita e il valore dei coefficienti di diffusione radiale. Da queste analisi si è potuto trarre informazioni legate all'andamento delle caratteristiche del plasma, valutando in particolare i profili radiali di temperatura e densità elettronica e potenziale di plasma, al variare dei suddetti parametri fisici. Infine si è proposto un primo confronto tra i risultati delle simulazioni e i dati sperimentali disponibili. L'andamento qualitativo dei profili radiali è stato in buona parte colto dalle simulazioni svolte. Contrariamente a quanto si era riusciti ad ottenere nel precedente lavoro svolto impiegando SOLPS 5.1, i risultati delle simulazioni con SOLPS-ITER sono in buon accordo quantitativo con i dati sperimentali, mostrando discrepanze inferiori ad un fattore 2.
Per verificare l'effettiva applicabilità del codice a situazioni di maggiore interesse in ambito di fusione nucleare, si è infine passati a simulare plasmi di deuterio. La natura molecolare di questo gas arricchisce la varietà di specie che devono essere tenute in considerazione, aggiungendo ioni e neutri di natura molecolare. Questo dilata in modo significativo i tempi computazionali del codice, arrivando fino ad un aumento di due ordini di grandezza per ogni iterazione. I risultati ottenuti dall'unica simulazione effettuata, sono comunque da considerarsi soddisfacenti. Anche in questo caso, nonostante non sia stata effettuata un'analisi di sensitività sui parametri fisici, si è ottenuto un buon accordo con i dati sperimentali con discrepanze inferiori ad un fattore 2.
Per concludere l'analisi delle simulazioni dei plasmi di deuterio, si è verificata a posteriori la validità dell'*approssimazione statica* sugli ioni molecolari, che viene effettuata dal codice Monte Carlo. La natura atomica della parte fluida del codice, non permette infatti di simulare il trasporto di specie come il $D_2{}^+$ mediante l'approssimazione fluida. Tuttavia, tali specie sono importanti in molti dei processi atomici e molecolari che avvengono nel plasma e vanno dunque considerate nella trattazione cinetica. L'approssimazione statica adottata dal codice, assume che il libero cammino medio di queste specie sia nullo così da poterne trascurare il trasporto. Tuttavia, questa approssimazione è valida solo se la densità del plasma di background è sufficientemente alta da rendere sostanzialmente istantaneo il processo di dissociazione del $D_2{}^+$. In questo lavoro, è stato dunque stimato il valore del libero cammino medio di questa specie $\lambda_{D_2^+}$ e confrontato con la dimensione della griglia computazionale, così da verificare la validità dell'approssimazione statica in GyM. Nonostante i risultati ottenuti siano in buon accordo con i dati sperimentali, si è riscontrato che l'approssimazione statica non è in generale valida per la descrizione del plasma in GyM.

CONTENTS

LIST OF FIGURES

LIST OF TABLES

1 INTRODUCTION

In this first introductory chapter a very general overview of nuclear fusion as a source of electric energy is given.
The chapter starts with a brief introduction to the energy problem, in particular referring to the role of nuclear energy in the foreseen scenario of increasing energy demand. To conclude section 1.1, the different approaches of nuclear fission and nuclear fusion are introduced.
In section 1.2, a more detailed overview of thermonuclear fusion is given. First the fusion reaction is introduced from a physical point of view (§1.2.1), introducing also the concept of plasma state, then the fusion reactor scheme is described (§1.2.2), pointing out also the various contribution to the thermal and electric power balance (§1.2.3). In this context, the source and sink terms of the thermal energy balance are related to the plasma properties, such as temperature and density. Finally, the two plasma confinement approaches of inertial and magnetic confinement are described (§1.2.4).

1.1 NUCLEAR ENERGY

The identification of new energy sources to produce energy in a sustainable and reliable way is the fundamental challenge of our generation. Energy is essential for almost all human activities, from food production and heating to operating industrial facilities and providing transportation. If from one side an increasing energy demand is a sign of an increased standard of living, on the other hand it is clear that to ensure the correct operation of our society, a reliable supply of energy is increasingly essential.
Figure 1 shows the results of the *Annual Energy review* [2] compiled by the U.S. Energy Information Administration (EIA), monitoring the primary energy consumption by source per year from the Fifties up to 2017. We can see that energy consumption is almost tripled in the past fifty years and moreover projections forecast that this trend will continue for the next years. Concerns that this steadily increasing demand for new energy production is more than what we can met in an economically feasible and environmentally friendly manner within the existing portfolio of options are nowadays part of the public discussion.
In this scenario of increasing energy demand, nuclear energy should be considered of primary interest as a clean, sustainable and reliable source of energy.

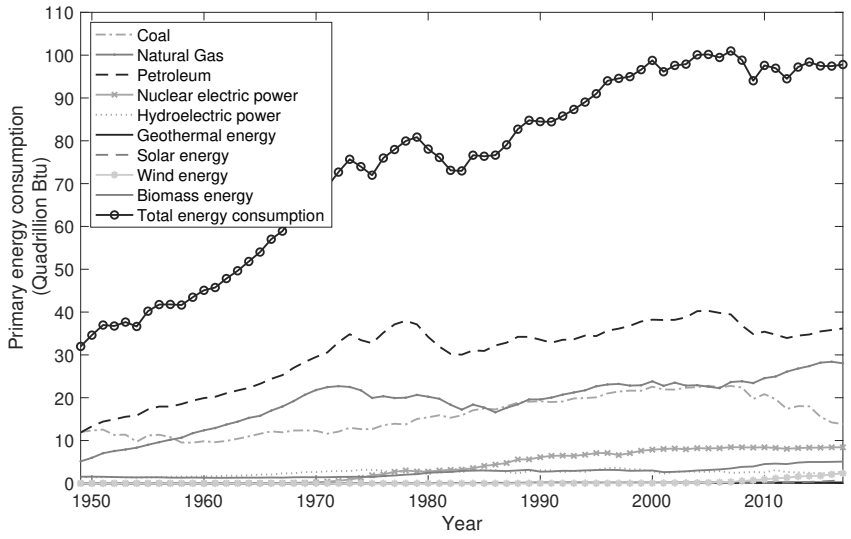

Figure 1: Evolution of the primary energy consumption in quadrillion Btu, from 1949 to 2017. One quadrillion Btu ($= 1 \times 10^{15}$ Btu) corresponds to 1.055×10^{18} J or 33.434 GW y [2].

One of the most appealing characteristics of nuclear energy is its huge intrinsic energy density. Comparing with traditional chemical combustion reactions, nuclear reactions produce on the order of one million times more energy per particle involved in the process. This has clear advantages both on the mass of fresh fuel needed to produce a given amount of energy, but also on the volume of wastes produced.

From the physical point of view, this enormous difference in the energy density is related to the nature of the interaction involved in the two processes.

In a chemical reaction, as it is combustion, bounds between electrons and nuclei are broken. Typical order of magnitude for the binding energy associated to this electromagnetic interaction is around few eV. In a nuclear reaction on the contrary, the interaction that we have to consider is the strong nuclear force among protons and neutrons, which in this context are usually called *nucleons*. This interaction is much more intense than the electromagnetic force and moreover it has a very short range, of the order of $\sim 10^{-15}$ m[1], resulting in a binding energy of the order of one MeV per bound.

In figure 2 the nuclear binding energy per nucleon is plotted as a function of the mass number A for each element. We can see that this quantity has a maximum for A between 40 u and 60 u. To a very elementary level, we can say

1 The *femtometer* fm $= 10^{-15}$ m is usually called *Fermi* in nuclear physics. It is the typical length scale of both the strong nuclear interaction and the nuclear dimension. The name is of course chosen in honor to Enrico Fermi, who gave major contribution in many nuclear science topics.

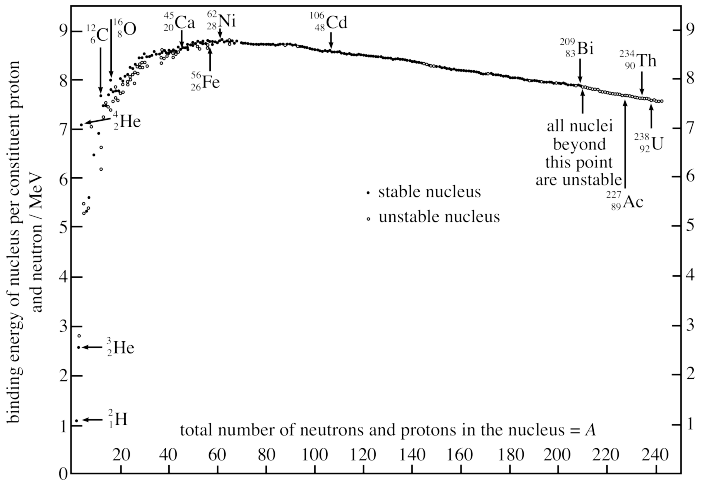

Figure 2: Nuclear binding energy per nucleon as a function of the number of nucleons in the nucleus.

that a reaction, being chemical or nuclear, is exothermic when the products are more stable than the reactants, or with reference to the curve in figure 2, when the reaction evolves toward the maximum. Again referring to the same figure, it is evident that two paths can be followed to reach the maximum and so to release energy from the reaction: starting from the lightest nuclei, merging them together exploiting a *nuclear fusion reaction*, or starting from heavy elements splitting them into tow or more fragments in what is called *nuclear fission reaction*.

Up to now, all the commercial electrical power produced by nuclear reactions has been obtained exploiting the fission induced by neutrons of heavy elements, mainly uranium. The use of neutrons to promote fission reactions was first proposed by Enrico Fermi and his studies, in particular on thermal neutrons, led to the construction and operation of the first nuclear reactor, the *Chicago Pile-1 (CP-1)*, in December 1942.
The fission cross section for ^{235}U and ^{239}Pu as a function of neutron energy is reported in figure 3a. We can clearly see the $\sim 1/v$ behaviour of the cross section in the thermal energy region, below 0.1 eV, and the resonant behaviour for higher neutron energies. Today both thermal and fast neutrons are exploited in fission nuclear reactors.
The key feature of nuclear fission reactor is the possibility of self-sustain a chain reaction, so that no external power has to be supplied once the reaction has been started. This is possible providing a balance among the neutrons needed to fission a given mass of fuel, the neutrons produced by the fission reactions and the neutron losses, both from absorption and leakage from the reactor. Once this balance is reached, the reactor is said to be *critical*, the produced power is stationary and no external energy source is needed. As we will see the

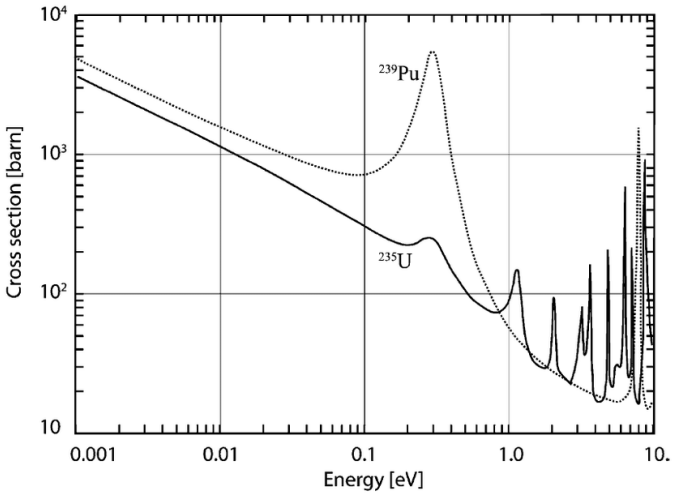

(a) *Nuclear fission cross section as a function of neutron energy from [79]. The kinetic energy E, considering nuclei at rest, is related to neutron velocity v by $E = 1/2 m_n v^2$.*

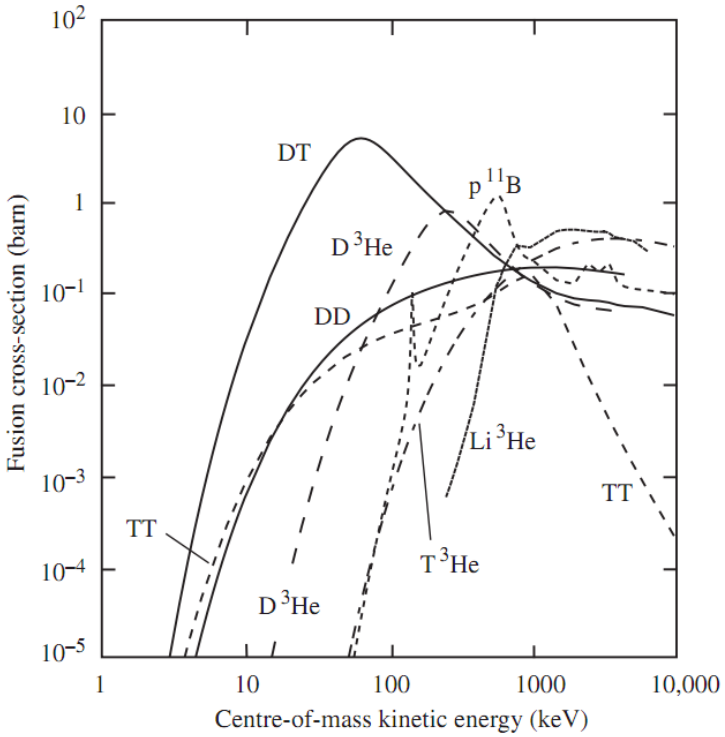

(b) *Nuclear fusion cross section as a function of the center of mass kinetic energy from [57]. This is more commonly expressed in terms of plasma temperature.*

Figure 3: Cross section for fission and fusion nuclear reactions. It is interesting to note the paramount difference in both the cross-section values and the energy spectra of interest for the two reactions.

current prototype of fusion reactor will be quite different with respect to all these features.
For what concerns the operational condition of a fission reactor[2], they are not much different from a conventional reactor regarding pressure and temperature. On the other hand, peculiar considerations in the choice of materials must be paid, in particular to achieve a satisfactory overall neutron economy needed to reach criticality.

1.2 NUCLEAR FUSION

The other possibility to produce energy exploiting nuclear reactions, that is by fusing light nuclei together, will be considered in this section. We will see that the conditions needed to operate a fusion reactor are unique to this kind of device and need to overcome the very difficult scientific and engineering challenges that are inherent in the fusion process. Even if we are still far away from producing the first commercial electric *kilowatt* of power by nuclear fusion, the benefits that this source of energy could give make fusion research one of the most active research topics of our time.

1.2.1 *Nuclear fusion physics*

We have seen that nuclear fusion is a nuclear reaction where two light nuclei merge together giving a heavier and more stable nucleus, together with the release of other particles and energy. In principle, as we can see from figure 2, all nuclei up to ^{56}Fe can undergo exothermic fusion reaction, however only few of them are considered feasible to be exploited in the construction of a reactor. To understand why, we have to consider that when two positive charged particles, like two nuclei, has to be fused together, the Coulomb barrier has to be overcome. This barrier is proportional to the square of the nuclear charge, hence the lightest nuclei are the first candidates to fulfill our purposes. This is why, the most studied reactions mainly use hydrogen and its isotopes as reactants:

$$\begin{aligned} \mathrm{D} + \mathrm{D} \quad &\rightarrow \quad \begin{cases} {}^{3}\mathrm{He} + n + 3.27\,\mathrm{MeV} & b.r. = 0.5 \\ \mathrm{T} + \mathrm{H} + 4.03\,\mathrm{MeV} & b.r. = 0.5 \end{cases} \\ \mathrm{D} + {}^{3}\mathrm{He} \quad &\rightarrow \quad {}^{4}\mathrm{He} + \mathrm{H} + 18.3\,\mathrm{MeV} \\ \mathrm{D} + \mathrm{T} \quad &\rightarrow \quad {}^{4}\mathrm{He} + n + 17.6\,\mathrm{MeV} \end{aligned} \tag{1}$$

2 In this discussion we are considering a standard PWR (pressurized water reactor), which nowadays represents the most common nuclear power plant technology in the world. Typical working conditions for the primary circuit are pressure of 155 bar and maximum water temperature slightly above 300 °C.

The cross sections for this and others reactions are reported in figure 3b. From this figure we can understand one of the challenging features of the fusion process. Let's consider, for instance, the D-T process: the cross section is orders of magnitude less than the fission ones and moreover it shows a sharply increasing behaviour with energy up to around 50 keV, completely opposite to the $\sim 1/\sqrt{E}$ behaviour of fission. Consequently, high reactants energies are required in order to make the reaction interesting for applications.
The fusion cross section, as we have already mentioned, is strongly affected by the Coulomb repulsion. In a quantum mechanical picture, the possibility of tunneling this potential barrier plays an important role in the overall fusion probability. It is for this reason that the usual dependence [41] of the cross section contains the so-called exponential *Gamow factor*, which represents indeed the transparency factor of the Coulomb barrier:

$$\sigma(E) = \frac{1}{E} S(E) e^{-\sqrt{G_E/E}} \tag{2}$$

here $S(E)$ is the so-called *astrophysical S-factor* and, for most of the reaction of interest, is slowly varying with E, while G_E is the *Gamow energy* and it is proportional to the square of the nuclear charges.

The vast majority of research in the nuclear fusion field is directed towards thermonuclear fusion. By this we refer to a scheme where the fuel is in *plasma state* and the required high energy conditions we have just described are reached by heating up the plasma to suitable temperatures.
A *plasma* is a partially or completely ionized gas, made of electrons, ions and neutral particles interacting with each other. Differently from the other states of matter, interactions among charged particles in a plasma are dominated by collective phenomena, originated from the electromagnetic fields present in the ionized gas. Indeed, charge separation between ions and electrons gives rise to electric fields, and charged particle flows give rise to currents and magnetic fields. The description of these electromagnetic phenomena then is an integral part of the plasma modeling and their effects on the plasma properties are considered characteristic features of this state.
When we want to describe binary interactions between two particles in a plasma, such as in a D−Tfusion reaction[3], the process can generally be written as:

$$A + B \rightarrow C + D \tag{3}$$

where B is called *probe particle* and it is usually considered mono-energetic with energy E_0, and A is the *bulk particle*, which represents the background

3 This discussion, anyway, is quite general and it does not apply only to fusion reactions. As we will see in the following, in particular in section 2.3.2, many types of binary interactions between charged and neutral species have to be considered also in non ignited plasmas.

plasma species onto with the probe collides. Background species is supposed to be described by a *Maxwellian distribution functions*:

$$f_A(\mathbf{v}) = f^{Max}(\mathbf{v}) = n_A \left(\frac{m_A}{T_A \pi}\right)^{3/2} \exp\left\{-\frac{m_A(v_x^2 + v_y^2 + v_z^2)}{2T_A}\right\} \tag{4}$$

where the temperature T_A has been defined as[4]:

$$\frac{3}{2} n_{e,i} T_A = \frac{1}{2} m_A \int (v_x^2 + v_y^2 + v_z^2) f^{Max}(\mathbf{v})_A d\mathbf{v} \tag{5}$$

In case any non-null forces act on the plasma background, the distribution function can still be represented by a Maxwellian, but with a non-null drifting velocity $\mathbf{v}^{Drift} = a_x \mathbf{u}_x + a_y \mathbf{u}_y + a_z \mathbf{u}_z$. We call this moving Maxwellian a *drifting Maxwellian distribution functions*:

$$f^{Max}(\mathbf{v})_A = n_A \left(\frac{m_A}{T_A \pi}\right)^{3/2} \exp\left\{-\frac{m_A[(v_x - a_x)^2 + (v_y - a_y)^2 + (v_z - a_z)^2]}{2T_A}\right\} \tag{6}$$

The rate coefficient $\langle \sigma v \rangle$, i. e. the proportionality constant between the collision frequency ν_{AB} and the bulk specie density n_A, for a given reaction is obtained averaging the cross section over the distribution function of the bulk specie.

$$\langle \sigma v \rangle = \int \sigma(v) v f_A^{Max}(v_r) dv_r \tag{7}$$

In case neither of the two reactants can be considered at rest, the velocity to be considered Maxwellian distributed is their relative velocity v_r. The $\langle \sigma v \rangle$ obtained in this way is, in the simplest case, only a function of the temperature of the bulk species. Rate coefficients are used to estimate the number of reaction of type (3) that occurs per unit volume per unit time. The reaction rate R_{Rate} is given by:

$$R_{Rate} = n_A n_B \langle \sigma v \rangle \tag{8}$$

where n_A and n_B are respectively the number of particles of type A and B in the unit volume considered. The fusion rate coefficients $\langle \sigma v \rangle_{Fus}$, for reactions (1) and other reactions are reported in figure 4. As we can see, to have a sufficiently high reaction rate, background plasma temperature around 10 keV, which corresponds to more than a hundred million Celsius degrees, as to be reached. From this curves, it is also clear that, in terms of both temperature and reactions per second, the most promising reaction is the D–T reaction.

4 The same definition is used also when only *near local thermodynamic equilibrium (LTE)* conditions apply. Issues related plasma description near LTE are discussed in section 2.4.2, when the Braginskii plasma model is described.

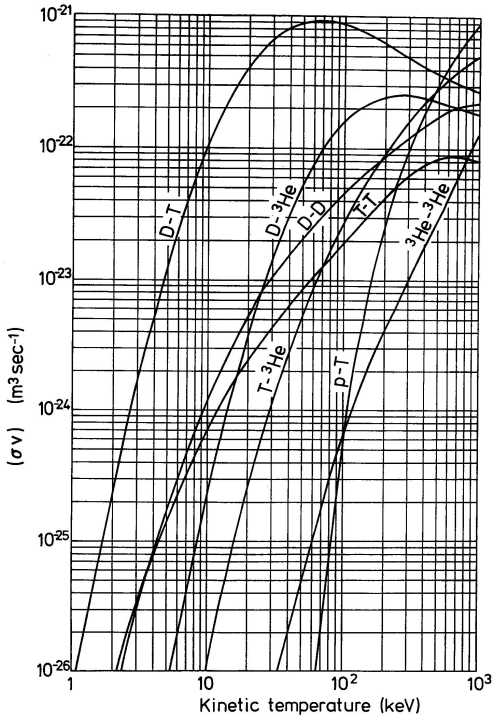

Figure 4: Rate coefficients $\langle \sigma v \rangle_{Fus}$ for different fusion reactions.

Peculiar difficulties related to the use of tritium as fuel has anyway to be considered. As it is well known, tritium is a radioactive isotope of hydrogen, with half life of 12.33 y, for this reason it is extremely rare on Earth and it has to be produced in some way to be used as fuel. Moreover, it is extremely permeable and so radiation protection limits on the concentration of this isotopes are imposed by the Nuclear Regulatory Commission [15]. Of course, dealing with only deuterium would have spare this problems but the much lower reaction rates for D−D reaction makes it completely unfeasible.
A possible solution for the tritium production will be described in section 1.2.2, after the scheme for a fusion reactor will be presented.

This very simplified description of D-T thermonuclear fusion already allows to understand that the conditions under which a fusion reactor would work are extremely different from any other device. To initiate the fusion reaction, in fact, temperatures above hundred million degrees are to be reached, making the fusion core plasma the hottest plasma that has ever been artificially produced on Earth. The basic physical features of nuclear fusion that we have just described, are used in section 1.2.2, where the scheme for a thermonuclear reactor is described, introducing the various elements, which allows to convert the energy produced by the nuclear reaction into electric power.

1.2.2 *Nuclear fusion power plant*

The aim of this section is to describe how the energy produced by fusion reactions is recovered and converted into electric power.
Considering very elementary momentum and energy balance for the D – T reaction, we can see that 4/5 of the total energy produced per reaction, equal to 14.1 MeV, is kept by the neutron and only 3.5 MeV by the ^{4}He nucleus. The idea, then, is to recover the kinetic energy of neutrons, converting it first into heat and then into electrical work by means of a thermodynamic cycle. In figure 5 a conceptual scheme for a fusion reactor is shown[5]. Features related to the behaviour of the plasma inside the core will be discussed later, here we want to briefly describe how the reactor works once the fusion reaction is initiated in the core.
To fulfill the first of the two energy conversion steps, i. e. converting neutron kinetic energy into heat, a thick layer of moderating material, called *blanket*, is placed all around the core. Neutrons impinging on the blanket material, transfer their energy via elastic collisions. It is known that neutron moderation is more effective if the moderating atoms are light, for this reason low Z materials are chosen for the blanket. A cooling system is installed in the blanket to remove the heat produced by collisions and convert it into electric energy by means of an ordinary thermodynamic cycle. Also the possibility to have blanket material in liquid form, so that it acts as both moderator and coolant, is being considered.
A very good candidate for a solid blanket material is lithium: it is a good moderator for neutrons since it is very light and moreover both its stable isotopes, ^{6}Li(7,5%) and ^{7}Li(92,5%) reacts with neutrons producing tritium. The two reactions we could exploit are

$$\begin{aligned} {}^6\mathrm{Li} + n &\rightarrow {}^4\mathrm{He} + T + 4.8\,\mathrm{MeV} \\ {}^7\mathrm{Li} + n &\rightarrow {}^4\mathrm{He} + \mathrm{T} + n - 2.5\,\mathrm{MeV} \end{aligned} \tag{9}$$

where the first reaction being exothermic while the second is endothermic. In this scheme, therefore, also the problem of tritium production can be solved.
Of course, showing that this production process is possible and sustainable is one of the key points in the demonstration of the feasibility of nuclear fusion as source of energy.

1.2.3 *Energy balance and Lawson criterion*

After the main features of a fusion reactor have been described in section 1.2.2, the critical issue is to calculate the ratio of the output power to the input power, in order to determine the conditions under which the system indeed

5 From now on we will always refer to schemes based on D-T fusion reaction.

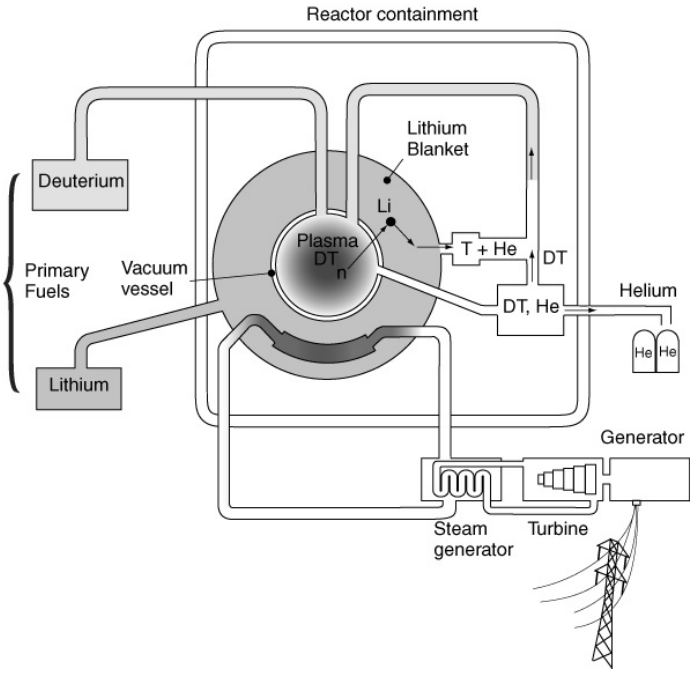

Figure 5: Scheme of a nuclear fusion reactor.

makes sense as a power reactor. We will see that, contrary to what we have said for fission reactor in section 1.1, a fusion reactor can not work unless a large amount of external energy is supplied. A fusion reactor then, actually works as an energy amplifier, exploiting the energy produced by fusion reactions in order to get a net power gain between the external input and the output.

To address the efficiency of this amplification, two dimensionless *gain parameters* are introduced. The first parameter Q is widely used by the fusion community and is based primarily on physics considerations. The second one Q_E is instead more directly connected with the final goal of achieving a net production of electricity and attempts, in a simple manner, to include some basic engineering constraints mainly related to the conversion of thermal power into electric power. The first and more general definition for the two parameters can be given as

$$Q = \frac{\text{net thermal power out}}{\text{heating power in}} \qquad Q_E = \frac{\text{net electric power out}}{\text{electric power in}} \tag{10}$$

The gain parameter Q is essentially telling us the net thermal power produced by the plasma as a result of the physics of the fusion process. In the limit where no fusion reaction takes place, all the input heating power is converted into the total output thermal power in the form of thermal conduction and radiation power losses; in this case the *net thermal power out* which is the dif-

ference between the total output power and the heating power supplied to the plasma is zero and so also $Q = 0$. In the limiting case where no external heat is required to sustain the plasma, the Q factor diverges to infinity. Anyway, although relevant for the plasma energy balance, the physical gain parameter Q is not sufficient to describe a nuclear fusion reactor since none of the contributions to Q is an actual electric power density. The engineering gain factor Q_E remedies this situation by converting all contributions to electric power densities by the introduction of appropriate power conversion efficiencies. The value $Q_E = 0$ corresponds to the so-called *electric power breakeven*, i. e. the condition for which the electric power supplied is equal to the electric power produced and it requires that some energy is produced by the plasma, it must be $Q > 1$. Moreover, the relevant condition under which a power reactor works clearly requires $Q_E > 1$.

In Appendix A, a more detailed derivation of the various terms entering the plasma power balance is given. In particular, relations between plasma parameters, such as density and temperature, and the physical gain parameter Q is given. The main result obtained is the derivation of the *Lawson criterion* [44], which defines the *plasma ignition conditions*.
The Lawson criterion allows to define the conditions under which a plasma, with density n which is confined for a time τ_E, can self-sustain fusion reactions, without the need for external power supply. It requires that, the product $n\tau_E$ is greater than minimum value, which for a D−Tplasma, with temperatures around $T \simeq 25\,\mathrm{keV}$, is $n\tau_E \geq 2 \times 10^{14}\,\mathrm{s\,cm^{-3}}$. When this condition is fulfilled, the plasma is said to be *ignited*.
This criterion moreover, just define the minimum value for the product $n\tau_E$, but no restriction is given on the relative values for the two parameters. Under this consideration lies the distinction between two possible strategies to reach ignition, which exploit two different confinement schemes, as it is described in section 1.2.4.

1.2.4 *Inertial and Magnetic confinement*

In section 1.2.3, we have said that, according to Lawson criterion, the plasma must be confined for a sufficiently long time in order to reach conditions where the ignition of the fusion reaction is possible. Two different approaches to confine a thermonuclear plasma meeting Lawson requests have been studied and are now under intense experimental investigation.

The first confinement scheme we will describe is the so-called *inertial confinement*. In *inertial confinement fusion (ICF)*, the idea is to compress a tiny target with high-power lasers to bring thermonuclear fuel to ignition conditions. If the

condition required by the Lawson criterion is met, in the compressed core, the plasma inertia confines the plasma density long enough for the thermonuclear burn to produce copious amounts of fusion reactions.
The order of magnitude for the inertial confinement time, considering a 0.1 cm diameter pellet, can be estimated to be $\tau_E \simeq \tau_{in} \sim 10^{-9}$ s, meaning that densities higher than $10^{23}\,\mathrm{cm}^{-3}$ are to be reached in order to meet Lawson criterion requirements. Efforts to study laser driven inertial confinement has been made in particular by the U.S. where the *National Ignition Facility - NIF* has been constructed at the Lawrence Livermore National Laboratory (LLNL) in California. Two main approaches have been studied [32], known as (a) *direct* and (b) *indirect drive*. In both approaches the fuel is in form of a spherical capsule, prepared with a layer of deuterium-tritium fuel on its inside surface. As the capsule surface absorbs energy and ablates, pressure accelerates the shell of remaining ablator and D−T fuel inwards, causing an implosion of the pellet. The fundamental difference between direct and indirect driven inertial fusion, is the way energy is transferred from the laser beam to the target: (a) in the former the laser is focalized directly onto the fuel pellet, trying to maintain the spherical symmetry of the shell in order to have a uniform implosion pressure all over the surface; (b) in indirect drive, instead, the symmetry problem is overcome by placing the target inside a metallic cylinder, named *hohlraum*. The laser beam is focalized onto the internal surface of the cylinder to produce X-rays, which are used to compress the target. The hohlraum material is high-Z and high density so that it has high opacity to X-ray radiation to maximize the energy coupling to the capsule. This second approach seems to be the more efficient in terms of energy coupling and the best results regarding densities and temperatures have been reached with this approach at NIF.

The second scheme is the so-called *magnetic confinement fusion (MCF)*. As it is clear by the name, externally generated magnetic fields are used in order to confine the plasma. This scheme tries to satisfy the Lawson criterion in a completely different regime of densities and confinement times with respect to ICF. Magnetic confinement, in fact, allows at least in principe to confine the plasma for much longer time, so that the possibility to have a steady state operational regime is not to be excluded for this scheme. Longer confinement times conversely mean that typical plasma densities required in magnetic confinement fusion are low, if compared with ICF densities. The maximum density is limited by pressure driven instabilities and typical values for which these are controllable are expected to be around $n \sim 10^{14}\,\mathrm{cm}^{-3}$ for a 10 keV temperature plasma. This means that to satisfy Lawson criterion confinement time around 1 s as to be reached.
Starting from chapter 2, magnetic fusion will be described in more details, according to the framework in which this thesis work has been developed.

2

EDGE PHYSICS AND MODELING IN MAGNETIC FUSION DEVICES

As we have seen in chapter 1, the basic condition to produce energy through nuclear fusion reactions is the achievement of plasma confinement so that the product $n\tau_E$ meets requirement of the Lawson criterion. Among the two confinement schemes described in section 1.2.4, in the following we will refer exclusively on the magnetic one. Specifically, in this chapter the basic ideas behind magnetic confinement are addressed, focusing on topics related to the physics and modeling of the boundary plasma region. As one will see in fact, magnetic confinement is not perfect and it needs to be supplemented by confining material walls. The study of the phenomena occurring when plasma and solid state matter enter in contact is one of the fundamental branches of research in the MCF field and it is strictly connected to the comprehension of plasma transport in the outermost region of magnetic devices.
First, in section 2.1, after a general introduction of basic physical aspects (§2.1.1), the main features of magnetic devices are addressed, distinguishing between the two main concepts of closed confinement systems: *stellarator* and *tokamak* (§2.1.2). The latter is mainly considered in the following, specifically in sections 2.2 and 2.3, where the importance of the edge plasma region in these devices is clarified. In section 2.4 the two approaches for the edge plasma modeling are presented. As one will see, edge physics description is essentially impossible without numerical codes. A brief list of many of the more used numerical codes for MCF boundary description is given in section 2.4.4.
Finally, in section 2.5, the importance of linear magnetic devices in fusion research will be addressed, with particular emphasis to their relevance in studies related to edge plasma transport and plasma-wall interaction issues. This discussion naturally leads to the motivations and the main goals of this thesis work, which are described in section 2.6.

2.1 MAGNETIC FUSION DEVICES

The aim of this section is to try to answer questions about the best magnetic field configuration able to confine the plasma and how this configuration can be obtained in a magnetic fusion device. To do that we start recalling some basic features of the dynamics of charged particles in an electromagnetic field.

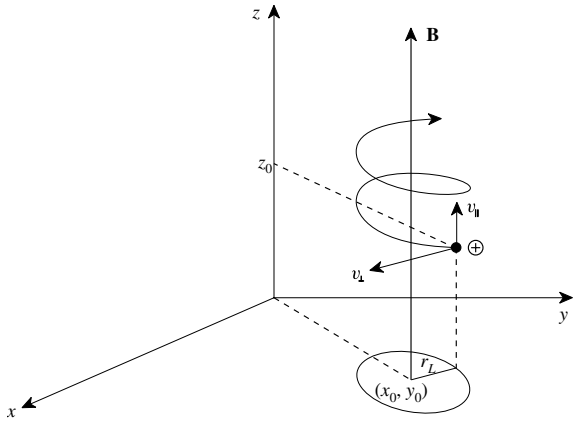

Figure 6: Motion of a positive charged particle in a uniform magnetic field from [68].

2.1.1 *Magnetic confinement physics*

It is well known from *orbit theory* [68] that a charged particle with a different from zero initial velocity and subjected to a magnetic force, executes a helical orbit around the axis parallel to the local direction of the magnetic field. It is said that the particle gyrates around the magnetic field line, while moving along it. In figure 6 the motion of a positively charged particle in a uniform magnetic field is shown. The frequency of the gyromotion and its radius are called respectively *Larmor frequency* and *Larmor radius*, or gyroradius, and are given by:

$$\nu_L = \frac{eZB}{2\pi m} \qquad\qquad r_L = \frac{v_\perp}{\nu_L} \tag{11}$$

where eZ and m are the charge and the mass of the particle and $v_\perp$ is its velocity in the direction perpendicular to the magnetic field B. Thus, increasing the strength of the magnetic field, it is possible to reduce the gyroradius to sufficiently small values and restrict the particle orbit in the close neighborhood of the magnetic field line, eventually confining the particle on the plane perpendicular to **B**. In this scheme, anyway, no confinement is addressed in the direction parallel to the magnetic field. Confinement in this direction can be obtained by two classes of device: *open confinement systems* and *closed confinement systems*. The definition refers to the topology of the externally generated field lines, which can be respectively open, usually starting from one solid surface of the vessel and ending on the other one, or closed, endlessly wrapper in toroidal confinement region. Typical devices belonging to the former category are linear plasma machines with specific magnetic field configuration called *magnetic mirror*. In a cylindrical configuration with magnetic field directed along the axis, it can be shown, using energy and magnetic moment conservation, that particles with sufficient perpendicular velocity are reflected by positive field

gradients [68]. The main employments of linear plasma devices in magnetic nuclear fusion research will be discussed in section 2.5 and, as one will see, it is not related to the exploitation of this class of devices as confining system.
Here we will focus on closed confinement systems, which are the relevant geometries nowadays studied for a fusion device. In this case, as it was mentioned, the magnetic field lines are bent, by means of appropriate coil geometries, and wrapped around so that trajectories following the magnetic field are practically endless.
Many of the basic features of the magnetic field typical of these confining systems can be understood starting from some purely topological issues, related to a theorem by Poincarè. This theorem states that *given a smooth surface S and a well behaved vector $\mathbf{C}(\mathbf{x})$, if the component of $\mathbf{C}$ tangent to S never vanishes, then S must be a torus. Moreover, from $\mathbf{C}(\mathbf{x})$ another non vanishing vector $\mathbf{D}(\mathbf{x})$, everywhere tangent to S, can be constructed* [51]. The implication to plasma confinement of this theorem is quite straightforward, in fact, if the plasma has to be everywhere magnetized, $\mathbf{B}(\mathbf{x})$ can not vanish on the outermost surface containing the plasma; furthermore, since the motion of the charged particle is unconstrained along the parallel direction, $\mathbf{B}(\mathbf{x})$ can not have components orthogonal to this surface. If these two conditions are satisfied, $\mathbf{B}(\mathbf{x})$ is said to *densely cover* the outermost plasma surface, and therefore, according to Poincarè theorem, plasma must be contained in a toroidal shell.
We define a surface densely covered by the magnetic field a *flux surface*; moreover, a function $\psi(\mathbf{x})$ that is everywhere constant on a flux surface is called *flux function*, or *flux label*. With this definition of $\psi(\mathbf{x})$, it is clear that the equation:

$$\psi(\mathbf{x}) = \psi \tag{12}$$

defines a different flux surface for each real number ψ. The relationship between the $\mathbf{B}(\mathbf{x})$ field and the flux label can be written as:

$$\mathbf{B}(\mathbf{x}) \cdot \nabla\psi = 0 \tag{13}$$

Based on these topology considerations, the shape of the magnetic field can then be inferred. Indeed, if the flux surface is a torus, the magnetic field $\mathbf{B}(\mathbf{x})$, which densely covers it, must have both toroidal ϕ and poloidal θ components, as it is shown in figure 7. Thereby, the magnetic field for a closed confinement system is written as:

$$\mathbf{B} = B_\theta \mathbf{e}_\theta + B_\phi \mathbf{e}_\phi \tag{14}$$

where $\mathbf{e}_\theta$ and $\mathbf{e}_\phi$ are the unit vector respectively in the poloidal and toroidal direction.

The simplified picture of a charged particle that gyrates around the magnetic field lines, while moving along it, can be enriched. Indeed, when a non uniform

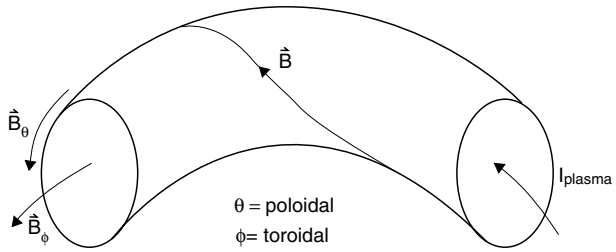

Figure 7: Poloidal and toroidal components for the magnetic field in a closed magnetic device from [74].

magnetic field and/or an electric field is present, according to the *first order guiding center approximation* [68], the particle trajectory is not simply directed along $\mathbf{B}$, but drifts arise in the $\mathbf{B} \times \nabla \mathbf{B}$ and $\mathbf{E} \times \mathbf{B}$ directions. Moreover, orbit theory is strictly valid only when we are considering single particle dynamics in a magnetic field. Things clearly become more complicate when a macroscopic system of interacting particles, like a plasma, is considered. Consider for example the fact that magnetic confinement is incompatible with the establishment of thermodynamical equilibrium. The equilibrium distribution function, in fact, depends only on the particle energy, which in turn is unaffected by the magnetic field. Therefore, a detailed characterization of magnetically confined plasmas should always consider non-equilibrium description [51].
The definition of a magnetic equilibrium configuration, however, is essential to describe not only plasma equilibrium properties but also to model plasma instabilities, transport phenomena and turbulence and plasma waves. For these reasons a simplified model is usually adopted when the magnetic equilibrium configuration has to be computed. Under the hypothesis of *ideal magnetohydrodynamics (MHD)*, plasma is represented by a single fluid with infinite electrical conductivity and zero ion gyro radius. Ideal MHD equations [28] are derived from the single-fluid approximation of the coupled system of Maxwell equations and two-fluid conservation questions (41), (42) and (43) described in section 2.4.2, assuming *quasineutral approximation* $n_e \simeq n_i \equiv n$ of the plasma and neglecting electron inertia. If then one assumes stationarity $d/dt \simeq 0$ and static condition, i. e. null plasma velocity $\mathbf{u} \simeq 0$, the ideal MHD equilibrium equations are found [28]:

$$\begin{aligned} \nabla p &= \mathbf{J} \times \mathbf{B} \\ \nabla \cdot \mathbf{B} &= 0 \\ \nabla \times \mathbf{B} &= \mu_0 \mathbf{J} \end{aligned} \tag{15}$$

where the electromagnetic variables are the electric field $\mathbf{E}$, the magnetic field $\mathbf{B}$, and the current density $\mathbf{J}$. The fluid variables are the mass density ρ, and the pressure p. These equations represents the most basic model to describe a

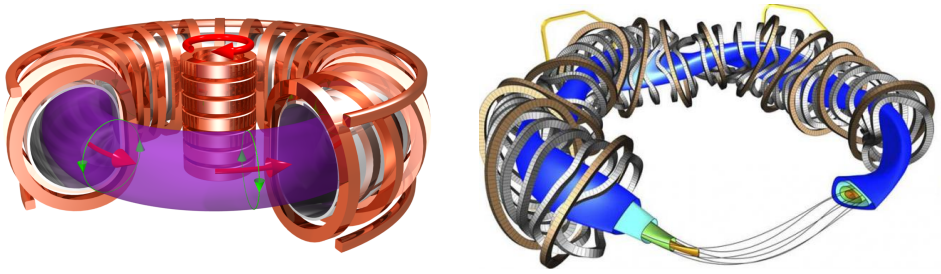

(a) *Tokamak.* (b) *Stellarator.*

Figure 8: Comparison between the tokamak and stellarator magnetic fields and coil structures. We can see that both have close nested magnetic flux surfaces, but toroidal symmetry is only achieved in tokamak geometry.

magnetized plasma and most of the time it is the starting point for any more involved description.

2.1.2 *Tokamaks and Stellarators*

Once the basic physics behind plasma confinement has been described in section 2.1.1, it is possible to present the two closed toroidal systems developed for magnetic fusion research: the tokamak and the stellarator devices.

The **tokamak** concept was first proposed by two Russian physicists, Igor Tamm and Andrei Sakharov in 1952 [33]. The name is a Russian acronym which stands for *toroidal chamber with magnetic coils*. A schematic 3D picture of a tokamak structure is represented in figure 8a.
The toroidal magnetic field B_ϕ, which in this kind of machines is the dominant component of $\mathbf{B}$, is generated by current flowing in external poloidal coils, while the poloidal component B_θ is produced by the toroidal current flowing in the plasma itself. In tokamak, this *plasma current* is induced exploiting the phenomenon of *electromagnetic induction*, generated by the current flowing in a central Ohmic transformer. Plasma current, moreover, allows the exploitation of *Ohmic heating* to increase the plasma temperature. Finally, coils in the toroidal direction are present, with the main objective of controlling the shape and the equilibrium of the plasma.
One of the characteristic features of the tokamak geometry is its symmetry in the toroidal direction, which gives remarkable advantages in the modeling of this device. On the other hand, the presence of the transformer to induce the plasma current makes this machine intrinsically a pulsed device, which is not the optimal situation in the perspective of building a reactor.
Starting from the Seventies many tokamaks have been built all over the world. From the first generation we can mention AlCaTor A (then become AlCa-

Tor C and then AlCaTor C-mod at MIT, USA - 1973), FT (now called FTU in Frascati, Italy - 1977) and TEXTOR (Julich, Germany - 1978). From the new generation of tokamak, built starting from the Eighties, we recall T-15 (Moscow, USSR), JET (now JET-ILW Culham, UK), TFTR (Princeton University, USA), JT-60 (Naka, Japan), Tore Supra (now become WEST Cadarache, France), ASDEX (now called ASDEX- Upgrade in Garching, Germany).
Of course the most important fusion research project and the most advanced tokamak design is represent by ITER (*The way*, in Latin) [58], which is now being built in Cadarache, France. The main goal of this experiment is to demonstrate the feasibility to generate net thermal energy in a magnetic fusion device: ITER is designed to produce a ten-fold return on energy $Q = 10$, or 500 MW of fusion power from 50 MW of input heating power. Other important studies that will be carried on are related to (1) study the physics of an ignite plasma, (2) testing and designing all the technologies needed for a fusion power plant such as diagnostics, control and safety systems, heating system, cryogenic plant and remote maintenance, (3) exploit the first system able to produce a self sustained D-T plasma, to investigate issues related to the tritium breeding.
Finally, a project which directly involves Italy concerns the design and construction of the DTT (Divertor Test Tokamak) facility in Frascati, Rome. This tokamak will be designed to specifically asses issues related to power exhaust in future reactors. As will be largely detailed in this thesis work, in fact, the problem of plasma-wall interaction (PWI) and power exhaust is of crucial importance in the overall feasibility of nuclear fusion exploitation.
Both ITER and DTT projects are managed by *EUROfusion (European Consortium for the Development of Fusion Energy)*, which is the main European institution aimed to coordinate the research activities on nuclear fusion.

The other magnetic confinement concept is the **stellarator** and can be considered the Western counterpart of the Soviet tokamak design. The first stellarator was design by Lyman Spitzer of Princeton University in 1951 [73] and the idea at the base of this device is to produce the twisted and closed magnetic field lines through very geometrically complex coils system, as it is shown in figure 8b. As we can see, this kind of geometry is inherently 3-dimensional contrary to the axial symmetric configuration of a tokamak. No induced Ohmic current is present and overall magnetic configuration is obtained by means of external current, allowing in principle to operate the machine in steady state. Conversely, the absence of the Ohmic current strongly reduces the plasma capability of self-heating by Joule effect.
From a historical point of view, the development of the stellarator design was abandoned after the East-West scientific thaw in the Sixties in favor of the tokamak design. Only in the Nineties, with the developments of new methods of construction which leads to an increased quality and power of the magnetic fields, improving the device performances, this kind of machines has gained new

interest. A number of new devices have been constructed since then. Major examples include Wendelstein 7-X in Greifswald at the Max Planck Institute of Plasma Physics (Germany), the Helically Symmetric Experiment (HSX) at the University of Wisconsin-Madison (USA), and the Large Helical Device (LHD) in Tokio (Japan).

2.2 DESIGN OF THE FIRST WALL

After having introduced the general concepts of magnetic confinement, we want now to move the attention to a more specific problem. From this point, we start investigating the outermost region of the toroidal vacuum chamber, which contains the so-called *boundary plasma*. In this section, it is shown that magnetic confinement of a plasma is always imperfect and the contact of the energetic plasma particles with the solid containment is unavoidable. The inner solid surface of the chamber containing the plasma in a magnetic device is called *first wall* and plays a role of paramount importance both from the physical and engineering point of view. Its three main functions are: (1) sustain the impact of energetic particles and other radiation releasing the less impurities as possible and without large degradation of its mechanical and thermodynamical properties; (2) transfer heat loads to the cooling medium, both from the steady state neutron fluxes produced by fusion and transient plasma events, like disruptions or *edge localized modes (ELMs)*; (3) minimize the tritium retention, accordingly to safety tritium inventory requirements.

To better understand the problem of *plasma-wall interaction (PWI)* and the importance of the first wall, basic features of transport phenomena in plasmas are described in section 2.2.1. This section has no claim to provide an extensive treatment of the topic, and only the elements needed to introduce the concept of *scape-off layer (SOL)* in a magnetic device (§2.2.2) will be discussed. Finally, the two configurations of limiter and divertor (§2.2.3) are then presented, trying to underline limits and advantages of the two schemes.

2.2.1 *Introduction to transport phenomena in plasmas*

In section 2.1.1, the dynamics of a charged particle in a magnetic field was introduced, underlying also that the complexity of the problem increases when instead of a single particle we try to describe a plasma. Part of this complexity is represented by the so-called *transport phenomena*. These phenomena can be ascribed to very different physical mechanisms, the most important of which are collisions between charged particles. When just binary Coulomb collisions are considered the theory to describe transport processes, starting from a condition *near local-thermodynamical equilibrium (LTE)*, is well understood and

goes under the name of *classical transport theory* [6, 60].
In a magnetized plasma, strong differences exist in the transport of charged particles along the direction of the magnetic field and in the direction perpendicular to it: we have said that, for a single particle, transport along the magnetic field lines is unconstrained, while its trajectory is bounded in the cross-field direction within a Larmor radius distance. This can also be considered true for a system of perfectly *non-interacting* particles. When interactions become important, on the contrary, the almost free transport along the field lines is clearly reduced by the collision processes, while, on the other hand, the random nature of collisions enhances a cross-field diffusion in the direction orthogonal to $\mathbf{B}$ [60].
The transport of particles, momentum and kinetic energy is related to the presence of gradients in the particle density, momentum and temperature, respectively. In this sense, transport phenomena are modeled as diffusion processes. Considering e. g. a gradient in the radial direction for the electron density n, one can write the r-component of the plasma velocity v_r as:

$$v_r \approx D_R \frac{1}{n} \frac{dn}{dr} \tag{16}$$

where D_R is the *radial diffusion*, or *transport coefficient*. In magnetized plasmas, moreover, the strong transport anisotropy in the directions along and across the magnetic field, translates into different values for the diffusion coefficient in the two directions: $D_\parallel$, $D_\perp$. Classical transport theory is able to provide quite accurate approximations of the value of the parallel diffusion coefficient $D_\parallel$, while some additional considerations on the classical value of $D_\perp$ are necessary. According to this theory, displacements orthogonal to the magnetic field are only possible due to collisions, so that cross-field diffusion coefficient $D_\perp$ is modeled as the product between the electron-ion collision frequency times the gyroradius squared, which, in the frame of *random-walk model* represents the square of the radial displacement step [54]:

$$D_\perp^{Classical} = \nu_{ei} r_L^2 = \frac{e^2\, n\, \log\Lambda\, \sqrt{m_e}}{4\pi\epsilon_0^2 B^2 \sqrt{3T_e}} \tag{17}$$

where $\log\Lambda$ is the Coulomb logarithm [6].
At the beginning of fusion research, the classical dependency of radial transport on the magnetic field strength, i. e. $D_\perp \sim 1/B^2$, gives rise to hopes that an excellent confinement of the plasma, and so a quick realization of fusion, was quite easy to be obtained just increasing the value of $\mathbf{B}$. Soon, unfortunately an anomalously large perpendicular transport coefficient was observed; furthermore only a $D_\perp \sim 1/B$ dependence was found experimentally. Despite copious efforts and progress made in this theoretical field, which goes under the name of *anomalous transport theory*, a self consistent theory on radial diffusion does not exist and no reliable predictions on $D_\perp$ can be given up to now. What it

is clear is that other physical mechanisms than Coulomb collisions affect the cross-field transport, producing diffusion up to four order of magnitude more intense than what classical theory predicts.

2.2.2 *The Scrape-Off Layer*

It is clear from the discussion in section 2.2.1 that, even if a closed magnetic field configuration, confinement in the radial direction is imperfect and *plasma-wall interaction* is unavoidable. Not only particle, but also momentum and energy fluxes are directed to the first wall and a crucial problem is to collect these fluxes without strong effects on both the solid surface and the plasma itself. To better control this interaction and to localize the impurities generated by the erosion of the first wall, usually the area where plasma and the solid interact is limited in space. To do so, the outermost field lines are opened and oriented towards a specially designed structure. In this scheme, the plasma rapidly streams along the magnetic field lines in the direction of the solid surface, while slowly diffuses in the radial direction. The cross-field diffusion in the boundary region is slow enough in comparison to the parallel transport, to give rise to a narrow plasma layer, which extends from the *last closed magnetic flux surface (LCFS)* up to few centimeters in the outgoing radial direction.This sharp plasma boundary is the so-called *scrape-off layer (SOL)*.
From the beginning of fusion research, the importance of the edge plasma[1] and the impossibility to realize magnetic confined controlled fusion without a careful understanding and controlling over the processes that interest this region were clear. Only understanding the mechanisms happening in this region, in fact, energy and particle fluxes can be estimated and methods to reduce the loads applied to the wall can be designed.
If from one side limiting the area of plasma-wall interaction allows to better control the phenomenon, on the other side a strong reduction of the *plasma-wetted area* results in an increasing of the fluxes with consequences on the *plasma facing components (PFCs)*. Beside the effects on the solid material, also the plasma is strongly affected by the consequences of PWI. Heavy impurities are indeed generated by erosion and sputtering of the wall caused by the particle fluxes and can migrate from the boundary plasma to the core region, inside the LCFS. The presence of these elements inside the ignite plasma represents a critical issue in the overall energy balance: the output thermal power, in fact, is reduced by both a fuel dilution and an increasing in the radiative losses 1.2.3).

1 Although sometimes used as synonyms of SOL, the edge plasma actually includes the scrape-off layer but also extends some distance inboard the last closed magnetic surface into the main plasma.

2.2.3 *Limiter and Divertor configurations*

From what we have seen in section 2.2.2, in principle all magnetically confined plasmas have a scrape-off layer. Anyway, in the following discussion we will refer explicitly to tokamaks. In figure 9 the two possible schemes that have been exploited to design the SOL in these machines are represented: the first type of SOL is obtained by exposing the so-called *limiter* into the plasma while the second configuration is obtained by *diverting* the edge plasma by means of special magnetic coils onto two or more target plates. In this section, we will discuss in some details these two configurations.

The limiter configuration, shown in figure 9a, was the first scheme adopted in magnetic devices in order to try to reduce the area of plasma-wall interaction. In this configuration, a dedicated and geometrically optimized structure is protruded inside the plasma so that the outermost magnetic field lines connect the two faces of the limiter and the gross of particle-surface interaction happens in this region. Usually, the geometry of this structure is such that an almost parallel incidence of the magnetic field at the top of the limiter is obtained, so that the particle fluxes on the limiter surface are reduced. Erosion of the solid material, in fact, is directly linked to the strength of the fluxes, which in turn is affected by the angle of incidence.
The main disadvantage of the limiter configuration is related to the fact that PWI area is directly facing the core plasma: impurities eroded from the limiter can cross-field diffuse rather easily to the main plasma, consequently affecting the behavior of the reactor. To try to overcome this disadvantage, another scheme was soon implemented. With additional magnetic coils, placed at the top and/or at the bottom of the tokamak chamber, the magnetic topology of the plasma is modified so that the outermost magnetic field lines are diverted and directed towards the target plates. In the poloidal plane, the magnetic field lines draw a figure-of-eight shape as shown in figure 9b and in the so-called *X-point*, the poloidal magnetic field is null. The field line passing through the X-point is called *separatrix* and is the analogous of the last closed magnetic surface in the limiter case: inside the separatrix there is the main and well confined plasma, while the region outside the separatrix is the SOL. The simplest and more common divertor geometry is shown in figure 9b. It is the so-called *lower single null (LSN) configuration*, where the targets and the X-point are located at the bottom of the vessel. In this configuration, a third plasma region, beside the core and the scrape-off layer, can be identified: it is called *private flux region (PFR)* and it is located at the bottom of the vessel between the X-point and the target plates. The plasma in this region is sustained by the transport of particles and power from the main SOL, across the private-separatrix.

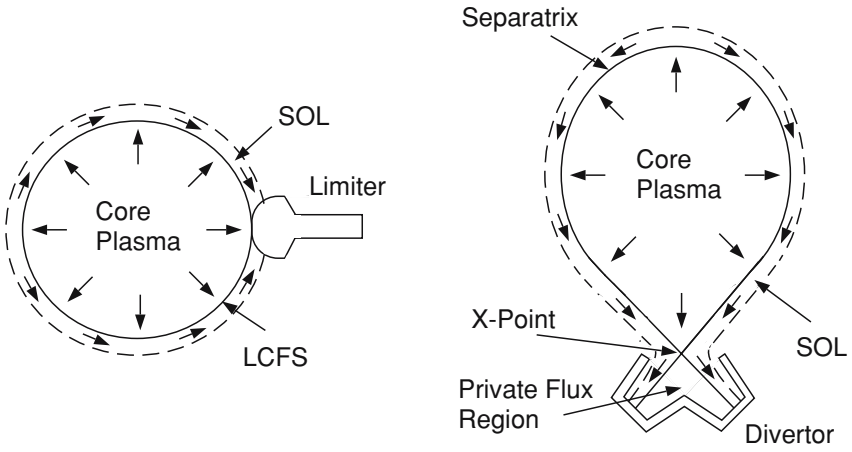

(a) *Limiter scheme.* (b) *Divertor scheme.*

Figure 9: Comparison between the two different scrape-off layer (SOL) configurations from [54].

The original motivation for introducing the divertor approach into magnetic confinement devices was, as previously stated, to reduce the impurity content in the main plasma. Indeed, the divertor configuration offers advantages with respect to both production yield and transport of impurities into the main plasma. As regard impurity migration, then, the possibility offered by a diverted geometry to locate the target plates at arbitrary distance from the core plasma allows to strongly reduce penetration in the main plasma of impurities generated at the targets. Moreover, impurity production yield is reduced in this configuration since it offers the advantage to work in a regime where large temperature gradients exist along the separatrix, the so-called *conduction limited regime*. Recalling that the sputtering yield increases with the ion temperature [7], a condition where temperature gradient exists along the SOL is compatible with the favorable situation of a maximized plasma temperature far from the targets, in the so-called *upstream region*, At the same time, sufficiently low ion temperatures at the targets to reduce the sputtering yield. Conversely, the limiter configuration usually works in the so-called *sheath limited regime*, where plasma temperature is constant along the SOL and a reduction of the ion temperature near the target plates also involves a colder core plasma. Another advantage of the divertor configuration is the increased capability to remove at high rate the helium produced by fusion. In fact, while edge impurity production can be by many means reduced, helium is unavoidably produced inside the main plasma in a D-T burning mixture and must be removed from the chamber in order to avoid unacceptable fuel dilution. Once this species has been produced inside the core, it migrates towards the SOL, recombines at the solid surface and is released as neutral atoms. One must be able to efficiently

remove the He atoms before they are re-ionized. The target leg configuration of a divertor tokamak is a favorable geometry to instal the cryo-pumps and allows to obtain a quite high neutral pressure in the pump and a consequently efficient and compact pumping system. This process is much more inefficient for a limiter configuration [74]. On the other hand, also limiters have some advantages for what concerns both the plasma wetted area and the use of the magnetic volume. An increase in the plasma wetted area is desirable since reduces the heat fluxes to the wall and in a limiter configuration can be increased more easily that in a divertor, by adding more limiter structures or directly shaping the first wall so that is has almost the same curvature of the magnetic field lines. As for the use of magnetic volume, in the optic to build an economically competitive reactor and considering that a consistent part of the capital cost is related to the dimension of the poloidal magnets and so of the primary chamber, one should try to maximize the volume occupied by the D-T burning plasma inside the primary vessel. Certainly, a divertor with very long legs is not very effective from this point of view.

In conclusion the choice between limiter or divertor configuration is not straightforward: many factors are involved and, with regard to most of the issues understanding continues to evolve. Presently the balance of consideration favors divertor, and so tokamaks that are under construction now, like ITER, are being build following this approach. Moreover, to carry out more dedicated studies about divertor developments for future nuclear fusion reactors, facilities like DTT are currently under design.

2.3 PHYSICAL PHENOMENA IN THE SCRAPE-OFF LAYER

In section 2.2.2, the concept of the scrape-off layer in a magnetic plasma device has been introduced. In this section we want to better understand the physical mechanisms which determine the plasma behaviour in this peculiar region. In section 2.3.1, we start with the description of one of the first phenomena studied in the context of plasma-material interaction, i. e. the formation of an electrostatic sheath on the top of the solid surface facing the plasma. Then, in section 2.3.2, the effects related to the interaction of the plasma with the neutral species present in the chamber will be addressed.

2.3.1 *Formation of the Electrostatic Sheath*

Solid walls are often said to be sinks for plasmas since, when the magnetic field lines are opened and directed towards a solid surface, the plasma freely moves towards the wall slowly diffusing in the orthogonal direction, as discussed in section 2.2.2. But how does the plasma know, at each point along the SOL,

which is the direction towards the surface? In other words, what is the local force that causes the acceleration of the plasma in the direction of the wall? To answer this question the concept of *electrostatic sheath* must be introduced.

Suppose that the unperturbed plasma is equipotential at the so-called *plasma potential* ϕ_P. Whenever a solid object, kept at a potential lower than ϕ_P, is put in contact with the plasma, a voltage difference spontaneously develops between the hosting medium and the object. This voltage difference is called the *floating potential* ϕ_F. The cause behind this phenomenon is to be recognized in the much smaller inertia of electrons with respect to ions: their larger mobility produces, in the first instants ($\sim$ µs) after the object and the plasma are made in contact, an intense negative random flux to strike the solid surface charging it negatively. An electron repelling potential is then generated on the top of the surface facing the plasma, producing a region of net positive charge density, called *electrostatic sheath*. The negative charge on this surface approximately equals the positive charge density in the sheath so that the sheath acts to shield the plasma from the potential on the solid surface. This phenomenon is called *Debye shielding*. The spatial extension of the electrostatic sheath is of the order of the *Debye length* [69]

$$\lambda_D = \sqrt{\frac{\epsilon_0 T_e}{n_e e^2}} \tag{18}$$

Furthermore, the shielding effect of the sheath is imperfect and a small residual field penetrates deep into the plasma, generating a quasi-neutral plasma region, called the *pre-sheath*. Although the potential drop in the pre-sheath is just a small fraction of the total floating potential, it is sufficient to draw ions from the upstream plasma into the sheath. It can be shown that this accelerating field is such that the ion drift velocity, at the sheath/plasma interface, should bee equal or higher than the *ion acoustic speed*

$$c_s \geq \sqrt{\frac{(T_e + T_i)}{m_i}} \tag{19}$$

This is the so-called *Bohm criterion* [61, 74]. The remaining part of the potential drop accelerates the ions through the sheath, thus making them impact the solid surface with an energy which is greater than that associated with their temperature, T_i.
Plasma pressure and potential, ion drift speed and electron and ion densities variations along the SOL are shown in figure 10. From this figure, one can see that the sink action of the solid surface generates a depression in the local plasma density and an associated pressure gradient. The wall sink action can

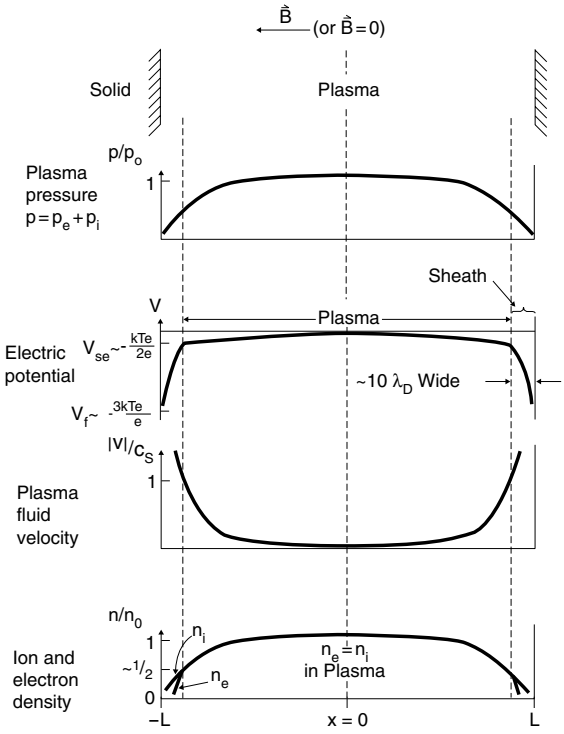

Figure 10: Variation for the plasma profiles along the SOL. Plasma pressure, potential, ion drift speed and electron and ion densities are shown in the sheath and pre-sheath regions [74].

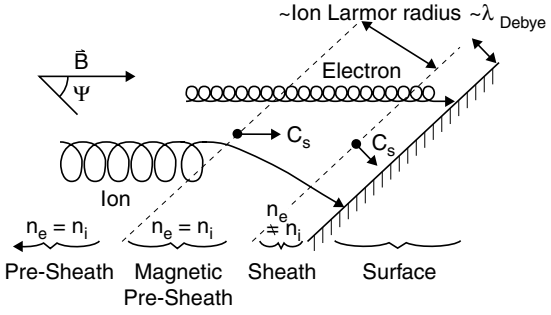

Figure 11: Plasma-wall interaction when **B** is oblique to the surface. The analysis was first made by Chodura [14].

be estimated by expressing the particle flux at the *sheath entrance* in terms of plasma upstream temperature $T_{e,i}$ and density n [74]

$$\Gamma_{se} \simeq \frac{1}{2} n \sqrt{\frac{(T_e + T_i)}{m_i}} \tag{20}$$

Moreover the sheath controls the rates at which energy is removed from the plasma by the solid surface. *Sheath transmission coefficients* for both electrons and ions are given in [74].
All the results just presented do not explicitly include the presence of a magnetic field. They are therefore suitable for describing the flow of plasma along magnetic field lines towards a surface with normal along **B**, since such flow is not impeded by the magnetic field. In real magnetic devices, however, the angle between the surface normal and **B** is usually quite large, in particular when a divertor configuration is used. Moreover referring to figure 11, a glancing angle Ψ between the magnetic field and the surface is desirable, in order to make the deposited heat flux only a small fraction of the total parallel heat flux:

$$q_{dep} = q_{\parallel} \cos \Psi \tag{21}$$

where $q_{\parallel}$ is the modulus of the heat flux in the direction parallel to **B** [61].
A simplified picture of the situation in presence of an oblique magnetic field is given in figure 11. In addition to the already introduced electrostatic sheath and pre-sheath, a third region exists in this case, known as *magnetic pre-sheath*, or *Chodura sheath* [14]. This region, located between the sheath and the pre-sheath, is quasi-neutral and its width is about few *ion Larmor radii*

$$r_{L,i} \simeq \frac{m_i c_s}{eB} \tag{22}$$

In the pre-sheath, far from the surface, electric forces are small due to the shielding effect of the sheath: when an intense magnetic field is present, magnetic forces dominate and the plasma flows nearly parallel to **B** even if the field is oblique with respect to the surface. Approaching the wall, however, electric forces start to become important and the plasma flow is bent from magnetic field direction to the direction of the wall normal. Nevertheless electron and ion flow paths in the magnetic pre-sheath/sheath region are different. Ion flow path starts to be deviated when the distance from the wall is of the order of their gyroradius, while electrons, due to their small mass, are more strongly coupled to magnetic field lines and at first continue to flow along **B** until they deviate when the sheath entrance is reached. Chodura was able to show [14] that Bohm criterion, expressed by equation (19), is still valid at the entrance of the magnetic pre-sheath demonstrating that the plasma upstream has no 'knowledge' of whether the plasma flow tube is terminated by a normal sheath or an oblique sheath. It is clear, therefore, that the choice of the angle Ψ,

although it has strong relevance on the heat dissipation, according to equation (21), has very little effect on any aspect of the plasma properties.

The extension of the theory described so far to the case in which the solid object inserted into the plasma is biased to a certain potential is the base of *Langmuir probes (LPs)* [53]. LPs have been one of the most widely used diagnostic techniques for low temperature plasmas, $T_e \lesssim 100\,\mathrm{eV}$, and have also come to be widely used over recent years for SOL measurements. A brief introduction to the theory and the working principles of Langmuir probes is given in Appendix B.

2.3.2 *The role of atomic species in edge physics*

The formation of the electrostatic sheath, described in section 2.3.1, is a mechanism which involves only electrons and ions, when in contact with a solid material. Besides charged particles, however, also atomic and molecular species present in the plasma play an important role in determining the behaviour of plasma properties inside the scrape-off layer. This will be extensively discussed in this thesis work and so in this section some of the phenomena involving neutral particles in the boundary plasma are introduced.

The existence of neutral gas in the SOL region of a tokamak plasma is due to external gas puffing, which is used to refuel the plasma, or more importantly, to the *recycling process* happening at the solid surface. Ions impinging on the surface of the solid wall, as described in section 2.3.1, can either be backscattered or remain attached to the wall, recombining with electrons from the solid and thermalizing in the near surface. Once neutralization and thermalization have occurred, they are released as neutral particles and successively re-ionized by the plasma: this is the so-called recycling process. After an initial phase in which the absorption of charged particle prevails and the wall acts as an effective sink for the plasma, the retention of the recombined neutral particles in the near solid surface saturates. From this moment on, a steady-state situation results, where the charged particles retained by the surface and the ionization of the desorbed particles are balanced and the plasma is said to *refuel itself*. If no active pumping system is present in the chamber, in fact, the plasma density, once the stationary recycling regime is reached, remains constant without the need for an external fueling system[2].

The presence of neutral atoms and molecules in the plasma generates a wide range of possible interaction processes through which charged and neutral par-

2 As we have already said (§2.2.3), active pumping system are necessary in real fusion devices to remove the helium ash, and so pumping and puffing are always present in a real machine.

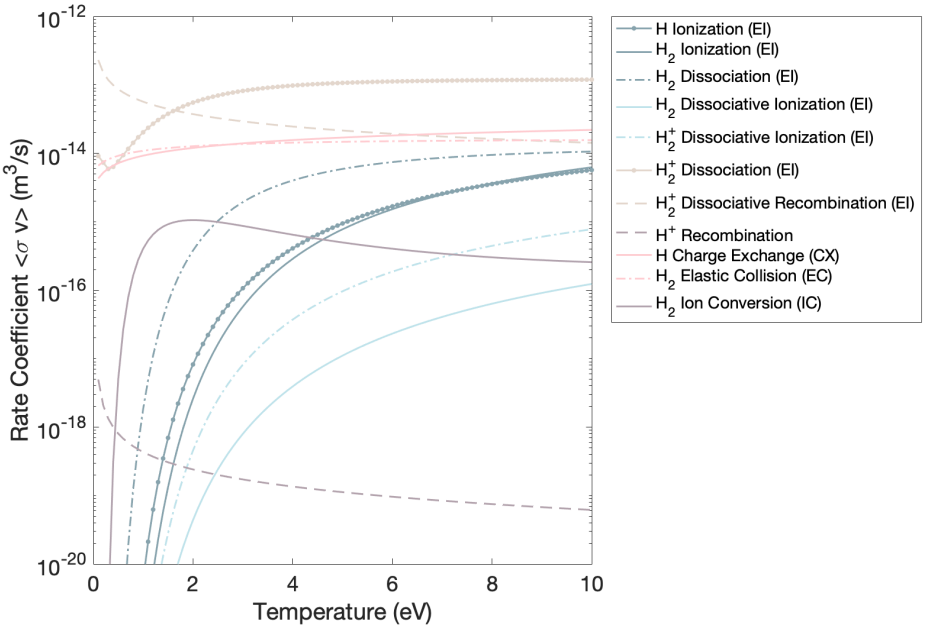

Figure 12: Rate coefficients $\langle \sigma v \rangle$ for the most relevant reactions in a hydrogen plasma. The explicit form of the reactions is shown in table 1. We can see that the only reaction involving just charged particles is the $H_2{}^+$ *dissociative ionization*, all the others involve as products or reactants both charged and neutral species. The value for the electron density n_e is supposed to be $n_e = 1 \times 10^{16}\,\mathrm{m}^{-3}$.

Reaction	**Name of the reaction**
$e + \mathrm{H} \rightarrow 2e + \mathrm{H}^+$	H Ionization
$e + \mathrm{H_2} \rightarrow 2e + {\mathrm{H_2}}^+$	$\mathrm{H_2}$ Ionization
$e + \mathrm{H_2} \rightarrow e + 2\,\mathrm{H}$	$\mathrm{H_2}$ Dissociation
$e + \mathrm{H_2} \rightarrow 2e + \mathrm{H} + \mathrm{H}^+$	$\mathrm{H_2}$ Dissociative ionization
$e + {\mathrm{H_2}}^+ \rightarrow e + \mathrm{H}^+ + \mathrm{H}^+$	${\mathrm{H_2}}^+$ Dissociative ionization
$e + {\mathrm{H_2}}^+ \rightarrow 2e + \mathrm{H} + \mathrm{H}^+$	${\mathrm{H_2}}^+$ Dissociation
$e + {\mathrm{H_2}}^+ \rightarrow 2\,\mathrm{H}$	${\mathrm{H_2}}^+$ Dissociative recombination
$e + \mathrm{H}^+ \rightarrow \mathrm{H}$	H^+ Recombination
$\mathrm{H}^+ + \mathrm{H} \rightarrow \mathrm{H} + \mathrm{H}^+$	H Charge exchange
$\mathrm{H_2} + \mathrm{H}^+ \rightarrow \mathrm{H_2} + \mathrm{H}^+$	$\mathrm{H_2}$ Elastic collision
$\mathrm{H_2} + \mathrm{H}^+ \rightarrow {\mathrm{H_2}}^+ + \mathrm{H}$	$\mathrm{H_2}$ Ion conversion

Table 1: Description of the most relevant reactions in a hydrogen plasma according to [39].

ticles can interact. The most important of them for a hydrogen plasma are reported in table 1 and the corresponding rate coefficients $\langle \sigma v \rangle$ are shown in figure 12. A large part of these reactions belongs to the class of *electron impact ionization (EI)*. According to the discussion presented in section 1.2.1, the *probe particle*, that can be both charged or neutral, collides with an *electronic background*, assumed to be in thermodynamical equilibrium. This type of reaction processes is supposed to be important since electron-ion collision frequency is much higher than ion-ion collision frequency, due to the small inertia of electrons. As an order of magnitude, in fact, the ratio of these two frequences is inversely proportional to the square root of the mass ratio, i. e. $\nu_{ei}/\nu_{ii} \sim \sqrt{m_i/m_e}$. Collisions between heavier particles, then, have much lower collision frequency and only few reactions of this type have to be considered. Among these, we consider *H_2 ion conversion (IC)*, which together with $\mathrm{H_2}$ ionization is responsible for the production of H_2^+ charged molecules, and the two reactions of *elastic scattering (EC)* and *charge exchange (CX)*. Many databases exist containing numerical fits for both the cross-section and the rate coefficient of the most frequent reactions happening in fusion plasmas [19, 20, 23, 35].
The rate coefficients reported in figure 12 are obtained using numerical fits from the AMJUEL [19] database. The fits for electron impact ionization (EI) rate coefficients are given as a function of electron density and temperature

$$\log \langle \sigma v \rangle = \sum_{n=0}^{N} \sum_{m=0}^{M} \alpha_{n,m} (\log \tilde{n})^m (\log T)^n \tag{23}$$

where $\langle \sigma v \rangle$ is in $\mathrm{cm}^3\,\mathrm{s}^{-1}$, T is in eV and $\tilde{n}$ is in $\mathrm{cm}^3/10^8$. To plot rate coefficients reported in figure 12, the electron density was supposed to be $n_e = 1 \times 10^{16}\,\mathrm{m}^{-3}$. Fits for charge exchange (CX), elastic collision (EC) and ion conversion (IC) rates coefficient are given as a function of temperature alone

$$\log \langle \sigma v \rangle = \sum_{n=0}^{N} b_n (\log T)^n \tag{24}$$

The effect of plasma-neutral interaction is a fundamental aspect in SOL modeling and, as we will see also in this thesis work, modification of the neutrals content in the plasma, e. g. obtained modifying the puffing or pumping rate, strongly affects the plasma properties.
Moreover, neutral injection in the divertor region in tokamaks has been intensively studied since the achievement of the so-called *divertor detachment* has beneficial effects on the power exhausting [45]. Plasma detachment from a divertor target is defined as the state in which large gradients in total plasma pressure are observed parallel to the magnetic field with consequent reductions in the plasma power and ion fluxes to the limiting surfaces [50]. A detached regime is then desirable since it reduces the power loading on the *plasma facing components* and ion fluxes and temperature near the target, consequently reducing the erosion of the material. Presently, operation with the detached divertor is the key element of the ITER baseline design [42, 58].

Having discussed the fundamental aspects related to the scrape-off layer, suitable mathematical models to describe and better understand the plasma dynamical evolution in the SOL has to be introduced. This will be the aim of section 2.4, where kinetic and fluid models are presented.

2.4 PLASMA EDGE MODELING

Mathematical models are fundamental in order to better understand the complex behaviour of plasma in the SOL. In this section, we will describe the kinetic and fluid models widely used to describe the plasma in magnetic fusion research. We will start from the more general kinetic model (§2.4.1) and then derive from it the fluid approximation (§2.4.2). Finally the limits of the present models will be outlined (§2.4.3). Although simple analytical models to describe the plasma in the edge region of a fusion device have been formulated [74], they usually give too partial results to fully understand edge physical phenomena. To have a better insight on boundary plasma physics, elaborated computational code has been developed and the most used in the field of magnetic fusion research are presented in section 2.4.4.

2.4.1 *Kinetic models*

The most accurate description we are able to give of the plasma dynamics is by means of the so-called *kinetic theory*. The aim of this theory is to determine the distribution function $f_a(\mathbf{x}, \mathbf{v}, t)$ for each plasma species, taking into account the motions of *ensemble of particles* contained in the plasma. The equation describing the evolution of the distribution function is the well-known *Boltzmann equation* [8] and for the a-th species in the plasma it is written as

$$\frac{\partial f_a(\mathbf{x}, \mathbf{v}, t)}{\partial t} + \mathbf{v} \cdot \nabla_{\mathbf{x}} f_a + \frac{q_a}{m_a} (\mathbf{E} + \mathbf{v} \times \mathbf{B}) \cdot \nabla_{\mathbf{v}} f_a = C(f_a) \tag{25}$$

If the $a - th$ species considered is neutral, then the electromagnetic term in equation (25) is clearly null. To understand the various terms which appear in this equation, and in particular the so-called *collision term* $C(f_a)$, a brief description of its derivation is given. The starting point of the derivation is the equation for the evolution of the *one-particle density functional* $N_a(\mathbf{x}, \mathbf{v}, t)$

$$N_a(\mathbf{x}, \mathbf{v}, t) = \delta(\mathbf{x} - \mathbf{X}(t))\delta(\mathbf{v} - \mathbf{V}(t)) \tag{26}$$

describing the position and velocity for each plasma particle of species a at each time. The so-called *Klimontovich equation* states that the convective derivative in phase space of the one-particle density functional is equal to zero [55]

$$\frac{DN_a(\mathbf{x}, \mathbf{v}, t)}{Dt} \equiv \frac{\partial N_a(\mathbf{x}, \mathbf{v}, t)}{\partial t} + \mathbf{v} \cdot \nabla_{\mathbf{x}} N_a + \frac{\mathbf{F}}{m_a} \cdot \nabla_{\mathbf{v}} N_a = 0 \tag{27}$$

and provides an exact description of the plasma, computing the true trajectory for each particle. However, it is clear that the equation is far from being solvable for practical purposes due to the huge number of particles we are interested in. Then, the distribution function $f_a(\mathbf{x}, \mathbf{v}, t)$ is introduced. This function is the *ensemble average* of the density functional and represents the number of particles of species a per unit volume $d\mathbf{x}d\mathbf{v}$ in *phase space*

$$f_a(\mathbf{x}, \mathbf{v}, t) = \langle N_a(\mathbf{x}, \mathbf{v}, t) \rangle \tag{28}$$

The Boltzmann equation for the time evolution of $f_a(\mathbf{x}, \mathbf{v}, t)$ can be obtained from the Klimontovich equation (27), writing the quantities $N_a(\mathbf{x}, \mathbf{v}, t)$, $\mathbf{E}_t(\mathbf{x}, \mathbf{v}, t)$ and $\mathbf{B}_t(\mathbf{x}, \mathbf{v}, t)$ as the sum of an average part plus the fluctuations

$$\begin{aligned} N_a(\mathbf{x}, \mathbf{v}, t) &= f_a(\mathbf{x}, \mathbf{v}, t) + \delta N_a(\mathbf{x}, \mathbf{v}, t) \\ \mathbf{E}_t(\mathbf{x}, \mathbf{v}, t) &= \mathbf{E}(\mathbf{x}, \mathbf{v}, t) + \delta \mathbf{E}(\mathbf{x}, \mathbf{v}, t) \\ \mathbf{B}_t(\mathbf{x}, \mathbf{v}, t) &= \mathbf{B}(\mathbf{x}, \mathbf{v}, t) + \delta \mathbf{B}(\mathbf{x}, \mathbf{v}, t) \end{aligned} \tag{29}$$

A self consistent description of the plasma is then given by the solution of the Boltzmann equation (25) coupled to the *Maxwell equations* [34].

Substituting equations (29) into equation (25) and taking its ensemble average, it is easy to show that the collision term $C(f_a)$ in the Boltzmann equation essentially represents the effect of the fluctuations δN_a, $\delta\mathbf{E}$ and $\delta\mathbf{B}$ on the evolution of the distribution function:

$$C(f_a) = -\frac{q_a}{m_a}\left\langle\left(\delta\mathbf{E} + \frac{\mathbf{v}}{c}\times\delta\mathbf{B}\right)\cdot\nabla_{\mathbf{v}}\delta f_a\right\rangle \tag{30}$$

More generally, the $C(f_a)$ term is defined as the effect of the interaction between plasma particles. There are situations in which a plasma can be considered *collisionless* and so $C(f_a)$ is just set equal to zero, reducing equation (25) to the *collisionless plasma kinetic equation*, also known as *Vlasov equation*. Anyway, this is not usually the case when considering SOL plasmas, where the collision term must be suitably modeled. This is often done in the so-called *diffusion approximation* and the collision term is in the form of a *Fokker-Planck collision operator* [31, 46]. When considering binary Coulomb collisions between two charged particles of species a and b, the collision operator reduces to

$$C(f_a, f_b) = -\frac{q_a^2 q_b^2 \log\Lambda}{8\pi\epsilon_0^2 m_a}\frac{\partial}{\partial\mathbf{v}}\int \underline{\underline{\mathbf{U}}}\cdot\left(\frac{f_b}{m_a}\frac{\partial f_a}{\partial\mathbf{v}} - \frac{f_a}{m_b}\frac{\partial f_b}{\partial\mathbf{v}}\right) \tag{31}$$

where the subscripts a and b refer to the two species, $\log\Lambda$ is the Coulomb logarithm [6, 46] and $\underline{\underline{\mathbf{U}}}$ is the *scattering tensor*

$$\underline{\underline{\mathbf{U}}} = \frac{v^2\underline{\underline{\mathbf{I}}} - \mathbf{vv}}{v^3} \tag{32}$$

Equation (31) is the expression obtained by Landau and it is called *Landau collision integral*. Conversely, when binary interactions between neutrals or neutrals and charged particles are considered, the *Lorentz force* in equation (25) is not present and the collision integral is modeled according to *Boltzmann collision integral*

$$C(f_a, f_b) = \int \sigma(\mathbf{v}_a, \mathbf{v}_b)|\mathbf{v}_a - \mathbf{v}_b|\left[f_a(\mathbf{v}_a')f_b\mathbf{v}_b' - \mathbf{v}_a)f_b\mathbf{v}_b\right]d\mathbf{V}'d\Omega \tag{33}$$

where $\mathbf{v}_a'$, $\mathbf{v}_b'$ are the pre-collision velocities, $\mathbf{v}_a$, $\mathbf{v}_b$ are the post-collision velocities, and $d\Omega = \sin\chi d\chi d\epsilon$, χ being the deflection angle and ϵ the scattering angle.

Although, in principle this kinetic description gives the most detailed representation of edge plasma dynamics, the solution of the non linear system of coupled equations (25), for every charged and neutral particle species present in a magnetic device, is very expensive from the computational point of view even for a simple pure hydrogen plasma. In section 2.4.2, we will see that the *fluid approximation* can be conveniently adopted to model the plasma transport, when describing typical boundary plasmas. The validity of the fluid approximation and the limitations concerning its application to the electron, ion and neutral species composing the boundary plasma is of crucial importance in edge modeling and will be emphasized in this thesis work.

2.4.2 *Fluid models*

In this section we will show that a simpler model compared with the one described in 2.4.1, still usually suitable to capture many aspects of the edge plasma dynamics, can be provided starting from Boltzmann equation. This model is the so-called *multi-fluid plasma model* and it is obtained from equation (25) by taking *moments over the velocity space of the distribution function* $f_a(\mathbf{x}, \mathbf{v}, t)$ for each plasma species. With this procedure, the identity of the individual particle is neglected by integrating over the velocity distribution and only the motion of the so-called *fluid elements* is taken into account. In general, a moment over the velocity space is a smooth function defined as

$$\langle \psi(\mathbf{v}) \rangle_a \equiv \frac{1}{n_a} \int f_a(\mathbf{x}, \mathbf{v}, t) \psi(\mathbf{v}) d\mathbf{v} \tag{34}$$

where ψ has a power dependence on $\mathbf{v}$, $\psi \sim v_x^l v_y^m v_z^n$ and the *order of the moment* is given by $l + m + n$. Multiplying the Boltzmann equation (25) by $\psi(\mathbf{v})$ and integrating over the velocity space, the general evolution equation for the moment ψ is obtained

$$\frac{\partial}{\partial t} \left(n_a \langle \psi \rangle_a \right) + \nabla_{\mathbf{x}} \cdot \left(n_a \langle \mathbf{v} \psi \rangle_a \right) - \frac{q_a}{m_a} \left\langle \left(\mathbf{E} + \frac{\mathbf{v}}{c} \times \mathbf{B} \right) \cdot \nabla_{\mathbf{v}} \psi \right\rangle_a = \langle C \psi \rangle_a \tag{35}$$

Starting from definition (34), many important *macroscopic* plasma quantities can be defined [6]. The *local plasma particle density* for the species a is

$$n_a(\mathbf{x}, t) = \int f_a(\mathbf{x}, \mathbf{v}, t) d\mathbf{v} \tag{36}$$

The *local fluid velocity* for the species a $\mathbf{u}_a$ is defined via the *flux of particles* of species a

$$\Gamma_a(\mathbf{x}, t) = n_a(\mathbf{x}, t) \mathbf{u}_a(\mathbf{x}, t) = \int \mathbf{v} f_a(\mathbf{x}, \mathbf{v}, t) d\mathbf{v} \tag{37}$$

The third fundamental macroscopic quantity of interest is the *total kinetic energy density* E_a, defined as

$$n_a(\mathbf{x}, t) E_a(\mathbf{x}, t) = \frac{1}{2} m_a \int v^2 f_a(\mathbf{x}, \mathbf{v}, t) d\mathbf{v} \tag{38}$$

This quantity is usually split into two terms with different physical meaning: we distinguish between the *macroscopic kinetic fluid energy density* and the *thermal energy density*

$$n_a(\mathbf{x}, t) E_a(\mathbf{x}, t) = \frac{1}{2} m_a n_a(\mathbf{x}, t) |\mathbf{u}_a(\mathbf{x}, t)|^2 + n_a(\mathbf{x}, t) \epsilon_a(\mathbf{x}, t) \tag{39}$$

where the *thermal energy density* ϵ_a is related to the *plasma temperature* T_a and *plasma pressure* $p_a = n_a T_a$ by

$$\begin{aligned} n_a(\mathbf{x},t)\epsilon_a(\mathbf{x},t) &= \frac{1}{2}m_a \int |\mathbf{v}-\mathbf{u}_a(\mathbf{x},\mathbf{v},t)|^2 f_a(\mathbf{x},\mathbf{v},t)d\mathbf{v} = \\ &\equiv \frac{3}{2}n_a(\mathbf{x},t)T_a(\mathbf{x},t) = \frac{3}{2}p_a(\mathbf{x},t) \end{aligned} \tag{40}$$

When one is interested in a fluid description of plasmas, the main intent is to estimate the particle density $n_a(\mathbf{x},t)$, temperature $T_a(\mathbf{x},t)$ and the fluid velocity $\mathbf{u}_a(\mathbf{x},t)$ for each species in the plasma. Substituting into equation (35) respectively $\psi = 1$, $\psi = m_a\mathbf{v}$ and $\psi = 1/2 m_a v^2$, the corresponding *equations for the conservation of plasma density, momentum and energy* are found:

$$\frac{\partial n_a}{\partial t} + \nabla\cdot(n_a\mathbf{u}_a) = \sum_{n,i} S_{n,i}(f) \tag{41}$$

$$\begin{aligned} \frac{\partial}{\partial t}(m_a n_a \mathbf{u}_a) + \nabla\cdot(m_a n_a \mathbf{u}_a\mathbf{u}_a) = \\ -\nabla p_a - \nabla\cdot\underline{\underline{\mathbf{\Pi}_a}} + q_a n_a(\mathbf{E}+\frac{\mathbf{v}}{c}\times\mathbf{B}) + \sum_{n,i} S_{n,i}(m_a\mathbf{v}f) \end{aligned} \tag{42}$$

$$\begin{aligned} \frac{\partial}{\partial t}\left(\frac{3}{2}n_a T_a\right) + \nabla\cdot\left(\frac{5}{2}n_a\mathbf{u}_a T_a\right) = \\ \mathbf{u}_a\cdot\nabla p_a - \underline{\underline{\mathbf{\Pi}_a}} : \nabla\mathbf{u}_a - \nabla\cdot\mathbf{q}_a + \sum_{n,i} S_{n,i}(\frac{m_a}{2}v^2 f) \end{aligned} \tag{43}$$

where the source terms $\sum_{n,i} S_{n,i}$ represent the effect of collisions among the different plasma species, and can be divided into terms due to collisions with neutrals S_n or with other charged particles S_i. Nevertheless, the three equations (41), (42) and (43) do not form a closed system: the *viscous stress tensors* $\underline{\underline{\mathbf{\Pi}_{e,i}}}$, the *conductive heat fluxes* $\mathbf{q}_{e,i}$ and the collisions contributions, or *friction forces* $\mathbf{R}_{e,i}$ and $Q_{e,i}$ are in fact additional unknowns and their expressions in terms of the n_{ei}, $\mathbf{u}_{e,i}$ and $T_{e,i}$ must be provided in order to close the problem. The so-called *closure problem* is actually the crucial points of the fluid approximation. As we can see from equation (35), each moment of the Boltzmann equation describes the evolution of the variable $\langle\psi\rangle_a$ but also introduces the next higher moment variable $\langle\mathbf{v}\psi\rangle_a$ in the *divergence term*. A description of the plasma dynamics equivalent to the solution of Boltzmann equation is obtained only if an infinite series of moments is taken. On the contrary, the fluid approximation relies on the truncation at some finite order of the moment development. Thus, suitable relations between higher order moments and the macroscopic plasma quantities must be found.

The first self-consistent work about closure of the system of equations (41), (42)

and (43) is the one of Braginskii [11], who was able to deduce expressions for $\underline{\underline{\mathbf{\Pi}}}_{e,i}$, $\mathbf{q}_{e,i}$, $\mathbf{R}_{e,i}$ and $Q_{e,i}$ considering and electron-ion fully ionized plasma in the presence of a magnetic field. His work is essentially based on the observation that all the above mentioned coefficients are null if the system is in thermodynamical equilibrium, i. e. electrons and ions are described by Maxwellian distribution functions. The idea was then to provide a correction for *near LTE* conditions by expanding the electron and ion distribution functions around thermodynamic equilibrium. Here we summarize the main results of Braginskii transport theory [6, 11].

First, elastic collisions give no contribution to the particle density; then, defining $\mathbf{R}_{ei}$ to be the change in the electron momentum due to collisions with ions, and Q_{ei} the heat generated in the same events, the following relations hold [6, 11]

$$\mathbf{R}_{ei} = -\mathbf{R}_{ie} \tag{44}$$

$$Q_{ei} + Q_{ie} = -\mathbf{R}_{ei}\left(\mathbf{u}_e - \mathbf{u}_i\right) \tag{45}$$

The transfer of momentum from the ions to the electrons $\mathbf{R}_{ei} = \mathbf{R}_u + \mathbf{R}_T$ is given by two contributions: the first $\mathbf{R}_u$ is due to the existence of a relative velocity between electrons and ions $\mathbf{u} = \mathbf{u}_e - \mathbf{u}_i$ and the second $\mathbf{R}_T$ is the thermal force due to the gradient of the electron temperature T_e.

$$\mathbf{R}_u = -\frac{m_e n_e}{\tau_e}\left(0.51\mathbf{u}_{\parallel} + \mathbf{u}_{\perp}\right) = e n_e \left(\frac{\mathbf{j}_{\parallel}}{\sigma_{\parallel}} + \frac{\mathbf{j}_{\perp}}{\sigma_{\perp}}\right) \tag{46}$$

$$\mathbf{R}_T = -0.71 n_e \nabla_{\parallel} T_e - \frac{3}{2}\frac{n_e}{\omega_e \tau_e}\left(\mathbf{b} \times \nabla T_e\right) \tag{47}$$

where $\mathbf{b} = \mathbf{B}/B$, the *current density* is defined as $\mathbf{j} \equiv -e n_e \mathbf{u}$, $\omega_e = eB/m_e$ is the electron Larmor frequency and τ_e is the electron-electron collision time. The general dependency for the collision time of a species a with a species b is given by the following expression [6, 11]

$$\tau_{ab} \sim \frac{(4\pi\epsilon_0)^2 m_a^{1/2} T_a^{3/2}}{q_a^2 q_b^2 n_b \log \Lambda_{ab}} \tag{48}$$

where the numerical coefficient in front of this expression is slightly different if we consider electron-electron τ_e, electron-ion τ_{ei} or ion-ion τ_i collisions.
The Braginskii expression for heat transferred from electrons to ions is

$$Q_{ie} = \frac{3 m_e}{m_i}\frac{n_e}{\tau_{ei}}(T_e - T_i) \tag{49}$$

Analogously to the friction force, also the electron heat flux is given by two contributions, one originated from the relative velocity $\mathbf{u}$ and one from the electron thermal gradient:

$$\mathbf{q}_u^e = 0.71 n_e T_e \mathbf{u}_\parallel + \frac{3}{2}\frac{n_e T_e}{\omega_e \tau_e}(\mathbf{b}\times\mathbf{u}) \tag{50}$$

$$\mathbf{q}_T^e = -\kappa_\parallel^e \nabla_\parallel T_e - \kappa_\perp^e \nabla_\perp T_e - \frac{5}{2}\frac{n_e T_e}{m_e \omega_e}(\mathbf{b}\times\nabla T_e) \tag{51}$$

where the *thermal conductivities* $\kappa_\parallel^e$ and $\kappa_\perp^e$ are given by

$$\kappa_\parallel^e = \frac{3.16 n_e T_e \tau_e}{m_e} \qquad \kappa_\perp^e = \frac{4.66 n_e T_e}{m_e \omega_e^2 \tau_e} \tag{52}$$

The electron viscosity $\underline{\underline{\mathbf{\Pi}_e}}$ is negligible when the magnetic field is sufficiently intense, $\omega_e \tau_e \gg 1$.
Concerning the ions, the heat flux is

$$\mathbf{q}_i = -\kappa_\parallel^i \nabla_\parallel T_i - \kappa_\perp^i \nabla_\perp T_i + \frac{5}{2}\frac{n_i T_i}{m_i \omega_i}(\mathbf{b}\times\nabla T_i) \tag{53}$$

where the thermal conductivities are

$$\kappa_\parallel^i = \frac{3.9 n_i T_i \tau_i}{m_i} \qquad \kappa_\perp^i = \frac{2 n_i T_i}{m_i \omega_i^2 \tau_i} \tag{54}$$

Finally the components of the *ion viscous stress tensor* $\underline{\underline{\mathbf{\Pi}_i}}$, in a reference frame with z parallel to the magnetic field $\mathbf{B}$, are

$$\begin{aligned}
\Pi_{zz} &= -\eta_0 W_{zz} \\
\Pi_{xx} &= -\frac{\eta_0}{2}(W_{xx}+W_{yy}) - \frac{\eta_1}{2}(W_{xx}-W_{yy}) - \eta_3 W_{xy} \\
\Pi_{yy} &= -\frac{\eta_0}{2}(W_{xx}+W_{yy}) - \frac{\eta_1}{2}(W_{xx}-W_{yy}) + \eta_3 W_{xy} \\
\Pi_{xy} &= \Pi_{yx} = -\eta_1 W_{xy} + \frac{\eta_3}{2}(W_{xx}-W_{yy}) \\
\Pi_{xz} &= \Pi_{zx} = -\eta_2 W_{xz} - \eta_4 W_{yz} \\
\Pi_{yz} &= \Pi_{zy} = -\eta_2 W_{yz} + \eta_4 W_{xz}
\end{aligned} \tag{55}$$

where the η coefficients are related to the plasma quantities

$$\begin{aligned}
\eta_0 &= 0.96 n_i T_i \tau_i \\
\eta_1 &= \frac{3}{10}\frac{n_i T_i}{\tau_i \omega_i^2} = \frac{1}{4}\eta_2 \\
\eta_2 &= \frac{1}{2}\frac{n_i T_i}{\omega_i} = \frac{1}{2}\eta_3
\end{aligned} \tag{56}$$

The viscous stress tensor in absence of magnetic field $\underline{\underline{\mathbf{W}}}$ is

$$\underline{\underline{\mathbf{W}}} = \left(\nabla\mathbf{u}_i + \nabla\mathbf{u}_i^\top\right) - \frac{2}{3}(\nabla\cdot\mathbf{u}_i)\,\underline{\underline{\mathbf{I}}} \tag{57}$$

With the above definitions for $\underline{\underline{\mathbf{\Pi}}}_{e,i}$, $\mathbf{q}_{e,i}$, $\mathbf{R}_{e,i}$ and $Q_{e,i}$ the system of fluid equations for electrons and ions is closed. As we have mentioned, anyway, Braginskii procedure to obtain these closure coefficients involves an expansion of the distribution function around a Maxwellian function, consequently the system must be closed to thermodynamic equilibrium. To make this happen, the relaxation process, which forces the distribution function to approach a Maxwellian, must be sufficiently fast compared to the evolution of all the fluid quantities. In other words, the general requirements for the applicability of the Braginskii closure of transport equations are that the time variation of the average plasma quantities is slow with respect to the *collision time* τ

$$\frac{d}{dt} \ll \frac{1}{\tau} \tag{58}$$

and that the spatial variation of the same quantities is small over distances of the order of that travelled by the plasma particles between collisions. This latter requirement, in case of strong magnetic field can be expressed by

$$L_\perp \gg r_L \qquad L_\parallel \gg \lambda \tag{59}$$

where r_L is the Larmor radius, λ is the particle *mean free path* and $L_\perp$ and $L_\parallel$ are respectively the characteristic variation lengths in the direction perpendicular and parallel to $\mathbf{B}$, $L_\perp \sim 1/\nabla_\perp$ and $L_\parallel \sim 1/\nabla_\parallel$.
Braginskii formulation of transport equations is perfectly placed in the framework of classical transport theory, introduced in section 2.2.1. Alternative formulations, within this classical theory, are the Balescu-Lenard [6] and the Zhdanov [84] forms for the closure coefficients.

2.4.3 *Limits of the existing models*

As we have seen in sections 2.4.1 and 2.4.2, the modeling of plasma dynamics is quite complicate even for the simplest cases, i. e. only one ionic species present in the plasma. Moreover, the validity of Braginskii fluid approximation is limited by restrictions on the time and spatial variation of the plasma properties. Although this approximation is able to usually capture quite well the edge plasma transport, some corrections are often necessary.
As discussed in section 2.2.2, transport of charged particles in the direction orthogonal to the magnetic field is not adequately described in the framework of classical transport theory: Braginskii coefficients for the cross-field transport, in fact, strongly underestimate the plasma transport in this direction with respect to experimental data. Although not understood completely, the causes of this anomalous transport can be related to the turbulent behaviour of plasma flow, characterized by extremely small spatial and temporal scales which bring the

plasma dynamics to a regime where the fluid closure described in section 2.4.2 is not a valid approximation. This enhanced cross-field transport is normally modeled as a diffusive process by means of the so-called *anomalous transport coefficients*. Since no complete theory exists to provide their correct values, two possible approaches can be followed to estimate radial anomalous coefficients: the development of dedicated *turbulence codes* for SOL plasmas allows the possibility to compute them with *transport-turbulence codes coupling* [83] or more frequently, they are considered as free parameters to fit measured experimental data for $n_{e,i}$, T_e, ϕ_p [22, 70]. The study of the dependences of the anomalous transport coefficients on the plasma variables is an active field of research from the theoretical, numerical and experimental point of view.
The second limitation of a classical description of edge plasma arises when kinetic effects become important also in the parallel direction. In SOL modeling, this can happen (a) near the sheath region, where strong gradients are present, or (b) when particular conditions of temperature and density are verified such that the particle mean-free path becomes of the same order of magnitude of the characteristic dimension of the system.

(a) Concerning the former, when describing the plasma in the Braginskii fluid approximation, the sheath region usually is not part of the domain of interest. Classical fluid equations, in fact, can not suitably model the plasma transport in the electrostatic sheath, due to the negligible collisionality and strong gradients that characterize this region. The reduction of the plasma domain up to the sheath entrance allows to impose the so-called *sheath boundary conditions* in correspondence of the target surfaces. These kind of boundary conditions correspond to impose Bohm criterion, given by equation (19), at the sheath entrance [70], neglecting of what actually happens inside the sheath region.

(b) Regarding kinetic effects affecting classical transport along the parallel direction in the SOL, instead, this problem is usually addressed introducing an artificial *flux limit* to upper-bound plasma fluxes to some fraction of the free streaming value [29, 70]. The flux limits are applied to both the parallel heat and momentum fluxes:

$$\kappa_{\parallel} = \frac{\kappa_{cl}}{1 + |q_{cl}/q_{fl}|} \tag{60}$$

where κ_{cl} is either Braginskii, Balescu or Zhdanov classical heat conductivity, $q_{cl} = -\kappa_{cl}\partial T/\partial x$ is the classical heat flux and the *limited flux* q_{fl} is

$$q_{fl} = \alpha n_e T_e^{3/2}\sqrt{m_e} \tag{61}$$

where α is an arbitrary scaling factor. The same treatment is done for the ion viscous stress tensor, to limit the momentum flux.

Another fundamental aspect to be considered is the modeling of neutral transport inside the plasma. As we will have the opportunity to discuss in the following, the most accurate treatment of neutral is provided by the solution of the kinetic Boltzmann equation, by means of Monte Carlo methods. Anyway, a fluid model can sometimes makes a reasonably good approximation, if the neutral mean free path λ_N is sufficiently small compared to the characteristic spatial scale lengths $L_{\parallel,\perp}$. When the fluid approximation is used, it is often necessary to apply the flux-limit procedure [77] to reduce the particle fluxes and take under control kinetic effects. Since neutral trajectories are not affected by the **B** direction, limits to both the parallel and perpendicular fluxes have to be considered:

$$\Gamma_N \rightarrow \frac{\Gamma_N}{[1 + |\Gamma_N/(\alpha n_N v_{th})|^{\gamma}]^{1/\gamma}} \tag{62}$$

where Γ_N is the neutral particle flux and v_{th} their thermal speed. Also in this case, α and γ are arbitrary values, which can be varied to reproduce the desired flux limitation.

2.4.4 *Numerical codes for edge plasma simulations*

Even with the simple two-fluids Braginskii model, conservation equations (41), (42) and (43) form a system of non-linear, coupled partial differential equations, which must be solved numerically. Numerical codes are then fundamental to understand the plasma behaviour in a magnetic device and their use in nuclear fusion research has different intents: (i) understand the basic physics that affects the plasma behaviour, (ii) derive the scaling of unknown quantities with respect to plasma parameters, (iii) integrate the available experimental measurements and (iv) make predictions on future devices. It is, indeed, in regard of this latter point that many computational codes have been developed to predict the behaviour of edge plasma in machine like ITER [58] and DEMO[3].

In modeling the tokamak geometry, perfect toroidal symmetry can be assumed so that the full 3D system of conservation equations (41), (42) and (43) can be reduced to a 2D problem. Many *2D multi-fluid codes* have been implemented in recent years to solve the multi-fluid analogous of the simple electron-ion Braginskii equations in the tokamak toroidal geometry. The possibility to introduce different types of ionic species in the plasma allows to account for the effects related to the presence of impurities generated by the wall erosion and sputtering, which is of fundamental importance in real magnetic fusion devices. Examples of this kind of codes are B2 [10] and its later version, B2.5 [9],

3 DEMO [24] (DEMOnstration Power Station) will be the first demonstration power plant, producing net electrical energy by nuclear fusion reactions. Contrary to ITER, which has the aim to produce a net thermal power of 500 MW, the aim of DEMO is to produce a net electric power of 100 MW (§1.2.3).

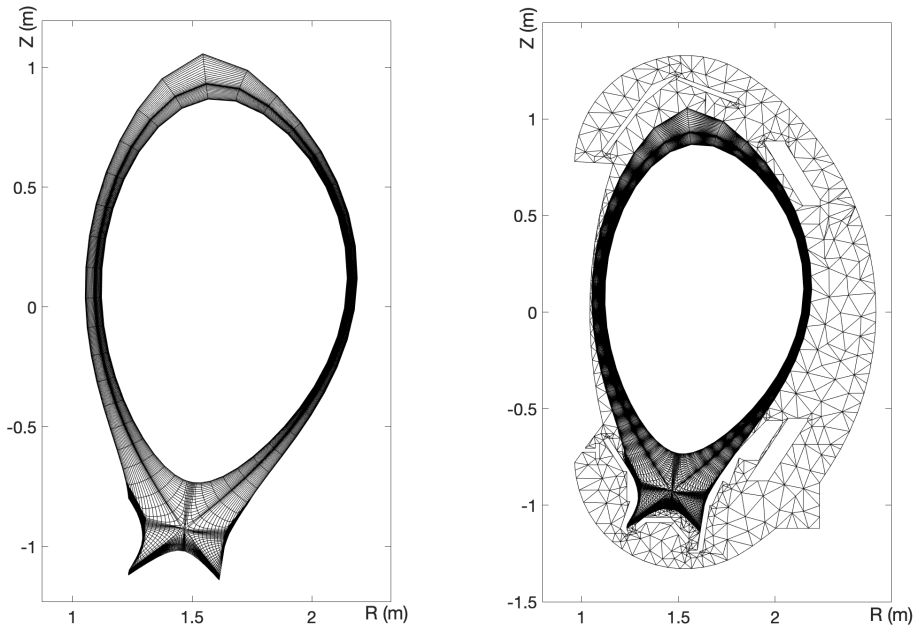

(a) *Rectangular computational mesh for a 2D edge plasma multi-fluid code.*

(b) *Triangular computational mesh for a coupled edge plasma multi-fluid code-neutral Monte Carlo code.*

Figure 13: Computational meshes for a 2D edge plasma multi-fluid-code code and 3D Monte Carlo code. Specifically, in figure 13a is represented a B2.5 mesh of the ASDEX-Upgrade tokamak (AUG) and the mesh in figure 13b is the B2.5-EIRENE triangular grid for the same machine.

EDGE2D [72], UEDGE [65] and the most recent SOLEDGE2D [12]. In these codes, multi-fluid plasma equations are solved using *finite-volume methods* on a bi-dimensional rectangular grid, representing the projections of the magnetic surfaces on a poloidal cross-section of the tokamak device. An example of B2.5 mesh for the Asdex Upgrade (AUG) tokamak is shown in figure 13a.
In section 2.3.2, we have discussed that the edge plasma is only *partially ionized* and the neutral atoms and molecules play a fundamental role. Although sometimes a fluid treatment for these species is reasonable implementing suitable corrections as described in section 2.4.3, the description of all the molecular and atomic processes presented in table 1 required more sophisticated models. The most accurate edge plasma simulations, then, compute neutral transport in the plasma using a kinetic approach, solving Boltzmann equation (25) by means of fully 3D Monte Carlo methods. Examples of Monte Carlo codes developed to simulate neutrals dynamics on specified plasma background are, for example, EIRENE [18] and Eunomia [80] codes.
Immediately after the development of the first multi-fluid and Monte Carlo codes for plasma transport, methods have been developed to produced self-consistent solutions for the edge problem, by a mixed fluid-Monte Carlo approach [3, 64]. Coupled versions of fluid-Monte Carlo codes are nowadays extensively used to simulate the scrape-off layer of real tokamaks. Besides the validation of these codes with experimental data, which has been carry out for the last decade, their use to make reliable predictions on the plasma behaviour of under-construction machines such as ITER is one of the most active fields of research and leads to the development of always more refined code versions [13, 43].

In this thesis work, the latest version of the *SOLPS (Scrape-Off Layer Plasma Simulator)*, namely the *SOLPS-ITER* [81] code, which couples the B2.5 multi-fluid plasma transport code with the EIRENE Monte Carlo code for neutral transport, will be mainly used. A detailed description of the code structure and the physics that can be simulated will be given in chapter 3.

2.5 LINEAR MACHINES IN FUSION RESEARCH

In the last few sections, the presentation of both physical models and numerical codes has been done assuming toroidal tokamak geometry. As discussed in section 2.1.1, anyway, another class of magnetic devices exist: the so-called *open configuration systems* or *linear devices*. The use of this kind of devices in the framework of magnetic nuclear fusion research is not aimed to study plasma confinement, which, as we have discussed, is intrinsically connected to the toroidal geometry of closed system. However, their deployment is of keen interest for what concerns the possibility to study plasma-material interaction and other boundary phenomena. Indeed, in linear machines it is possible to

obtain particle fluxes and densities compatible with the values expected in future fusion devices. These high fluxes and densities values, in turn, are not reached in present day tokamaks, so that nowadays linear devices provide the only means to experimentally study the effects of plasma-material interactions for future nuclear fusion reactor-like structures.

The structure of a linear device is quite simple: a cylindrical vacuum chamber is surrounded by magnetic coils in the azimuthal direction, externally induced current flows in the coils and produces a magnetic field mainly directed in the axial direction. If such a cylindrical geometry is considered, many of the concepts we have presented so far are still valid: (1) magnetic field lines are opened and directed towards suitable targets, placed in front of the basis of the cylinder so that plasma-material interaction can be effectively studied; (2) transport of charged particles is again strongly anisotropic with respect to the axial and radial directions; (3) assuming rotational symmetry around the z-axis, a bi-dimensional transport model can be used also in this case.
Among the linear devices built all over the world there are: (a) MPEX (Material Plasma Exposure eXperiment) [62] and its precursor Proto-MPEX, planned to be built at Oak Ridge National Laboratory, Tennessee in U.S. This machine uses a high-intensity plasma source based on RF technology, with the aim to cover the entire expected plasma conditions in the divertor of a future fusion reactor. (b) Magnum-PSI at the the Dutch FOM Institute for Plasma Physics Rijnhuizen designed to study ITER-relevant plasma surface interactions. Plasma in Magnum-PSI in generated by the combined effect of expanding hydrogen arc plasma and RF heating. (c) Pilot-PSI is the forerunner of Magnum-PSI, built at Dutch FOM Institute for Plasma Physics Rijnhuizen to study the production and transport of hydrogen plasma at flux densities that are required for Magnum-PSI. Recently it has been upgraded to Upgrade Pilot-PSI. (d) MAGPIE (MAGnetized Plasma Interaction Experiment) has been built in the Plasma Research Laboratory at the Australian National University, with the aim to study plasma surface interaction physics, advanced remote diagnostic development and plasma production and heating with helicon sources [25]. (e) GyM (Gyrotron Machine) is a medium-flux linear machines located at the Istituto di Fisica del Plasma (IFP), of the Consiglio Nazionale delle Ricerche (CNR) in Milan. This device has been built with the aim to study basic aspects of plasma physics, such as plasma heating and turbulence, and plasma-material interaction in the framework of magnetic nuclear fusion research.

In lights of what we have said, linear plasma devices are excellent facilities to study important aspects of boundary plasma physics and plasma interaction with solid materials. Moreover, their relative simplicity and the reduced dimensions make them much more cost effective than tokamaks.
These devices have been widely used by the nuclear fusion community to study

plasma heating mechanisms [25], diagnostic systems, plasma detachment [56], plasma-wall interaction and material modifications [48] caused by exposure to fusion-relevant plasmas.
Despite their extensive deployment in experimental investigation of plasma edge physics and PWI, the application of boundary plasma transport codes to this kind of machines have been only seldom exploited. Boundary transport codes as those described in section 2.4.4 are in fact designed and developed to simulate tokamaks and, as we will discuss in this thesis work, they are quite often not optimized for the linear geometries. Among the few works done in this context, we recall: (a) B2-EIRENE plasma transport code has been applied to MPEX to study the feasibility to reach target densities similar to those expected with burning plasmas [63]. (b) Also to Magnum-PSI, B2-EIRENE simulations were performed, with particular interest in the role of neutral species on the plasma profiles [5]. (c) SOLEDGE2D-EIRENE code has been applied to Pilot-PSI to study the role of atomic and molecular processes in plasmas. Comparisons with experimental data were also performed [39, 40]. (d) On MAGPIE, simulations were performed to study radial transport in linear machines [59]. In this case the more advanced B2.5-EIRENE code has been used. (5) First explorative studies concerning the application of the B2.5-EIRENE code to the GyM device have been performed [48].

2.6 MOTIVATIONS AND GOALS OF THIS THESIS WORK

At this point, all the elements to understand the motivations and goals of this thesis work have been introduced. To briefly summarize what has been discussed so far, in chapter 1 a general overview of the motivations behind nuclear fusion research was given, focusing both on physical and engineering issues. The chapter has been concluded with an introduction to inertial and magnetic confinement approaches, the latter being the one of interest in this thesis work. More specific issues related to magnetic confinement nuclear fusion (MCF) research have been addressed in chapter 2. In this chapter, we have focused on phenomena concerning the *edge plasma* and its interaction with the *first wall*. In this context, the fundamental need for numerical tools to simulate the boundary plasma transport was acknowledged, underlying their importance in both interpretation of experimental data and prediction of future devices characteristics. Moreover, the importance of linear plasma devices in edge plasma research was emphasized, particularly considering the possibility to apply multi-fluid plasma codes to the linear geometry, for the simulation of transport mechanisms and the evaluation of plasma characteristics. Indeed, linear machines offer a simplified, yet still physically relevant model on which transport codes can be tested and then exploited to interpret experimental results and investigate future nuclear fusion reactor characteristics.
It is within this last specific framework that this thesis has been developed.

Its general aim is to numerically investigate nuclear fusion relevant plasma through the applications of dedicated edge transport codes to linear magnetic devices. In this thesis work the latest version of the *SOLPS* package, namely the *SOLPS-ITER* code, has been used to simulate the plasma of linear plasma device *GyM (Gyrotron Machine)*. This has been developed in the frame of a collaboration between *Politecnico di Milano* and *Istituto di Fisica del Plasma, IFP - CNR*, where GyM was designed.

Numerical simulation of a plasma device are aimed to develop reliable tools to help the interpretation of experimental results and to make predictions on future devices. Comparison between experiments and simulations can help giving an insight on the physical mechanisms active in determining the observed plasma behaviour. Moreover, the possibility offered by linear devices to reproduce plasma characteristics similar to those expected in future nuclear fusion machines, gives the opportunity to forecast many important characteristics of boundary plasmas and PWI. For these reasons, the application of boundary plasma transport codes also to linear devices is becoming of wide interest inside the nuclear fusion community. The primary intent of this thesis work has been the demonstration of the applicability of the SOLPS-ITER code, to medium flux plasmas produced in the linear device GyM. To our knowledge, this version of the code has not yet been applied to simulate plasma transport in linear machines and, since edge plasma codes like SOLPS are developed specifically for tokamak geometry, their application to linear devices is often not straightforward. Furthermore, the regime of densities that can be reached in GyM is quite different from those usually encountered in tokamak SOL and in other linear devices producing diverter-relevant plasmas. Therefore, the validity of many code approximations should be specifically tested for GyM.

A global description of the SOLPS-ITER code considering its more common applications devoted to the simulation of tokamak SOLs is given in chapter 3. When dealing with linear devices, many of the input files that have to be supplied to the code must be generated without the support of graphical-interface tools developed for tokamaks. In particular, dedicated programs for the computation of the equilibrium magnetic field and the mesh construction have been written, following the same approach used in previous applications of the SOLPS package to linear machines [48]. These issues, strictly related to the modeling of the GyM device, will be addressed in chapter 4.
Results of the performed simulations will be presented in chapter 5. First simplified test-simulations have been performed, treating both plasma and neutrals with the fluid approximation. In this case, argon plasmas have been simulated, exploiting simplifications related to the atomic nature of this gas. Moreover, the physical picture was also untangled, neglecting both the effects of pumping and puffing of neutral particles. The focus of the standalone simulations

has been on the numerical behaviour of the code, analyzing convergence to a stationary solution and the effects of time and space discretization.
Afterward, kinetic description of neutral particles has been employed, successfully exploiting the coupled fluid-Monte Carlo version of the code for the modeling of both argon and deuterium plasmas. A sensitivity analysis of some of the more relevant physical parameters has been carried out in the case of Ar plasmas. The neutrals content, the anomalous transport coefficients and the external power have been varied, with the aim to understand their effects on plasma parameters such as electron temperature, density and plasma potential. A first attempt to compare the available experimental data for both Ar and D plasmas with the simulation results has been successfully done. Finally in chapter 6, conclusions on the results obtained are drawn and future perspectives and developments of this thesis work are pointed out.

3 SOLPS-ITER CODE

Because of physical complexities presented in chapter 2, the experimental investigation of edge plasma physics and plasma wall interaction has to be supported by the design and application of increasingly refined numerical models. As we have said in section 2.4, both fluid models, to describe the plasma evolution, and kinetic neutral transport models, exploiting Monte Carlo methods, have to be implemented in boundary plasma transport codes. In order to combine the most recent advances in both the fluid and kinetic codes, the *ITER Organization (IO)* has sponsored the development of a new code version, named *SOLPS-ITER* [81], which couples the most recent MPI parallelized EIRENE code with the B2.5 fluid plasma solver, already used in the SOLPS5.2 package [66].
In this chapter this code will be described in some details. After a brief introduction in section 3.1, its structure is presented in section 3.2. Here, the main implemented modules are described, and all the necessary input files will be illustrated. In section 3.3, the physical models behind the code are presented. In particular in section 3.3.1, it is shown how the Braginskii fluid equations (41), (42) and (43) are written in a suitable curvilinear coordinate system exploiting toroidal symmetry, while in section 3.3.2, the neutral Boltzmann kinetic equation (25) is written in the form used to apply Monte Carlo methods. Finally in section 3.3.3, it is explained how the transport of different species is computed by EIRENE.

3.1 INTRODUCTION TO THE CODE: STANDALONE AND COUPLED MODES

The SOLPS-ITER code is the latest development of the SOLPS (Scrape-Off Layer Plasma Simulator) boundary plasma transport code, coupling the B2 or B2.5 multi-fluid code and the EIRENE Monte Carlo neutral code. The original version of the SOLPS package has been developed starting from 1987, but various improvements have been implemented since then. The different versions of the code are shown in table 2, pointing out the fluid-Monte Carlo coupling corresponding to each package. As already discussed in section 2.4.4, the B2 code, and its latest version B2.5, are 2D fluid code based on a set of transport equations, equivalent to the Braginskii equations [11]. The first version of the code was originally developed by B. Braams during his Ph.D. thesis [10] and then improved and firstly coupled with the EIRENE Monte Carlo code by M. Baelmans during her PhD thesis [47]. However, the model proposed by Braams

	EIRENE$_{96}$ **EIRENE**$_{99}$	**EIRENE**$_{facelift}$	**EIRENE**$_{2010}$
B2 (IO+FZ Julich)	SOLPS4.0	SOLPS4.2	SOLPS4.3
B2.5 (IPP)	SOLPS5.0	SOLPS5.1	
B2.5 + drifts (St. Petersburg)	SOLPS5.2		SOLPS-ITER

Table 2: All the implemented versions of the SOLPS package. The SOLPS-ITER code is the most complete version, coupling the latest multi-fluid transport code, accounting for both drifts and currents, and the parallelized $EIRENE_{2010}$ code version.

and Baelmans contains several simplifications of the actual plasma fluid equations and in the following years several mechanisms originally neglected, such as currents and drifts, have been added to the code by different groups.
Regarding the EIRENE code, the first version was presented in 1992 [17] and also in this case, many updates have been introduced since then. In particular, the latest version includes: large variety of many atomic and molecular processes (also thanks to the development of specific external databases), the possibility to simulate radiation losses and the neutral-neutral and photon-neutral non linear collision processes and finally, the possibility to run the code using the parallelized version, in order to strongly reduce the computation time.

The SOLPS-ITER code can be used in *standalone* or *coupled mode*.

- **B2.5 standalone run**: when this mode is used, only the multi-fluid code B2.5 is run and Braginskii-like fluid equations are solved for both charged and neutral particles. In this case, the species that can be taken into account are limited by the "atomic nature" of the fluid code: B2.5 can, in fact, consider only charged atomic ions and the corresponding neutral atom, but no molecules. Consequently the external database of reference for a standalone run is usually the ADAS [1] database for atomic processes. The multi-fluid nature of B2.5, anyhow, allows to simulate different atomic species, each of them with more than one state of charge. This is important in edge plasma simulations, since it enables to reproduce the effects of impurities on the plasma. Impurities in a magnetic device can be generated from sputtering of the PFCs or they can be artificially injected in the plasma as neutral gases mitigate particle and heat fluxes towards the first wall. For each charged state that is simulated dedicated density and momentum conservation equations are solved, while a single ion temperature equation is solved, approximating all the ion species as isotherm.

◇ **B2.5-EIRENE coupled run**: this mode represents the coupled fluid-Monte Carlo version of the code and it is nowadays one of the more advanced tools to simulate edge plasmas. Charged atomic ions are described using the fluid model, while the transport of neutral species and their interaction with plasma particles is implemented by means of Monte Carlo methods. The latest version of the EIRENE code allows to take into account not only atoms, but also molecules and molecular ions, such as $H_2{}^+$. To suitably describe all the relevant collision processes, databases like HYDHEL [20] and AMJUEL [19] for atomic and molecular processes are used. The possibility offered by the SOLPS code to simulate impurities requires other two elements: (a) the introduction of models for the impurities production by physical and chemical sputtering [16] according to the wall composition; (b) dedicated databases, describing collision processes among a given impurity family, such as hydrocarbons [36, 37], and plasma particles. The sputtering yield is usually computed by EIRENE from the TRIM (TRansport of Ions in Matter) code
The iterative coupling procedure between B2.5 and EIRENE consists in the following steps: (i) preparation of the numerical grid structures for the two codes (figure 13b), (ii) computation of the source and sink terms into the fluid balance equations for each plasma species in terms of Monte Carlo responses, (iii) solution of the plasma balance equations in terms of density, velocities and temperatures and (iv) update of the kinetic distributions $f_{pl}(\mathbf{x}, \mathbf{v}, t)$ for the host medium, i. e. the plasma, which is used to evaluate the collision terms at step (ii). The complete work-flow for a coupled B2.5-EIRENE run is shown in figure 14.

◇ **EIRENE standalone run**: in this mode, the transport of neutral species is simulated performing a single Monte Carlo iteration on a fixed plasma background. The plasma background in turn has to be provided by means of the `fort.31` file, that can be created at the end of a B2.5 standalone or coupled run.

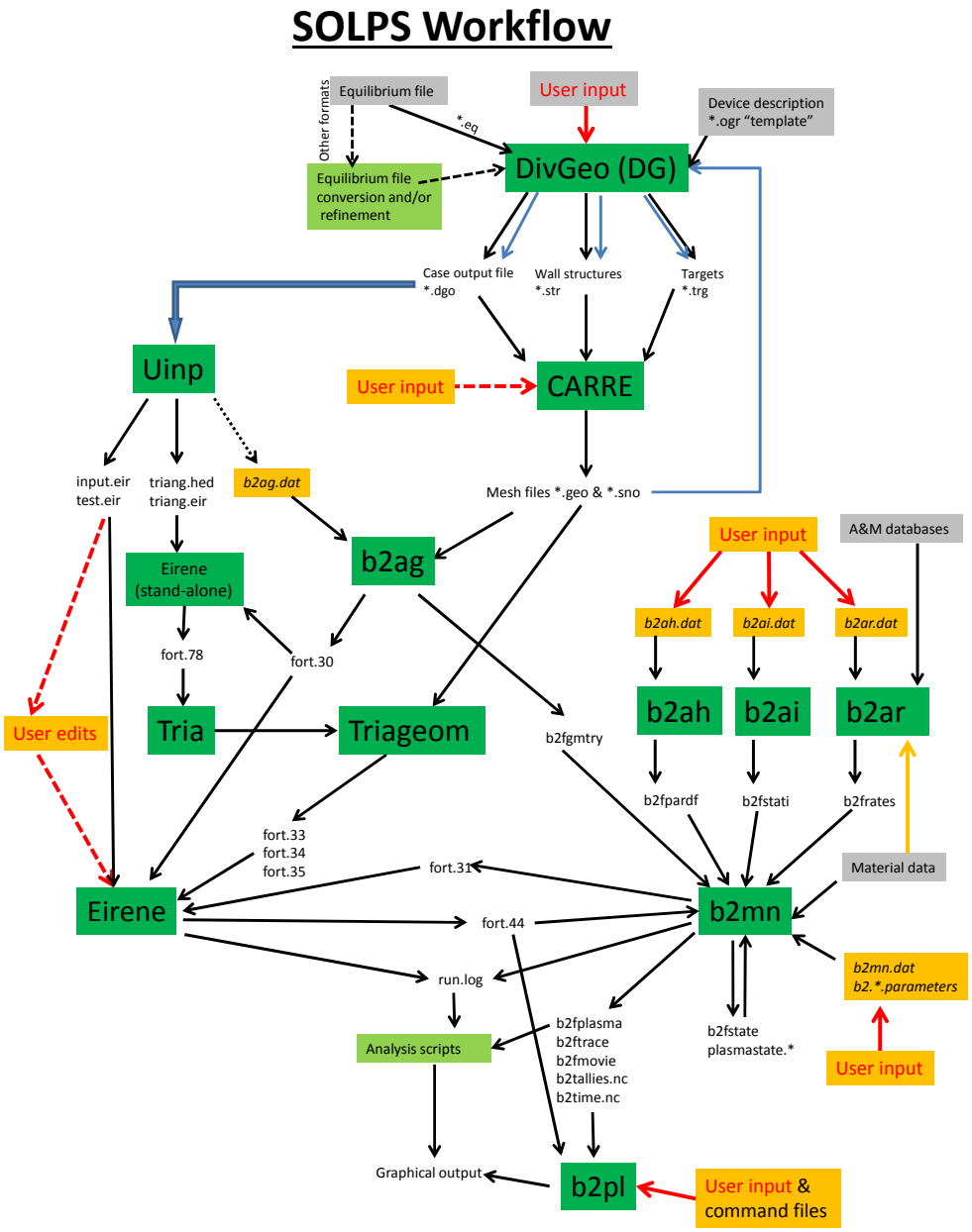

Figure 14: SOLPS-ITER workflow scheme for a coupled run. Many of the modules in green are described in section 3.2.

3.2 STRUCTURE OF THE CODE

In this section, we will describe the main packages of the code, many of which have been used in the context of this thesis work. The SOLPS-ITER directory has the following global structure:

```
SOLPSTOP
+---doc
|  +---SOLPS_2002_Course
|  +---solps
+---scripts
|  +---commands
|  +---matlab
|  +---palettes
+---scripts.local
+---modules
|  +---Sonnet-light
|  +---fxdr
|  +---Triang
|  +---Uinp
|  +---Carre
|  +---amds
|  +---B2.5
|  +---solps4-5
|  +---DivGeo
|  +---Eirene
+---lib
|  +---ITER.ifort64
+---runs
+---SETUP
```

The main packages are contained in the `/modules` folder.

- ◇ **DivGeo**, is a graphical user interface used for the preparation of the main inputs. This package requires the upload of the equilibrium poloidal magnetic flux surfaces. This equilibrium configuration is referred to a specific experimental scenario for a fixed instant of time. The requirement is that the equilibrium magnetic flux surfaces intersect the solid wall only at the divertor targets. As one will see, this means that the plasma computational domain can not extend to the main chamber wall. The two dimensional poloidal cross-section of the first wall of the tokamak is also needed. Such cross-sections are available in the SOLPS databases or can be imported in `DivGeo`, from a technical drawing file.

- ◇ **Carre** is the mesh generating program for B2.5 [49]. It uses the output files created by DivGeo to generate the curvilinear rectangular grid align-

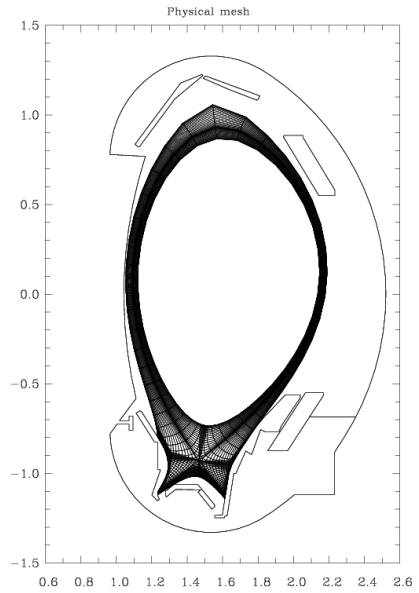

(a) *Physical mesh of B2.5.*

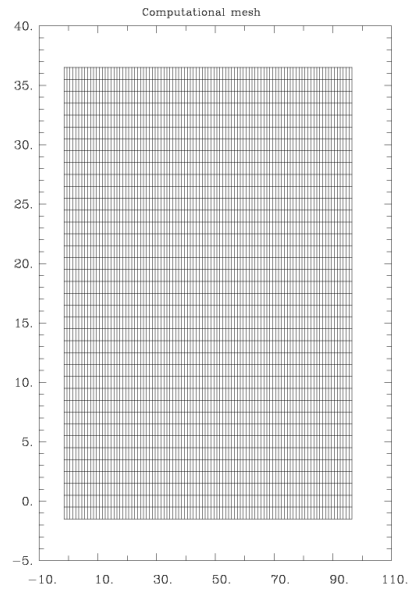

(b) *Computational mesh of B2.5.*

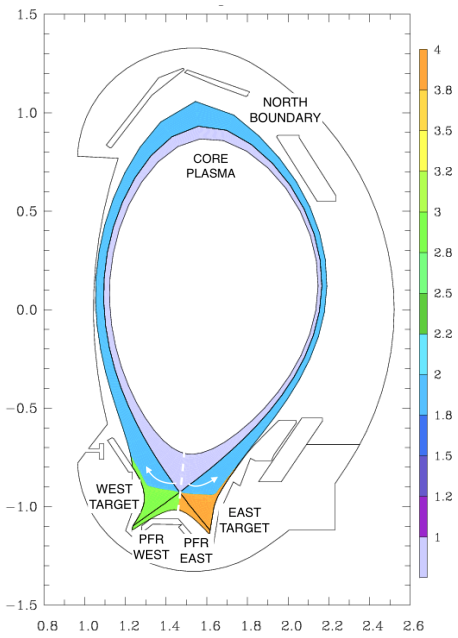

(c) *Regions on the physical mesh.*

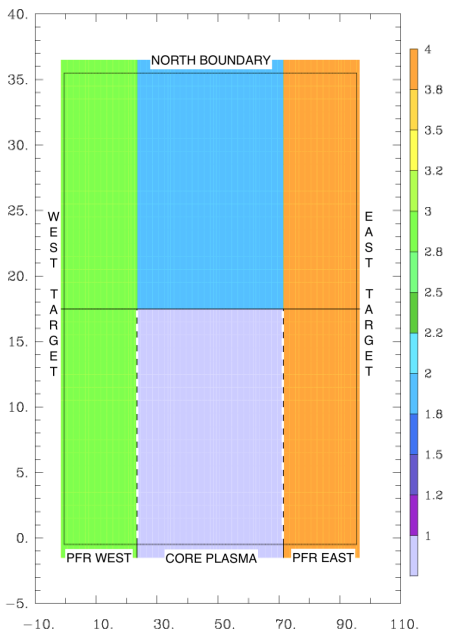

(d) *Regions on the computational mesh.*

Figure 15: Physical and computational meshes generated by the Carre package and domain separations into *regions*.

ing two sides of the mesh cells along the magnetic field lines as shown in figure 15a: this is the co-called *physical domain* for the simulations. Numerical calculations, instead, are performed on the topologically rectangular mesh shown in figure 15b, called *computational domain*. To move from the physical cross-section of the field lines on the poloidal plane to the full rectangular computational domain, the grid is *cut* in proximity of the *X-point*. The cutting procedure for a single-null configuration is shown in figure 15c and figure 15d: the different regions thus obtained are shown on the physical and computational mesh respectively. Furthermore, transformation between curvilinear and rectangular mesh cells is provided through metric coefficients that are included in the output of Carre. The grid resolution can be chosen by the user, remembering that a fine resolution is required when strong gradients in plasma parameters are expected: commonly close to the targets and around the X-point.

◇ **Triang** is the program used to build the triangular mesh for B2.5-EIRENE coupled mode, using the input from both DivGeo and Carre programs. This grid, contrary to the one used to solve plasma fluid equations, extends allover the 2D-poloidal projection of the vacuum chamber. The steps performed by the program are the following: (i) definition of a closed line representing the borders of the vacuum chamber in the (R,Z) plane; (ii) triangularization of both in the rectangular Carre grid and in the remaining vacuum region inside the vessel; (iii) merging of the two triangular grids to obtain the final result shown in figure 13b.

◇ **B2.5** is, together with EIRENE, one of the two fundamental packages of the code. It is the computational multi-fluid part of the code that solves the plasma transport equations. The code is entirely written in *FORTRAN 90* and it is based on *finite volume discretization* methods. At each time step, volumetric and surface source terms are computed, solving for momentum conservation, continuity, energy conservation and finally again for the continuity equation. The above procedure is repeated for a number of *internal iterations* to relax the equation solutions before proceeding to the next time step, or *external iteration*. The convergence of this iterative process can be checked by monitoring the *norm of the residuals* for each conservation equation. In the following, we will be interested in the *steady state solution*, corresponding to the state where no major variation in time of the plasma parameters is observed. This must include steady state of the densities, temperatures, energy and particle fluxes at various locations in addition to the total particle and energy content of the plasma.
Among the various routines that B2.5 calls during the run, the *auxiliary programs* `b2a*` requires the main input files for the multi-fluid simulation. These input files, given with extensions `.dat`, `.parameters` or `.profile`,

are written in `ASCII` format and therefore directly editable by the user to specify geometry, initial and boundary conditions and other parameters of interest for the simulation. A brief description of these files is given here:

- `b2ag.dat` is the the pre-processor input file for the `b2ag` auxiliary program. It is used to set up the geometry of the problem, providing information like the number of cells in the grid, the symmetry of the problem and the mesh file to be read. By running the `b2ag` program, the geometry file `b2fgmtry` is written.
- `b2ah.dat` is the input file for the `b2ah` auxiliary program and contains information about the different species that are considerd, boundary conditions and transport coefficient specifications. The `b2ah` program prepares the default physics parameters file, `b2fpardf`.
- `b2ar.dat` specifies the ranges of densities and temperatures for atomic physics tables, taken from different atomic physics packages. The default option is the use of ADAS (Atomic Data and Analysis Structure) [1]. The file obtained by the running of `b2ar` is `b2frates`.
- `b2ai.dat` sets up the default initial plasma states, specifying a homogeneous value for the electron and ion temperature, and neutral and ion densities; `b2ai` prepares the default initial plasma state file, `b2fstati`.
- `b2mn.dat` is the main input file and determines the *operating regime of the code*. First lines are a label containing a brief description of the case, followed by the *switches* required to obtain a given behaviour of the code. The switches are divided into six broad categories, according to the role they have on the code performance: *Geometry*, *Physics*, *Run*, *Output*, *Numerics* and *Atomic Physics*.
- `b2.boundary.parameters` specifies the boundary segments present in the simulated region and the corresponding boundary conditions for each of the balance equation. This name-list is actually read, only if the string `'b2stbc_boundary_namelist'` is set to `1` in `b2mn.dat`, otherwise boundary conditions are read from the file created by `b2fpardf`.
- `b2.neutrals.parameters` specifies data and parameters regarding the treatment of neutral species.
- `b2.numerics.parameters` specifies the settings for the numerical methods used for the solution of the equations in the different regions of the domain.
- `b2.transport.parameters` specifies the values for the anomalous transport coefficients. These can be either constant or with a specific

radial profile, which is defined in the `b2.transport.inputfile` file. This file is read only if the string `'b2tqna_inputflie'` is set to `1` in `b2mn.dat`, otherwise transport coefficients are read from the file created by `b2fpardf`.

– `b2.sources.profile` specifies arbitrary radially and axially dependent external source profiles. The types of sources that can be defined are particle source, momentum source, electron heat source, ion heat source, electric charge source and non-ambipolar electric particle source. This file is read only if the string `'b2sral_inputflie'` is set to `1` in `b2mn.dat`.

◇ **EIRENE** is the Monte Carlo kinetic code for neutrals transport, written in *FORTRAN 90*. As already stated in section 2.4.4, the Monte Carlo kinetic part of the code solves the transport equations for neutral particles in 3D volumes of arbitrary geometry. When the code is coupled to B2.5, anyway, the third toroidal dimension of the code is neglected and the volume of each cell of the mesh is computed by taking a fixed length $d\phi$ in the toroidal direction. The main input required by this package is a formatted file called `input.dat`.
The `input.dat` file is produced as output by DivGeo, also using the geometry outputs from both Carre and Triang. The file is made up of fifteen blocks:

```
*** 1. Input data for operating mode
*** 2. Input data for standard mesh
*** 3A. Input data for "Non-default Standard Surfaces"
*** 3B. Input data for "Additional Surfaces"
*** 4. Input data for species specification and atomic physics module
*** 5. Input data for plasma background
*** 6. Input data for surface interaction models
*** 7. Input data for initial distribution of test particles
*** 8. Additional data for some specific mesh zones
*** 9. Data for statistics and non-analog methods
*** 10. Data for additional volumetric and surface averaged tallies
*** 11. Data for numerical and graphical output
*** 12. Data for plasma diagnostic module DIAGNO
*** 13. Data for nonlinear and time-dependent mode
*** 14. Data for interfacing with routine INFUSR
*** 15. Data for interfacing with routine GEOUSR
```

The last two blocks are specific for the external fluid code to which EIRENE is coupled, in this case B2.5. Moreover, it is important to define the terminology which appears in the above block structure. In particular the *standard mesh* is the mesh where the plasma transport equations are solved, i. e. the rectangular grid constructed by the Carre program;

the boundaries of this mesh are the *non-default standard surfaces*, and represent the boundaries up to which the plasma can extend. The *additional surfaces*, instead, are the other extra-plasma boundaries, such as the walls of the vacuum vessel or other segments of the domain, for example related to gas puffing segments or pumping systems.

The one just described are the fundamental packages of the code and are implemented for tokamak geometry. As we will see in chapters 4 and 5, not every of them are optimized for liner devices.

3.3 SOLPS-ITER PHYSICS

In this last part of the chapter, we want to briefly summarize the equations solved by the code. To do so we have to introduce the curvilinear reference frame used to model the tokamak geometry and understand how to transform 3D fluid equations (41), (42) and (43) into a closed set of 2D transport equation in curvilinear coordinates (§3.3.1). Concerning the kinetic treatment of neutrals, first a general introduction to the Monte Carlo method applied to solve Boltzmann neutral equation will be given (§3.3.2) and then the we will see how the code solve for the transport of different atomic and molecular species (§3.3.3).

3.3.1 *B2.5 equations*

Our aim here is to construct a reduced set of 2D fluid transport equation assuming toroidal symmetry, starting from the 3D Braginskii equations. When the tokamak geometry has to be described, two different reference frames, shown in figure 16, are usually adopted. In either cases, the first direction considered is radial and cross-field, designated by coordinate r. In choosing the second coordinate, instead, two different approaches can be followed: (a) $s_{\parallel}$, measured along $\mathbf{B}$; (b) s_θ, along the projection of $\mathbf{B}$ in the poloidal plane, i. e. $s_\theta = s_{\parallel}(B_\theta/B)$. The first choice is called *dynamical frame*, since the particle transport along the field lines is followed; in this case, the third direction composing the orthogonal triad of coordinates is tangent to the flux surface but orthogonal to thee magnetic field. This direction is usually indicated with $s_\perp$ and it is called *diamagnetic direction*. The second choice is the *geometrical frame*, representing the directions along and orthogonal to the projection of the magnetic field lines on the poloidal plane. The geometrical frame is shown in figure 17. In B2.5 the poloidal coordinate θ is indicated with x, the radial one r, orthogonal to the flux surfaces, with y and the toroidal one ϕ with z. In the following we will use this nomenclature. As, we will see, B2.5 equations contain a mixture of both dynamical and geometrical frame coordinates.

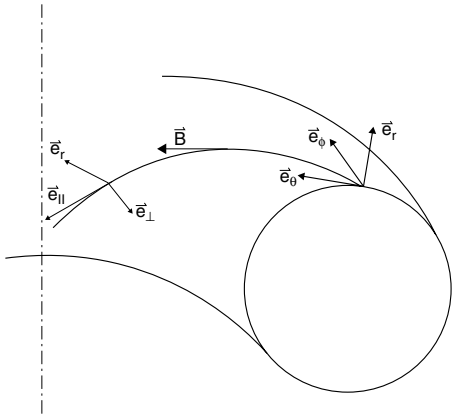

Figure 16: The two local reference frame use in tokamas description: the triad $(\mathbf{e}_{\|}, \mathbf{e}_{\perp}, \mathbf{e}_r)$ are the so-called *dynamical frame*, while the $(\mathbf{e}_r, \mathbf{e}_\theta, \mathbf{e}_\phi)$ is the so-called *geometrical frame*.

If we consider a pure hydrogen plasma with neutral particles and we suppose the magnetic field to be static and known, then the plasma transport problem has ten unknowns in total: the ion density, equal to the electron density if charge neutrality is assumed, the ion and electron temperatures, the three components of the ion flow velocity, the three components of the current density vector and, finally, the electrostatic potential. The corresponding ten equations to be solved are the conservation equations (41), (42) and (43) for particle density, energy and momentum for both the electrons and ions and Poisson equation. Local parallel transport coefficients are assumed to be classical, so that Braginskii expression can be used, moreover, if kinetics effects become important, flux-limits are applied as describe in section 2.4.3. Cross-field transport is instead assumed to be anomalous and, as we have seen in section 3.2, the values of the corresponding transport coefficients can be specified in the input files.
In Appendix C, a basic treatment of vector algebra and calculus in curvilinear coordinates is given. There, the main transformations needed to write the Braginskii equations from cartesian to curvilinear notation are pointed out. In the following we will use many of the concepts defined there.
Considering the geometrical frame, the metric coefficients are h_x, h_x and h_z and $\sqrt{g} = h_x h_y h_z$. Moreover the components of the local unit-basis vector along the magnetic field is $\mathbf{b} = \mathbf{B}/B$ and its poloidal and toroidal components are respectively $b_x = B_x/B$ and $b_z = B_z/B$.
The poloidal ion velocity V_x is given by $V_x = b_x V_{\|} + b_z V_{\perp}$. The perpendicular ion velocity $V_\perp$ and the radial component V_r can be obtained taking the cross product of the momentum balance equation for ions with the unit vector

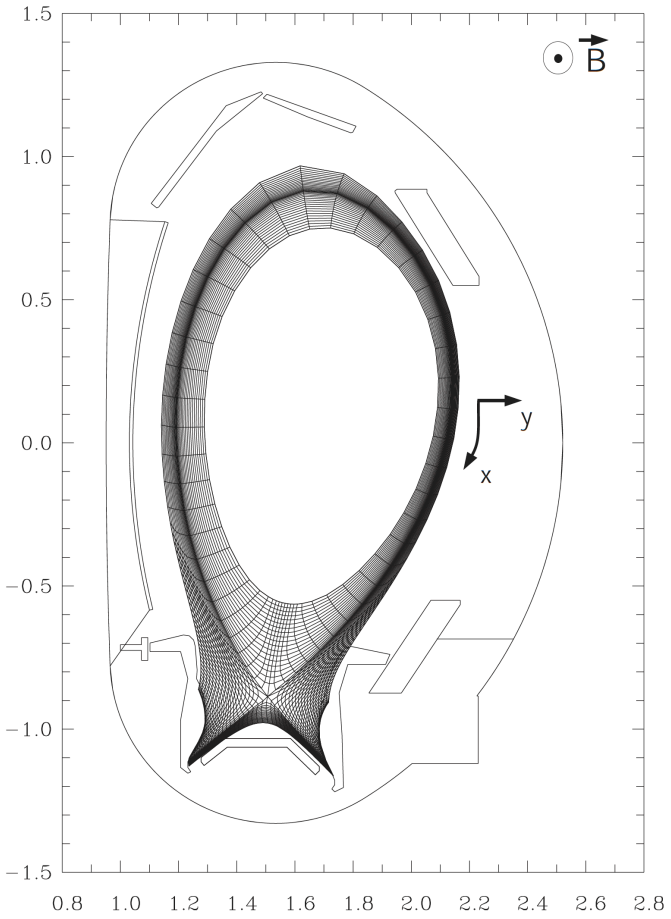

Figure 17: Geometrical reference frame used by B2.5: the radial coordinate is indicated by y and the poloidal coordinate by x.

b and projecting the results on the radial and perpendicular direction. The result, considering the Braginskii expression for the friction force is

$$V_\perp = V_\perp^{(a)} + V_\perp^{(dia)} + V_\perp^{(in)} + V_\perp^{(vis)} + V_\perp^{(s)} \tag{63}$$

$$V_y = V_y^{(a)} + V_y^{(dia)} + V_y^{(in)} + V_y^{(vis)} + V_y^{(s)} \tag{64}$$

Among these, $V^{(a)}$ is the so-called *ambipolar velocity*. Contributions to this velocity do not depend on the sign of the electric charge of the species considered and they are identical for both electrons and ions. In presence of anomalous transport it is given by

$$V_\perp^{(a)} = V_\perp^{\mathbf{E}\times\mathbf{B}} - \frac{D}{T_e+T_i}\frac{b_z}{h_x}\left(\frac{1}{n}\frac{\partial p}{\partial x} - \frac{3}{2}\frac{\partial T_e}{\partial x}\right) - D_{AN}^n \frac{b_z}{h_x n}\frac{\partial n}{\partial x} - D_{AN}^p \frac{b_z}{h_x n}\frac{\partial p_i}{\partial x} \tag{65}$$

$$V_y^{(a)} = V_y^{\mathbf{E}\times\mathbf{B}} - \frac{D}{T_e+T_i}\frac{1}{h_y}\left(\frac{1}{n}\frac{\partial p}{\partial y} - \frac{3}{2}\frac{\partial T_e}{\partial y}\right) - D_{AN}^n \frac{1}{h_y n}\frac{\partial n}{\partial y} - D_{AN}^p \frac{1}{h_y n}\frac{\partial p_i}{\partial y} \tag{66}$$

where $D = (T_e + T_i)\nu_{ei}/eb\omega_{ei}$ is the classical diffusion coefficient. The *diamagnetic velocity* $V^{(dia)}$, related to the term $\mathbf{B}\times\nabla p$, is

$$V_\perp^{(dia)} = -\frac{1}{enB}\frac{1}{h_y}\frac{\partial(nT_i)}{\partial y} \qquad V_y^{(dia)} = \frac{B_z}{enB^2}\frac{1}{h_x}\frac{\partial(nT_i)}{\partial x} \tag{67}$$

Actually, these expression have been modified in the most recent version of the code to reduce numerical instabilities when dealing with *H-mode* regimes [66]. The $V^{\mathbf{E}\times\mathbf{B}}$ velocity caused by the $\mathbf{E}\times\mathbf{B}$-drift is

$$V_\perp^{\mathbf{E}\times\mathbf{B}} = -\frac{1}{B}\frac{1}{h_y}\frac{\partial\phi}{\partial y} \qquad V_y^{\mathbf{E}\times\mathbf{B}} = \frac{B_z}{B^2}\frac{1}{h_x}\frac{\partial\phi}{\partial x} \tag{68}$$

Finally the non-ambipolar velocity terms $V^{(in)}$, $V^{(vis)}$ and $V^{(s)}$, caused respectively by inertia, viscosity and ion-neutral friction, are usually expressed in terms of current densities:

$$\mathbf{V}^{(in)} = \mathbf{j}^{(in)}/en \qquad \mathbf{V}^{(vis)} = \mathbf{j}^{(vis)}/en \qquad \mathbf{V}^{(s)} = \mathbf{j}^{(s)}/en \tag{69}$$

If we neglect the effects of drifts, i. e. $V^{(dia)} \simeq 0$ and $V^{\mathbf{E}\times\mathbf{B}} \simeq 0$ and we made the quite common hypothesis of *ambipolarity*, which means considering equal velocities for electrons and ions and consequently null current in the plasma $\mathbf{j} \simeq 0$, the original set of equations proposed by Braams and Baelmans is recovered.

With the definitions given above, the density conservation equation (41) becomes

$$\frac{\partial n}{\partial t} + \frac{1}{\sqrt{g}}\frac{\partial}{\partial x}\left(\frac{\sqrt{g}}{h_x} n \left(b_x V_\parallel + b_z V_\perp\right)\right) + \frac{1}{\sqrt{g}}\frac{\partial}{\partial y}\left(\frac{\sqrt{g}}{h_y} n V_y\right) = S_n \tag{70}$$

where S_n is the source term due to neutral ionization.
The ion parallel momentum equation, is obtained taking the component in the **b** direction of Braginskii momentum equation. To obtain the final form that we report here, many assumption has been made on the relative importance of different velocities and their associated flux [66, 67].

$$\begin{aligned} m_i\Bigg[&\frac{\partial\left(nV_\parallel\right)}{\partial t}+\frac{1}{h_z\sqrt{g}}\frac{\partial}{\partial x}\left(\frac{h_z\sqrt{g}}{h_x}n\left(V_\perp b_z+b_xV_\parallel\right)V_\parallel\right)+\\ &+\frac{1}{h_z\sqrt{g}}\frac{\partial}{\partial y}\left(\frac{h_z\sqrt{g}}{h_y}nV_yV_\parallel\right)\Bigg]=-\frac{b_x}{h_x}\frac{\partial\left(nT_i\right)}{\partial x}-b_x\frac{en}{h_x}\frac{\partial\phi}{\partial x}+F_k+\\ &+\frac{4}{3}b_xB^{3/2}\frac{1}{h_x}\frac{\partial}{\partial x}\left[\frac{\eta_0b_x}{B^2}\frac{\partial\left(\sqrt{B}\left(V_\parallel+b_xV_\perp^{(dia)}+b_xV_\perp^{\mathbf{E}\times\mathbf{B}}\right)\right)}{h_x\partial x}\right]+\\ &+B^{3/2}b_x\frac{1}{h_x}\frac{\partial}{\partial x}\left[\frac{b_x}{\nu_{ii}B^2}\frac{\partial\left[\sqrt{B}\left(q_{i,\parallel}+b_xq_{i,x}^{(dia)}\right)\right]}{h_x\partial x}\right]+\\ &+\frac{1}{h_z\sqrt{g}}\frac{\partial}{\partial y}\left(\frac{h_z\sqrt{g}}{h_y^2}\eta_2\frac{\partial V_\parallel}{\partial y}\right)+\\ &+\frac{1}{h_z\sqrt{g}}\frac{\partial}{\partial x}\left(\frac{h_z\sqrt{g}}{h_x^2}\eta_2\frac{\partial V_\parallel}{\partial x}\right)+S_{i\parallel}^m+R_{ei,\parallel} \end{aligned} \tag{71}$$

where F_k is the *Coriolis force*, the fourth and fifth terms on the RHS of equation (71) represent the parallel viscosity and η_0 is the classical parallel viscosity coefficient. The fifth terms is not present in Braginskii momentum equation and represents a *neoclassical* correction of the parallel Braginskii viscosity, strictly related to the tokamak toroidal geometry. The perpendicular viscosity is represented by the following two terms and η_2 is the classical perpendicular viscosity coefficient, usually replaced by the anomalous value $\eta_2 = nm_iD_{AN}$. Finally, $S_\parallel^m$ is the momentum loss due to ion-neutrals interaction or neutral beam injection and $R_{ei,\parallel}$ is the classical Braginskii electron-ion friction term.
When solving the electron momentum equation, it is common to neglect electron inertia in the Braginskii momentum equation. This procedure allows to obtain the so-called *generalized Ohm law* [68]. If we consider the parallel component of these equation, the parallel current has the form [67]:

$$j_\parallel=\sigma_\parallel\left[\frac{b_x}{e}\frac{1}{h_x}\left(\frac{\partial nT_e}{n\partial x}+0.71\frac{\partial T_e}{\partial x}\right)-\frac{b_x}{h_x}\frac{\partial\phi}{\partial x}\right] \tag{72}$$

The total current density is a sum of contributions from pressure gradient, also called *diamagnetic term* $\mathbf{j}^{(dia)}$, inertia $\mathbf{j}^{(in)}$, gyroviscosity $\mathbf{j}^{(vis)}$ and neutral friction $\mathbf{j}^{(s)}$:

$$\mathbf{j}=\mathbf{j}^{(dia)}+\mathbf{j}^{(in)}+\mathbf{j}^{(vis)}+\mathbf{j}^{(s)}+\mathbf{j}_\parallel \tag{73}$$

Beside $\mathbf{j}_\parallel$, the other current terms are obtained from the *current continuity equation*:

$$\frac{1}{\sqrt{g}}\frac{\partial}{\partial x}\left(\frac{\sqrt{g}}{h_x}j_x\right)+\frac{1}{\sqrt{g}}\frac{\partial}{\partial y}\left(\frac{\sqrt{g}}{h_y}j_y\right)=0 \tag{74}$$

For a full derivation of the various terms we refer to [21, 66, 67]. Finally, the energy balance equations are

$$\begin{aligned}\frac{3}{2}\frac{\partial\left(nT_e\right)}{\partial t}+\frac{1}{\sqrt{g}}\frac{\partial}{\partial x}\left(\frac{\sqrt{g}}{h_x}q_{e,x}\right)+\frac{1}{\sqrt{g}}\frac{\partial}{\partial y}\left(\frac{\sqrt{g}}{h_y}q_{e,y}\right)+\\ +\frac{nT_e}{\sqrt{g}}\frac{\partial}{\partial x}\left[\frac{\sqrt{g}\,b_x}{h_x}\left(V_\parallel-\frac{j_\parallel}{en}\right)\right]=\\ Q_e+nT_eB\frac{1}{h_xh_y}\left[\frac{\partial\phi}{\partial y}\frac{\partial}{\partial x}\left(\frac{1}{B^2}\right)-\frac{\partial\phi}{\partial x}\frac{\partial}{\partial y}\left(\frac{1}{B^2}\right)\right]\end{aligned} \tag{75}$$

for electrons, and

$$\begin{aligned}\frac{3}{2}\frac{\partial\left(nT_i\right)}{\partial t}+\frac{1}{\sqrt{g}}\frac{\partial}{\partial x}\left(\frac{\sqrt{g}}{h_x}q_{i,x}\right)+\frac{1}{\sqrt{g}}\frac{\partial}{\partial y}\left(\frac{\sqrt{g}}{h_y}q_{i,y}\right)+\frac{nT_i}{\sqrt{g}}\frac{\partial}{\partial x}\left(\frac{\sqrt{g}}{h_x}v_\parallel b_x\right)=\\ \frac{3m_e}{m_i}n\nu_{ei}\left(T_e-T_i\right)+\frac{\eta_0}{3}\left(2b_x\frac{1}{h_x}\frac{\partial V_\parallel}{\partial x}\right)^2+\\ +nT_iB\frac{1}{h_xh_y}\left[\frac{\partial\phi}{\partial y}\frac{\partial}{\partial x}\left(\frac{1}{B^2}\right)-\frac{\partial\phi}{\partial x}\frac{\partial}{\partial x}\left(\frac{1}{B^2}\right)\right]\end{aligned} \tag{76}$$

for the ions. The expressions for the heat fluxes $q_{e,x}$, $q_{e,y}$, $q_{i,x}$ and $q_{i,y}$, accounting for contributions due to drifts, currents and anomalous heat transport, are given in [21, 66, 67].

3.3.2 *EIRENE equations*

General aspects about the treatment of neutral species in edge plasma simulation have been introduced in sections 2.4.1 and 2.4.4. We have said that, although B2.5 standalone runs can be performed as described in section 3.3.1, usually the application of a kinetic treatment for these species gives much better results. In this section, we will address the the general ideas behind the solution of the Boltzmann transport problem by Monte Carlo methods. It is well known that the advantage of Monte Carlo methods is mainly related to their ability to handle complicated geometries and make a detailed description of the system at a kinetic level. Conversely, the main drawback of this method is that the computational time is large due to the necessity of performing a large number of repeated *Monte Carlo histories* to reduce statistical noise. The

theory of Monte Carlo methods and the possibility to be used to solve transport theory problems is well-known, not only in relation to plasma physics [26].

We have seen in section 2.4.1 that the equation which describes the evolution of the distribution function $f_a(\mathbf{x}, \mathbf{v}, t)$ is the Boltzmann kinetic equation (25). If, moreover, we consider the collision event as a discontinuous process we can write Boltzmann collision operator (33), as the sum of a *pre* and *post-collision integral*

$$\begin{aligned}\frac{\partial f_a(\mathbf{x}, \mathbf{v}, t)}{\partial t} + \mathbf{v} \cdot \nabla_{\mathbf{x}} f_a(\mathbf{x}, \mathbf{v}, t) = \\ \int \sigma(\mathbf{v}', \mathbf{V}'; \mathbf{v}, \mathbf{V}) |\mathbf{v}' - \mathbf{V}'| f_a(\mathbf{v}') f_b(\mathbf{V}') d\mathbf{v}' d\mathbf{V}' d\mathbf{V} - \\ \int \sigma(\mathbf{v}, \mathbf{V}; \mathbf{v}', \mathbf{V}') |\mathbf{v} - \mathbf{V}| f_a(\mathbf{v}) f_b(\mathbf{V}) d\mathbf{v}' d\mathbf{V}' d\mathbf{V}\end{aligned} \tag{77}$$

where $f_a(\mathbf{x}, \mathbf{v}, t)$ is the distribution function for the test particle and $f_b(\mathbf{X}, \mathbf{V}, t)$ for the background, σ is the cross section for binary collisions and its first two arguments correspond to the velocity of the test particle and the background prior to the collision, which are turned into the post collision velocities. In this sense the first integral describes transitions $(\mathbf{v}', \mathbf{V}' \to \mathbf{v}, \mathbf{V})$ into the velocity space interval $[\mathbf{v}, \mathbf{v}+d\mathbf{v}]$ for species a, and the second integral describes the loss from that interval for this species. In equation (77), collisions are assumed as point events and the motion between collisions is assumed to be free. Moreover, to solve the linear transport problem for the species a, the background distribution function f_b is assumed to be known. Equation (77) is usually rewritten in the form [78]

$$\begin{aligned}\frac{\partial f_a(\mathbf{x}, \mathbf{v}, t)}{\partial t} + \mathbf{v} \cdot \nabla_{\mathbf{x}} f_a(\mathbf{x}, \mathbf{v}, t) + \Sigma_{t,a}(\mathbf{x}, \mathbf{v}) |\mathbf{v}| f_a(\mathbf{x}, \mathbf{v}, t) = \\ \int C(\mathbf{x}, (\mathbf{v}', a'; \mathbf{v}, a)) |\mathbf{v}' - \mathbf{V}'| f_a(\mathbf{v}') d\mathbf{v}' + Q(\mathbf{x}, \mathbf{v}, t)\end{aligned} \tag{78}$$

where $\Sigma_{t,a}(\mathbf{x}, \mathbf{v})$ is the total *macroscopic cross section*, $C(\mathbf{x}, (\mathbf{v}', a'; \mathbf{v}, a))$ is the kernel of the collision operator and $Q(\mathbf{x}, \mathbf{v}, t)$ is the primary source. The macroscopic cross section is

$$\Sigma_{t,a} = \frac{1}{\lambda_{t,a}} = \frac{|\mathbf{v}|}{\nu_{t,a}} \tag{79}$$

here, $\lambda_{t,a}$ is the *mean free path* and $\nu_{t,a}$ is the *collision frequency*, i. e. the number of collisions which the test particle experiences during a unit time interval, which is given by

$$\nu_{t,a} = \sum_k \nu_{k,a} \quad \text{and} \quad \nu_{k,a} = \int \sigma_k(\mathbf{v}, \mathbf{V}, a; \mathbf{v}', \mathbf{V}', a')) |\mathbf{v} - \mathbf{V}| f_b(\mathbf{V}) d\mathbf{v} d\mathbf{V} d\mathbf{V}'$$

(80)

and the indices k represents the different collision processes that a given species a can do. The *collision kernel* $C(\mathbf{x}, (\mathbf{v}', a'; \mathbf{v}, a))$ is given by

$$C(\mathbf{x}, (\mathbf{v}', a'; \mathbf{v}, a)) = \sum_k \nu_{k,a'}(\mathbf{x}, \mathbf{v}) c_k(\mathbf{x}, (\mathbf{v}', a'; \mathbf{v}, a)) \tag{81}$$

where the factor $c_k(\mathbf{x}, (\mathbf{v}', a'; \mathbf{v}, a))$ is the conditional probability distribution for the post-collision species a with velocity $\mathbf{v}$ and for the specific collision process k.
The simplest Monte Carlo approach of solving the equation (78) derives straight from physical meaning of the transport equation. Indeed, this equation describes the evolution of the distribution function of the particles produced by the source $Q(\mathbf{x}, \mathbf{v}, t)$. They travel along straight lines and undergo collisions with background particles or with the domain wall, with frequencies $\nu_{k,a}(\mathbf{x}, \mathbf{v})$. In each collision the particle changes its velocity and type according to the distribution $c_k(\mathbf{x}, (\mathbf{v}', a'; \mathbf{v}, a))$. The process continues until the test particle is absorbed. Monte Carlo methods solve equation (78) by reproducing this process in a computer for a finite number of trajectories, using machine generated pseudo-random numbers. This is called *analog sampling*.
The design of a typical Monte Carlo transport code can be considered as consisting of two principal parts [78]: the *geometry module* and the *physical module*. The geometry module performs the particle tracking and it is to a large extent independent of the particular problem to be solved, and it can be applied to many transport phenomena, such as neutron transport or radiation transport. The physics of the problem, instead, is a *problem-specific* part of the code and it is defined by the source $Q(\mathbf{x}, \mathbf{v}, t)$, the post-collision distribution $c_k(\mathbf{x}, (\mathbf{v}', a'; \mathbf{v}, a))$ and the collision rates $\nu_{t,a}(\mathbf{x}, \mathbf{v})$. For a more detailed description of this second specific part we refer to [18]. In section 3.3.3, anyway, we will add some more information about how the transport of different species is handled by EIRENE.

3.3.3 *EIRENE modeling of different species*

According to what we have said in section 1.2.1, in most of the applications related to nuclear fusion research the interest is related to the study and simulation of hydrogen plasmas. To be more precise, since we are interest in the exploitation D-T fusion reactions, but at present only few experimental campaign involving tritium have been performed, most of the theoretical and experimental research deals with a plasma mainly composed by deuterium. Even neglecting all the impurities that could be present into the plasma, anyway, many atomic and molecular species has to be considered to take into account the relevant atomic and molecular processes reported in table 1.

The basic constituents of a pure deuterium the plasma considered by EIRENE are D^+, D, D_2 and D_2^+. Among them, the code distinguishes (1) *background plasma ions* (D^+), whose transport is computed by B2.5, while EIRENE produces the source and sink terms S_n and $S_{i\|}^m$ for the balance equations (70), (71), (75) and (76); (2) *neutral atoms* and *molecule*, like D and D_2, whose transport equation is solved by EIRENE, as described in section 3.3.2; (3) other kinds of ions, mainly with molecular structure such as D_2^+, that are referred to as *test ions*[1]. These kind of ions, represents a small fraction of the overall plasma density and moreover, their molecular nature is not compatible with the solution of their transport equation by B2.5. Still, their presence can be important for the overall particle, momentum and energy balances and atomic and molecular collision processes involving these particles have to be considered.

The transport of test ions in the plasma is computed by EIRENE in the routine `FOLION`. In principle, this is not an easy task, since as we have seen in section 2.4.1, the kinetic treatment of charged particle transport in an electromagnetic field requires the solution of the full Boltzmann equation (25), where the motion between collisions is not free, as it is for neutrals in equation (78), but it is affected by the Lorentz force. Anyway, for typical plasma densities reached in the SOL, of the order of $\sim 10^{20}\,\mathrm{m}^{-3}$, test ion mean free path is much smaller that the numerical space resolution defined by the computational grid size [40], and the problem of dealing with test ions transport can be greatly simplified. Indeed, in this case, instead of being traced, test ions are treated by EIRENE in the co-called *static approximation*: their trajectories are not followed and the test particle is destroyed immediately at its point of birth by a collision. In Monte Carlo language a collision estimator is used instead of a track-length estimator [18].
As will be discussed in details in section 5.3.2, the soundness of the static approximation for test ions, which is by default implemented in EIRENE, is largely influenced by the values of the background plasma density. Only for sufficiently high plasma densities, in fact, the collision frequency of D_2^+ molecules is high enough to neglect their transport around the plasma. As we will see, this conditions can be questioned when medium-flux devices, such as the GyM plasma machine simulated in this thesis work, are consider.

1 Beside D_2^+, when more complex plasmas are described, considering e. g. sputtering of carbon atoms from the wall is considered, also $CH_3{}^+$ is considered among test ions.

3.4 AUG EXEMPLE RUNS

In this section, to conclude the general overview on the SOLPS-ITER code, we want to present the results obtain by running the example input files contained into the `runs/examples/` folder. In particular, we present the *AUG_16151_D* example, which considers the *standard single-fluid 5.0 benchmark case*. This simulation corresponds to the Asdex Upgrade (AUG) shot #1615 configuration, with *low single null* (LSN) magnetic configuration. The two meshes for the standalone and coupled case are reported in figure 13. Only deuterium species are present in the plasma and any kinds of impurities are neglected in this benchmark. Total power incoming from the core plasma equal to $P_{core} = 1.6\,\mathrm{MW}$ is imposed at the *SOUTH* core boundary. Usual sheath boundary conditions are imposed at the *EAST* and *WEST* target boundaries, while at the *NORTH* boundary exponentially decreasing plasma profiles are set, with decay length $\Lambda = 0.01\,\mathrm{m}$.

In figures 18a and 18b, the norms of the residues respectively for the B2.5 standalone and the couple B2.5-Eirene case are shown. As one can see, the standalone case has converged to machine accuracy, while the residues for the coupled simulation are strongly affected by Monte Carlo statistical noise. In this case, the attainment of a converged stationary solution is not inferred by the value of the residues, which in any case have to be stable around stationary levels, but by the particles and energy balance, that can be checked by means of the *run diagnostic scripts* `particle_balance.py` and `energy_balance`.
To assess the statistical Monte Carlo error and to reduce the norms of the residues, averaging solution procedures have been recently developed [4]. In this context, one distinguishes between *instantaneous plasma solutions* and *iteration averaged solutions*: the latter are obtained by averaging the instantaneous solution obtained at each code time-step over many subsequent iterations. Studies [30] revealed that the statistical error of iteration averaged solutions decreases inverse proportional to the amount of iterations N over which is averaged, $\epsilon_s \propto 1/\sqrt{N}$. Similarly, the error also decreases with increasing number of Monte Carlo particles P, launched at each iteration, $\epsilon_s \propto 1/\sqrt{P}$. In the case presented here, the averaging procedure, as it is clear from figure 18b, has not been adopted.

Comparison between the standalone and coupled simulation results for the electron density and temperature are shown in figures 19 and 20, where the 2D patch-plot of the plasma quantities is shown on the fluid physical mesh. From the first figure, we that the main differences observed in the plasma density are located near the target plates, where the effect of the atomic and molecular processes and plasma recycling is more intense. A higher plasma density is observed in the target region, when the simulation is performed in coupled

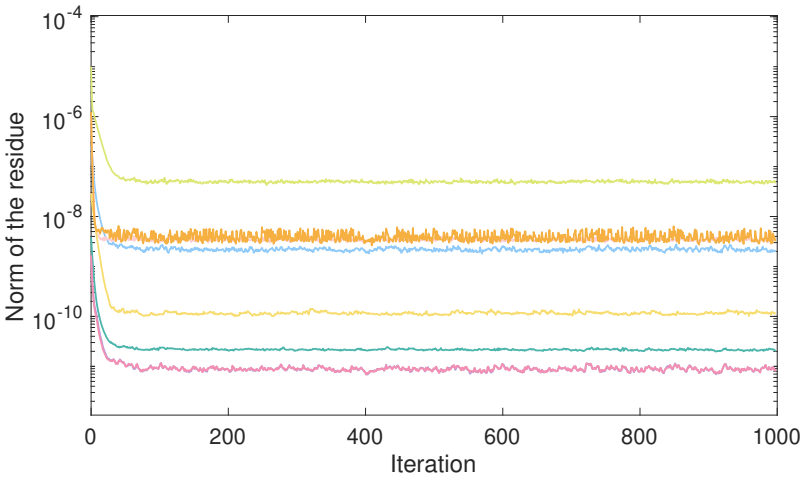

(a) *Norm of the residue, standalone simulation.*

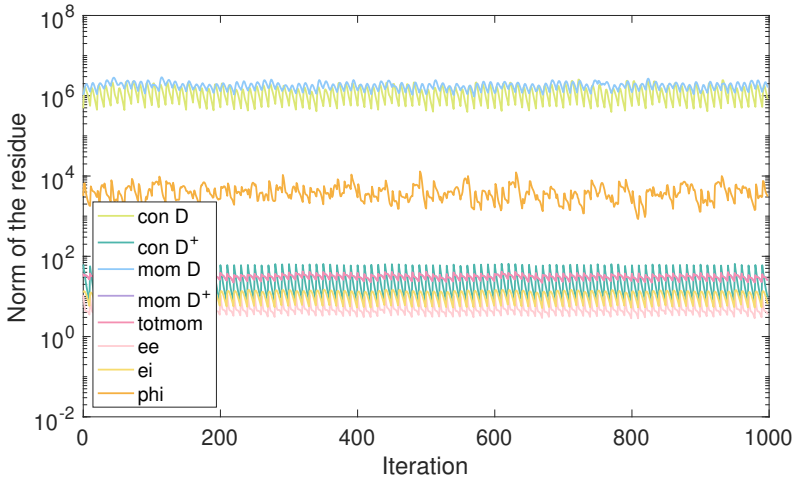

(b) *Norm of the residue, coupled simulation.*

Figure 18: Converged behaviour of the norm of the residue for standard test simulation. In particular figures 18a and 18b refer to the AUG_16151_D example.

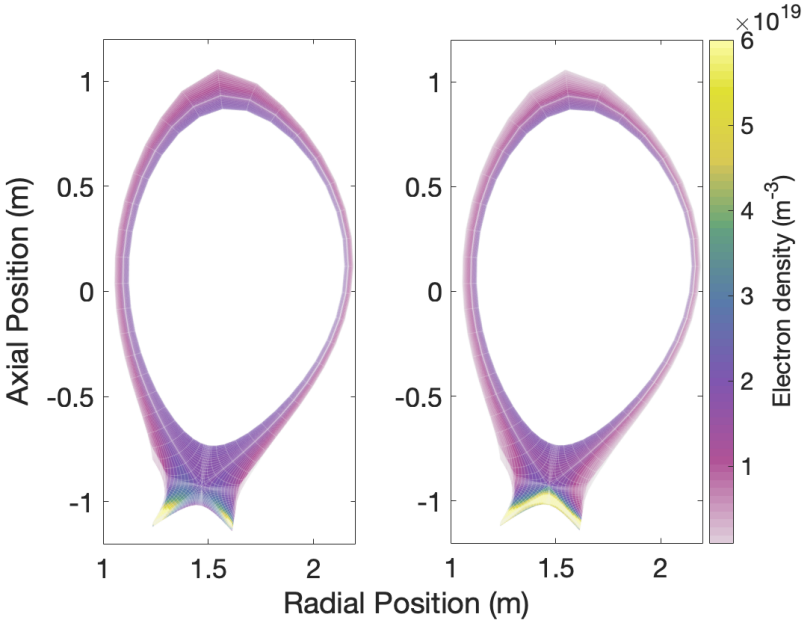

Figure 19: 2D patch plot on the physical mesh for the electron density (m^{-3}). The result for the standalone simulation is on the left and the coupled one on the right.

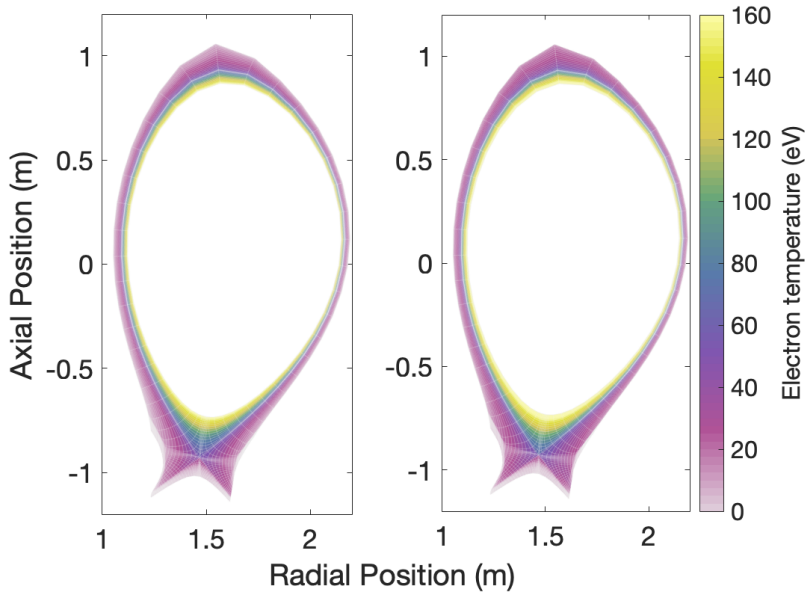

Figure 20: 2D patch plot on the physical mesh for the electron electron temperature (eV). The result for the standalone simulation is on the left and the coupled one on the right.

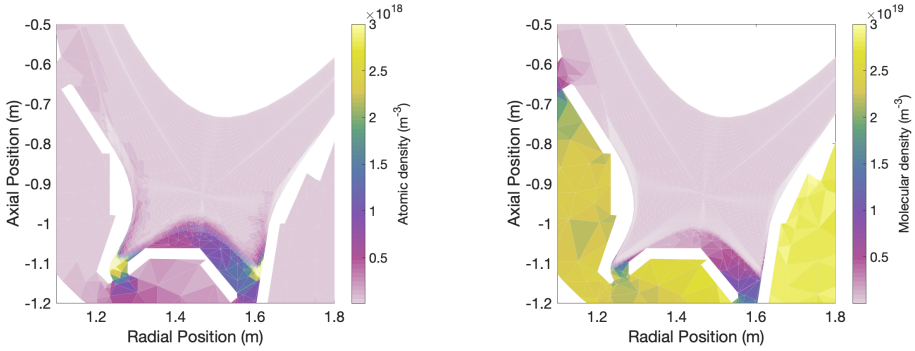

(a) *Density of neutral atomic deuterium D* (m^{-3}) (b) *Density of neutral molecular deuterium* D_2 (m^{-3})

Figure 21: Density of atomic neutral species D (m^{-3}). Different color-bar scales have been used since the molecular content is dominant over the atomic one.

mode.

Considering the second figure, as can be expected, the electron temperature is higher at the *SOUTH* core boundary where the 1.6 MW input power is imposed. This is typical of tokamak simulations, where the plasma energy is transferred into the SOL by heat diffusion from the central core region.

Concerning the neutral species present in the plasma, we have reported in figure 21, the density of atomic D and molecular D_2 species in the target region. In this case, the 2D patch-plot is shown on the extended triangular grid, which extends outside the plasma boundary, up to the chamber wall. As one can see, in typical tokamak scenario, neutral content inside the plasma is very limited, and the SOL region is mainly composed by ionized particles. Atomic processes, on the contrary, are important in the region of the targets, where neutrals are produced by the recycling process. In the region outside the plasma domain, molecular species are much more abundant, since gaseous deuterium is essentially D_2. Atomic D is almost only present near the targets, as consequence of neutral ionization processes.

4

MODELING OF GYM LINEAR PLASMA DEVICE

In this section, GyM linear plasma device is described. Emphasis will be given to general aspects related to the modeling of the machine. In particular, it will be discussed how to correctly simulate its features with SOLPS-ITER. When dealing with linear machines the graphical user interface `DivGeo` can not be used as starting point to construct the main input for the code. Thus, meshes and other input files have to be constructed by the user developing dedicated programs.
In section 4.1, a general introduction to the machine is given, describing the most relevant dimensions and the coil structure. In section 4.2.1, the procedure used to compute the magnetic field is discussed. The magnetic field and in particular the flux function ψ, is then needed to construct the mesh aligned with me magnetic field lines. In section 4.2.2 and section 4.2.3 the procedure adopted to generate the mesh for B2.5 and EIRENE is described. Beside magnetic field, the other critical aspect is the modeling of the plasma source, which will be addressed in section 4.3. Finally in section 4.4 other possible magnetic field configurations that can be exploited in GyM are presented.

4.1 GYM STRUCTURE

GyM (Gyrotron Machine) is a linear plasma device designed and built by *IFP (Istituto di Fisica del Plasma) - CNR (Centro Nazionale delle Ricerche)* in Milan. This machine was designed to study both elementary plasma physics phenomena, such as plasma heating and turbulence, and plasma-material interaction in the context of nuclear fusion research.
The structure of the machine is shown in figure 22 and the some of the more rel-

Dimension	**[cm]**
Cylindrical vacuum chamber length	205.8
Cylindrical vacuum chamber internal diameter	25.0
Total length, from coil 1 to coil 10	276.6
Coil external diameter	83.0
Coil internal diameter	55.2
Coil width	9.2

Table 3: Most relevant dimensions of GyM linear plasma device.

evant dimensions are reported in table 3. The axial magnetic field is produced by ten azimuthal coils which are placed around the vacuum vessel. Each coil is made of 36 copper windings and the current in each winding can be varied up to 1000 A. In figure 22, the positions of other important components of the machine are also shown: (i) the diagnostic system, represented by a Langmuir probe with which electron temperature, density and plasma potential can be measured as discussed in Appendix B; (ii) the pressure meter, to measure the neutral gas pressure inside the chamber; (iii) the two ducts, at the end of which there are the pumps to keep the system in high-vacuum conditions; (iv) the gas puffing system, to inject neutral gas into the chamber; (v) a 3 kW radio-frequency (RF) source to generate and heat up the plasma; (vi) the sample holder for fusion-relevant materials exposure.
The reference frame used in the following is the one shown in figure 22: the axial origin is aligned with coil number 6, while the radial origin is aligned with the axis of the cylinder.

4.2 MAGNETIC FIELD

The standard magnetic field configuration used in GyM is produced by flowing currents in the ten azimuthal coils connected in series. The axial modulation of the magnetic field is obtained from non uniform axial separation of the coils. From figure 22, in fact, one can see that coils number 3 and 4 are closer than the others, producing a more intense magnetic field near the left base of the cylinder. This is evident from figure 23, where the axial variation of the magnetic field is shown at different radial positions and for a fixed current of 600 A. Clearly, by increasing the current, the magnetic field increases accordingly. For this reason, it is usual to refer to the magnetic field configuration by means of the corresponding current value in Ampere. In the following we will refer to the magnetic configuration obtained for 600 A current by simply saying *the magnetic field at* 600 A.
A 2D mapping of the value of the magnetic field in each point of the (Z,R) plane is necessary to construct the computational plasma grid, which must have one dimension aligned along the magnetic field lines for the reasons discussed in section 3.2. To do so, the magnetic equilibrium configuration must be found by solving the *Grad-Shafranov equation* [71].

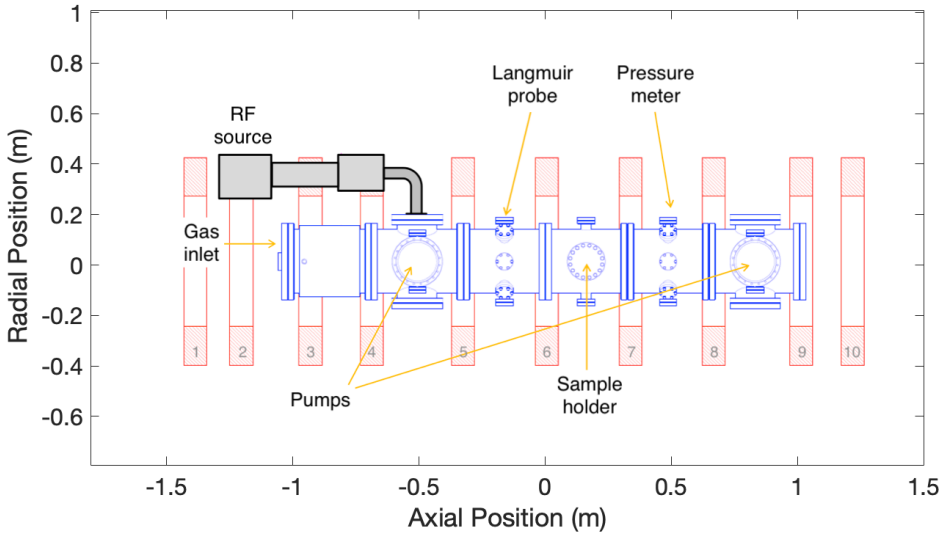

Figure 22: GyM (Gyrotron Machine) structure. RF source, gas puffing and pumping systems, plasma diagnostic, pressure meter, and the sample holder positions are also shown.

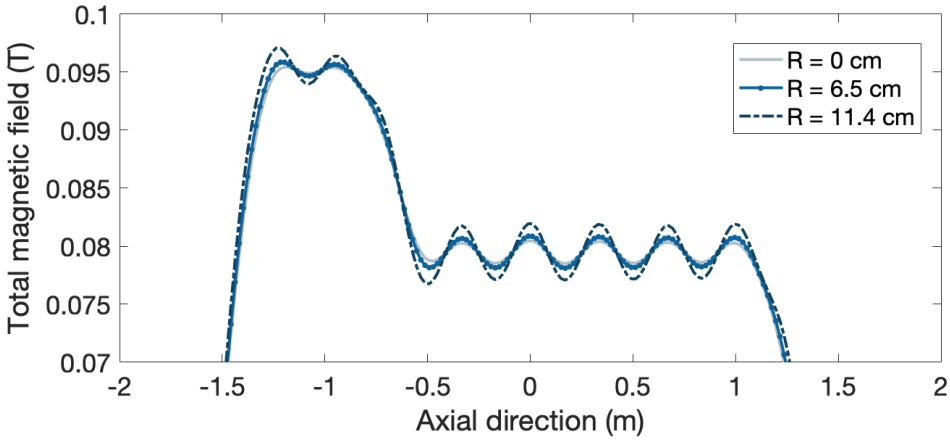

Figure 23: Magnetic field at 600 A as a function of the axial position on the axis ($r = 0\,\text{cm}$), around half the radius of the chamber ($r = 6.53\,\text{cm}$) and near the lateral wall of the chamber ($r = 11.43\,\text{cm}$).

4.2.1 *Grad-Shafranov equation*

In section 2.1.1, we have discussed that, although magnetically confined plasmas are rigorously non-equilibrium systems, an equilibrium configuration is necessary for many aspects of plasma modeling. Thus, plasma equilibrium can be obtained under the hypothesis of ideal MHD by solving the system of equations (15). When dealing with axial symmetric configurations, such as tokamaks and linear devices, this system of equations is usually rewritten using cylindrical coordinates (R, Z, ϕ). If one considers the $\nabla \cdot \mathbf{B} = 0$ and $\nabla \times \mathbf{B} = \mu_0 \mathbf{J}$ equations first, assuming toroidal symmetry $\partial/\partial\phi \simeq 0$, the following equation is obtained [28]:

$$\Delta^* \psi(Z, R) = -\mu_0 R J_\phi \tag{82}$$

where the scalar function ψ is the *magnetic flux function* and it is related to the vector potential $\mathbf{A}$, by the expression $\psi = RA_\phi$, or equivalently to the magnetic field by the expressions [28]:

$$B_R = -\frac{1}{R}\frac{\partial \psi}{\partial Z} \qquad B_Z = \frac{1}{R}\frac{\partial \psi}{\partial R} \tag{83}$$

Moreover, the flux function ψ is proportional to the so-called *poloidal magnetic flux*, i. e. the flux of the poloidal magnetic field $B_\theta = 1/R\, \nabla\psi \times \mathbf{e}_\phi$.
Considering then the ideal MHD momentum equation $\nabla p = \mathbf{J} \times \mathbf{B}$, the toroidal current density J_ϕ can be written as:

$$J_\phi = R p'(\psi) + \frac{F(\psi) F'(\psi)}{\mu_0 R} \tag{84}$$

where the two *figures of merit* $p(\psi)$ and $F(\psi)$ are related to the plasma pressure and to the poloidal current $I_\theta = 2\pi F(\psi)$ [28]. Substituting this expression for J_ϕ into equation (82), the so-called *Grad-Shafranov equation* is obtained. By solving this equation for $\psi(Z, R)$ and substituting its expression in equations (83), the two components of the magnetic field B_R and B_Z on the poloidal plane are obtained. This, anyway, is not straightforward, since $p(\psi)$ and $F(\psi)$ are not in general known. One commonly adopted technique to solve the Grad-Shafranov equation consists in arbitrary specifying the functional dependency on ψ of these two figures of merit. In this case, the solution is easily obtained by solving an ordinary second order differential equation for ψ.
A more involved strategy is required when a *free boundary equilibrium* is needed. In this case, the plasma position and shape have to be obtained in addition to $\mathbf{B}$ and ψ. Indeed, the ϕ-component of the current density in equation (82) is given by the sum of two contributions: the external known current density $J_{\phi,ext}$ and the unknown plasma current density $J_{\phi,pl}$. Moreover, not only the value of the plasma current density is unknown, but also the domain on witch it is defined, since the plasma extension is determined by the magnetic field

itself. Solution of this kind of problems requires dedicated methods, known as *free-boundary problem solvers* [38].

In case of linear devices, where the dominant contribution to $J_\phi(Z,R)$ is given by the external current density, many of the complexities just described can be overcome by simply neglecting the plasma contribution. The equation to be solved in this case is simply $\Delta^*\psi(Z,R) = -\mu_0 R J_{\phi,ext}(Z,R)$. Once the B_R and B_Z components of $\mathbf{B}$ are found by equations (83), these are enough to compute the total magnetic field strength, since the ϕ-component of the magnetic field in a linear plasma device can be considered null, $B_\phi \simeq 0$.
To solve Grad-Shafranov equation for GyM, the *Green function method* [38] has been used. $\psi(Z,R)$ has been computed solving the following integral

$$\psi(Z,R) = \int_{\Omega_{coil}} G(Z,R;\bar{Z},\bar{R}) J_{\phi,ext}(\bar{Z},\bar{R}) d\bar{\Omega}_{coil} \tag{85}$$

where $G(Z,R;\bar{Z},\bar{R})$ is the *free space Green's function*

$$G(Z,R;\bar{Z},\bar{R}) = \frac{\mu_0}{2\pi}\frac{\sqrt{R\bar{R}}}{k}\left[\left(2-k^2\right)K(k) - 2E(k)\right] \tag{86}$$

with $k^2 \equiv (4R\bar{R})/((R+\bar{R})^2+(Z-\bar{Z})^2)$ and K(k) and E(k) are elliptic integrals of the first and the second kind, respectively. Although much faster methods exist, this one was easily implemented in Matlab and it is sufficiently efficient for the simple geometry of GyM. The solution of the equation (85) for the considered geometry, is shown in figure 24. The total magnetic field strength and the ψ function are represented. The cylindrical vessel of GyM is also shown, while it was actually neglected during the computation.
Now that we know the magnetic equilibrium configuration, i. e. the values of $\mathbf{B}(Z,R)$ and $\psi(Z,R)$ in every point of the (Z,R) plane, the plasma computational mesh can be constructed.

4.2.2 *B2.5 mesh construction*

As we already said in section 3.2, the B2.5 physical mesh is a rectangular-cell mesh which represents the domain where the plasma transport equations are solved. This domain connects the two targets, which in the case of a linear device, are represented by the two bases of the cylinder, and can not intersects the side boundaries. The mesh cells are aligned following in one direction the magnetic field lines and in the other the radial cross-field coordinate. As already mentioned in the introduction to this chapter, the `DivGeo` graphical user interface can not be used to construct the mesh since the program treats only toroidal geometries. Therefore, an ad-hoc mesh generator needs to be built when dealing with linear devices. For this purpose, we developed a Matlab script. The B2.5 mesh for GyM at 600 A magnetic field is shown in figure 25.

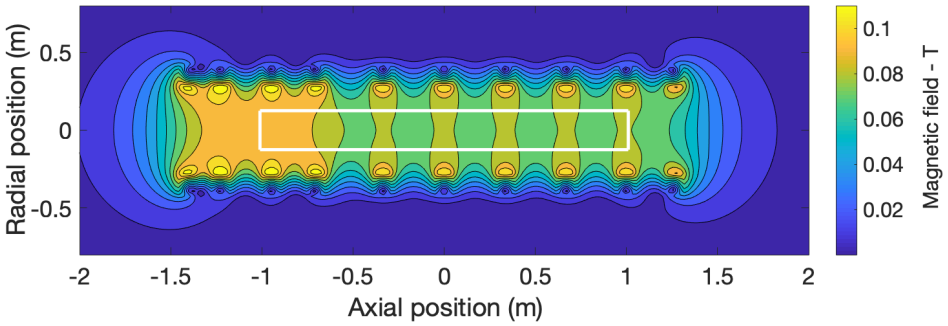

(a) *Modulus of the standard* 600 A *configuration of GyM magnetic field in* T.

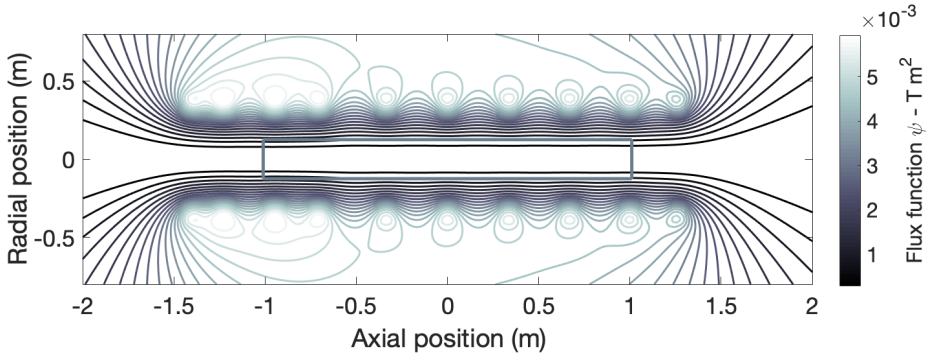

(b) ψ *flux function for the standard* 600 A *configuration of GyM magnetic field in* $\mathrm{T\,m^2}$.

Figure 24: Magnetic field and ψ flux function for the standard GyM field configuration at 600 A.

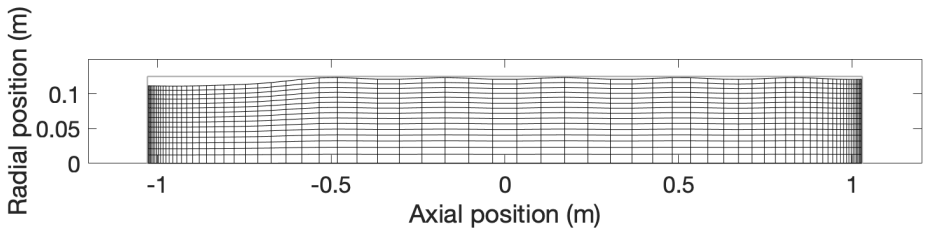

Figure 25: B2.5 mesh for GyM standard magnetic field structure for 600 A. The grey line represents the vacuum chamber cross-section in the (Z,R) plane. In this case $n_x = 75$ and $n_y = 15$.

As we can see, due to cylindrical symmetry, only half of the domain in (Z,R) plane is represented.
The scheme of the Matlab script is the following:

1. the ψ flux function is obtained by solving the Grad-Shafranov equation, as shown in section 4.2.1;

2. many *iso-*ψ lines are computed in the region of the (Z,R) plane inside the vacuum chamber;

3. of these lines, one, arbitrary closed to the maximum internal radius of the cylinder, is chosen as upper boundary for the plasma domain, checking that it never intersects the lateral wall, as shown in figure 26;

4. the domain is, then, divided into n_x cells in the axial direction by cutting the (Z,R) plane orthogonally to the cylinder axis, along the R-direction: as we can see, the dimension of the cells is not uniform along the Z-direction so that a more refine grid is obtained in the proximity of the targets, where the gradients are more significant;

5. to obtain the radial discretization of the domain, n_y cells are produced by tracing the *iso-*ψ lines from the outermost one to the axis of the cylinder. A more refined grid near the wall is considered;

6. finally, one more cell outside each boundary cell is added: these cells are called *guard cells*, they are much smaller than other cells, as it is shown in figure 26, and are used to set the boundary conditions.

Once the grid is ready, an `ASCII` file containing the R and Z positions of the cell vertexes and centers and the values of the axial and azimuthal components of the magnetic field at the cell center has to be written. This file is the input for the `b2ag` program togeter with the `b2ag.dat`, described in section 3.2. At

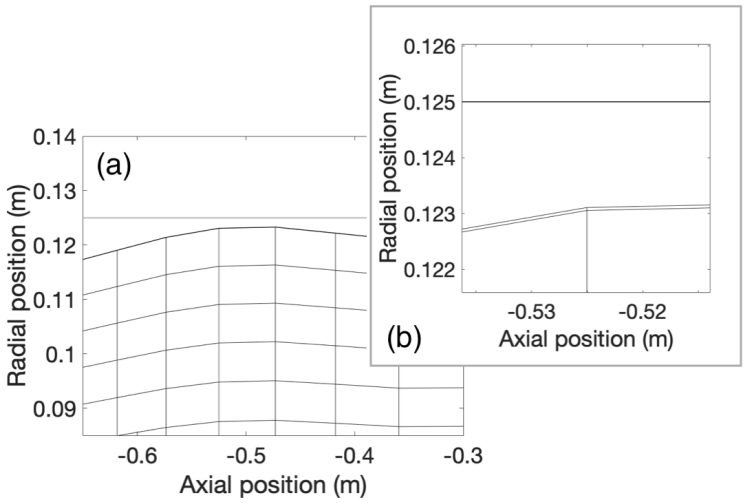

Figure 26: B2.5 mesh details: (a) the mesh can not intersect the lateral plasma boundary. (b) the guard cells are added in correspondence of north, west, wast and south boundaries to impose boundary conditions.

this point, some technical issues have been encountered regarding the right sorting of the mesh points in the `ASCII` file. These are due essentially to the fact that usual tokamak geometry is represented in the (R,Z) plane, while linear machines are more commonly represented in the (Z,R) plane. Although we are eventually able to provide to the code readable inputs for both orientation of the reference frame, the usual (R,Z) tokamak frame was chosen, in agreement with the existing literature on SOLPS application to linear machines. The simulation results were then analyzed by means of home-made Matlab post-processing tools to coming back to the (Z,R) frame. These tools are based on scripts provided by the code developers. Dedicated changes were made to use them for linear geometries.
The two outputs of the `b2ag` program containing all the information about the B2.5 geometry are the `b2fgmtry` and the `fort.30` and are used respectively by the B2.5 and EIRENE programs.

4.2.3 *EIRENE mesh construction*

The preparation of the triangular mesh for the coupled fluid-Monte Carlo version of the code also requires some special care in case linear geometry is considered. As we have said, this mesh, contrary to the B2.5 of section 4.2.2, extends over all the 2D cross section of the machine. Thus, a profile for GyM boundary must be provided, considering also segments and ducts other than the principal cylindrical chamber. The B2.5-EIRENE mesh used in our simu-

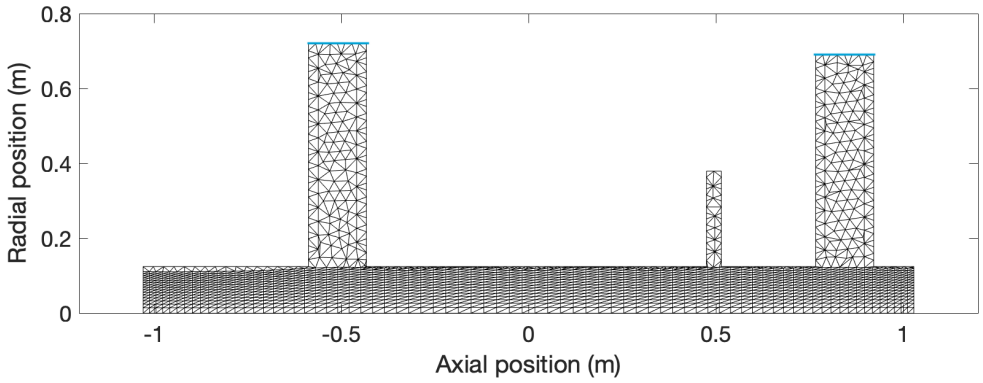

Figure 27: EIRENE mesh for GyM standard magnetic field at 600 A. The blue segments represent the pumping surfaces.

lations is shown in figure 27. Three additional ducts has been considered for GyM: the two ducts with larger diameter connect the principal chamber to the turbo-molecular pumps. Their top segments (colored in blue in figure 27) are open and gas can flow through them outside the domain; the smaller duct instead is closed and on ahead of it the pressure meter is located. The boundary segments were defined in `block 3B` of the `input.dat` file, where *additional surfaces* are defined (§3.2). Contrary to what happens for tokamaks, where these additional segments are defined by means of `DivGeo`, for linear machines they must be directly specified in the `input.dat`. Moreover, another surface has been defined in `block 3B`: a transparent segment placed near the west target, corresponding to the location of the gas nozzle, to simulate the effect of the gas-puff. For technical reasons in fact it is not possible to specify the puffing from a B2.5 grid segment. The possibility to define these kind of transparent segments on a surface laying inside the plasma domain, has been recently implemented for the SOLPS-ITER version of the code and it is important for the correct modeling of GyM device. The absence of this possibility in the previous SOLPS 5.1 version of the code has been one of the main reasons why the ITER version have been adopted to model GyM.
The files `fort.33`, `fort.34` and `fort.35`, containing respectively the coordinates of the nodes and vertices assignment for the triangles, and the connectivity information between triangles are created by the `triang` program. When the `DivGeo` interface is used, `triang` is automatically called, while for linear devices the program must be explicitly called, providing as inputs the `fort.30` file and the `triang.eir` files. The latter is the same as `input.dat` but with different *operating mode*, define in block 1.

4.3 THE RADIOFREQUENCY SOURCE

In sections 4.2.3 and 4.2.3, we have described how to prepare the `b2fgmtry` and `fort.33`, `fort.34` and `fort.35` files containing all the geometries information that the code requires. In this section, the same is done for the input file `b2.sources.profile`, related to the external particle, energy and momentum sources. Differently from tokamaks, where energy usually diffuses into the SOL from the core plasma, in linear devices the energy and plasma sources are often present into the simulated domain.
To understand how the `b2.sources.profile` for GyM is obtained (§4.3.2), first a general description of the *electron cyclotron resonance mechanism*, exploited as plasma source in GyM, is given (§4.3.1).

4.3.1 *Electron cyclotron resonance*

As we have seen in section 2.1.1, a charged particle in a magnetic field gyrates around the magnetic field lines, with frequency equal to the Larmor frequency, whose expression is given in equation (11). Moreover, when an electromagnetic wave is injected inside a magnetized plasma, many resonant phenomena can occur depending on the wave frequency, allowing a transfer of energy from the electromagnetic wave to the plasma [76]. In GyM, the so-called *electron cyclotron resonance* is exploited: efficient energy coupling between the wave and the electron population in the plasma occurs when the frequency of the electromagnetic wave ν_{RF} is equal to the electron Larmor frequency:

$$\nu_{RF} = \frac{eB}{2\pi m_e} \tag{87}$$

More precisely, in GyM a microwave source produces electromagnetic waves with frequency $\nu_{RF} = 2.45\,\mathrm{GHz}$. This electromagnetic field is injected into the chamber through an optical window, and the resonance condition is reached when the magnetic field takes the resonant value B_{res}

$$B_{res} = \frac{2\pi m_e \nu_{RF}}{e} = 0.0875\,\mathrm{T} \tag{88}$$

The position of the resonant magnetic field B_{res} on the (Z,R) plane is shown in figure 28, for different values of current. From this figure, one can see that the shape of the iso-B lines at B_{res} changes and different resonance configurations can be obtained: (1) from 575 A to 625 A, the resonance region is almost a straight line radially crossing all the chamber at a fixed axial position; (2) from 625 A to 675 A, periodic resonance structures appears near the lateral wall of the chamber; (3) for higher current values no resonance occurs, since the resonant field value is reached outside the chamber. It follows that the operational windows of GyM is narrow and can be expanded only up to 2/3

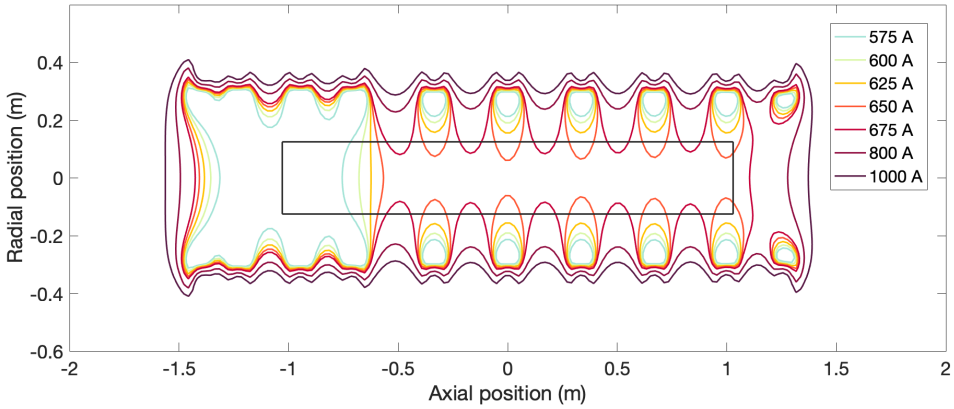

Figure 28: Electron cyclotron resonances for different magnetic field values.

than the maximum field strength $B_{max} = 1000\,\mathrm{A}$ which can be obtained with present current generator. In section 4.4 other possible current configurations are presented, which can partially overcome these limitations.

The electron cyclotron resonance, is actually just one of the possible resonant mechanisms to heat a magnetized plasma. More precisely, it can be shown that the resonance frequencies depend on the relative direction between magnetic field $\mathbf{B}$ and wave vector $\mathbf{k}$ [76]. If we consider the case in which $\mathbf{B}$ and $\mathbf{k}$ are parallel, then we find that the possible resonance frequencies are the electron and ion cyclotron frequencies and the plasma frequency. The plasma frequency $\omega_p = \sqrt{n_e e^2/\epsilon_0 m_e}$ is the most fundamental time-scale for plasmas and represents the typical electrostatic oscillation frequency in response to a small charge separation. Conversely, when the magnetic field $\mathbf{B}$ is orthogonal to the wave vector $\mathbf{k}$, the *upper-hybrid* and *lower-hybrid* resonant frequencies arise. The term hybrid refers to the fact that the associated resonant frequency is a mix of cyclotron and plasma frequencies, namely [68]

$$\omega_{UH} = \sqrt{\omega_p^2 + \omega_{L,e}^2} \tag{89}$$

$$\omega_{LH} = \sqrt{\frac{\omega_p^2 + \omega_{L,i}^2}{1 + \omega_p^2/\omega_{L,e}^2}} \tag{90}$$

Here, the general relation between ω and ν holds, namely $\omega = 2\pi\nu$. It is worth noting that, the dependency of ω_{UH} and ω_{LH} on the plasma frequency requires the knowledge of the plasma density allover the domain to assess where these two mechanisms are active.
In section 4.3.2, the modeling strategy adopted to reproduce the electron cyclotron resonance effects in SOLSP is explained.

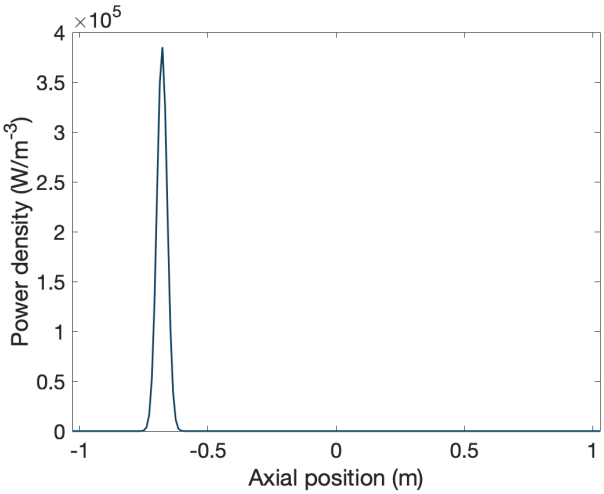

Figure 29: Axial profile of the electron heat source simulated in the code to model the electron cyclotron resonance heating. The total absorbed power is 800 W.

4.3.2 *Source modeling in SOLPS*

In section 4.3.1, some of the most important resonance mechanisms to transfer energy to magnetized plasmas by electromagnetic waves have been described. In particular, the electron cyclotron resonance exploited in GyM has been presented. In principle, the modeling of wave propagation and absorption in magnetized plasmas requires dedicated codes [25], since these mechanisms can not be directly simulated in SOLPS. Suitable assumption has then to be made in order to reproduce their effect on the plasma.
In this work the following two hypothesis have been made in order to implement Gym heating mechanism: (1) the only resonance mechanisms we consider is the electron cyclotron resonance. In this first attempt to model GyM energy source the existence of ω_{UH} and ω_{LH} is neglected due to their dependency to the unknown plasma density, as stated in section 4.3.1; (2) electron heating by ECH, is modeled as an external source term in the electron energy equation.
In the `b2.sources.profile` file the radial and axial profiles of the external energy sources can be specified, in terms of energy density. In our case, the source spatial modeling is based on the 2D contour plot of the iso-B lines for the resonant magnetic field, i. e. $\mathbf{B}(\mathbf{x}) = B_{res}$, shown in figure 28. From this figure, one sees that, for the field value $B = 600\,\mathrm{A}$, the spatial extension of resonance is localized around a narrow axial position, while it extends almost uniformly radially. In this thesis work, we have assumed that (a) the axial profile of the absorbed power density is represented by a narrow Gaussian, axially located in the region where the ECR occurs, as shown in figure 29. The standard deviation of the Gaussian profile is a free parameter in this modeling; (b) radially, the absorbed power density is constant, producing a total absorbed

power profile radially increasing as $\sim r$.
A weakness of our modeling is the absence of any information on the fraction of absorbed power with respect to the total RF source power. Experimentally, in fact, the only known parameter is the power carried by the electromagnetic wave, but no information on the actual power fraction that is absorbed by the plasma, is now available. Consequently, the power absorption efficiency η_a is treated as a free parameter in the simulations.

4.4 ALTERNATIVE MAGNETIC CONFIGURATIONS IN GYM

Finally, in this section we present two alternative magnetic field configurations for GyM. With the method discussed in section 4.2.1, the simplified Grad-Shafranov equation for linear devices has been solved, obtaining the magnetic field and the ψ poloidal flux function. The results are shown in figure 30. The main advantage that these magnetic field configurations offer is related to the possibility to have electron cyclotron resonance inside the main vacuum chamber at higher coil current values, thus allowing to expand the operational window of GyM.
From the experimental point of view, these configurations can be implemented, disconnecting two of the magnetic coils from the current generator:

- ◇ *Magnetic mirror configuration*: in this alternative configuration, the central coils 5 and 6 in figure 22 are disconnected, leading to an intense magnetic field at the boundary and lower at the center of the machine. The name magnetic mirror refers to the possibility, discussed in section, to have a configuration in which a positive magnetic field gradient near the extremes of the machine, enhancing the particle confinement in the axial direction.

- ◇ *Expanded magnetic configuration*: the second configuration is obtained by disconnecting two extreme coils, e. g. coils 9 and 10 in figure 22. In this way, an expansion of the magnetic field lines in correspondence of the East basis of the cylinder is observed.

The iso-B lines corresponding to the resonant magnetic field B_{res} are shown in figure 31, for different current values. As one can see, differently from the standard configuration where the maximum magnetic field to have ECR was around 675 A, in these configurations resonance in the plasma region is possible up to the maximum current value of 1000 A.

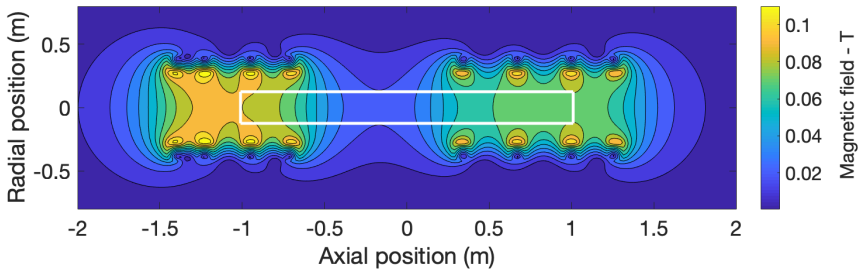

(a) *Modulus of GyM magnetic field in* T *for the magnetic mirror configuration at* 600 A.

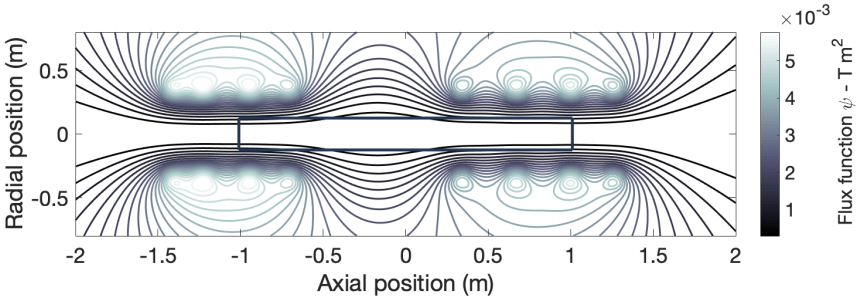

(b) ψ *flux function for the magnetic mirror configuration for* 600 A *of GyM magnetic field in* T m^2.

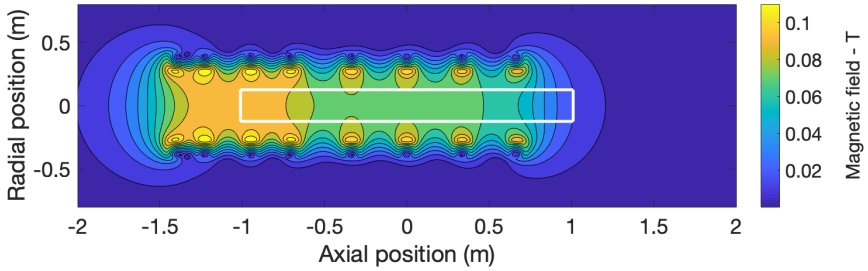

(c) *Modulus of GyM magnetic field in* T *for the expanded configuration at* 600 A.

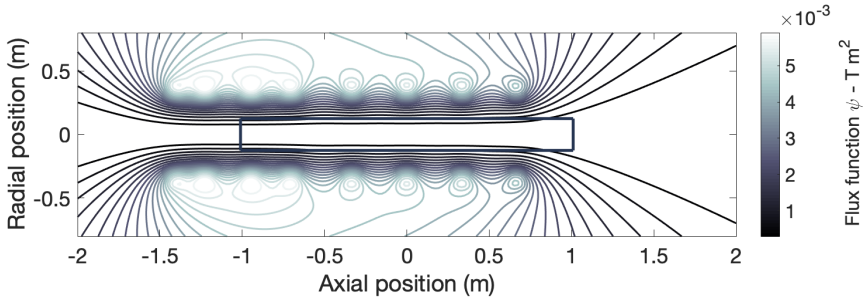

(d) ψ *flux function for the expanded configuration for* 600 A *of GyM magnetic field in* T m^2.

Figure 30: Magnetic field and ψ flux function for alternative current configurations in GyM. In particular, in figure 30a and 30b coils 5 and 6 are disconnected, while in figure 30c and 30d coils 9 and 10 are disconnected.

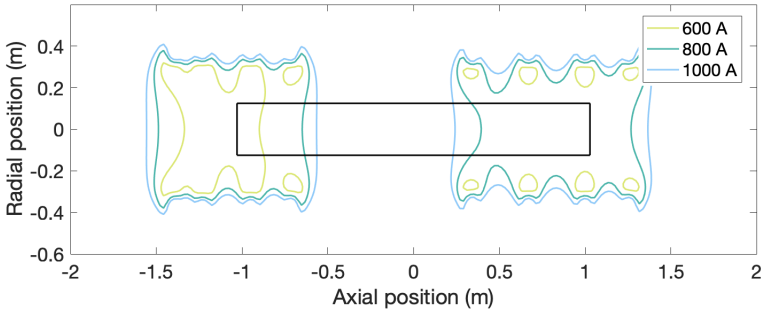

(a) *Mirror configuration.*

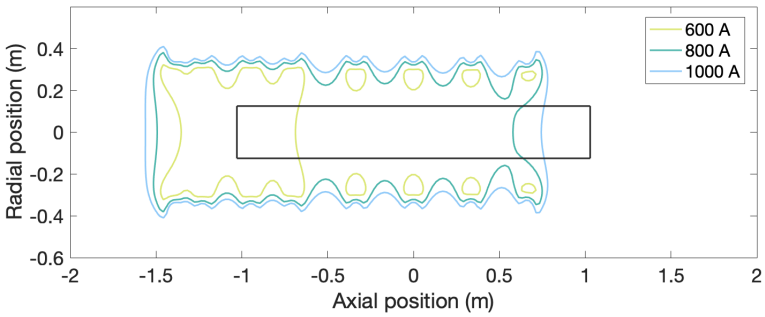

(b) *Expanded configuration.*

Figure 31: Resonant magnetic field $B = 0.0875\,\mathrm{T}$ for mirror and expanded configurations. We can see that ECR is inside the chamber for any value of currents, up to the maximum value of 1000 A.

5 SIMULATION RESULTS

This chapter is devoted to the presentation of the simulation results of GyM plasma modeling with SOLPS-ITER. Both standalone and coupled versions of the code were used, with the principal aim to investigate the effect of numerical and physical parameters on the simulation results. In the simulations we will present here, we considered a single plasma species in its first charge state, neglecting impurities from sputtering. Argon and deuterium plasmas were separately simulated, focusing mainly on the former. Moreover, a simplified physical model has been used, neglecting the contributions of drifts to the plasma equations. The ambipolar approximation has been instead relaxed and the current terms have been considered.
The first part of the chapter is devoted to the presentation of simulation results for argon plasmas, which were obtained using both the standalone and the coupled version of the code. The consideration of an argon plasma can be a good starting point for different reasons. First, since we consider only the first charge state, the number of atomic collision processes to be considered is reduced with respect to the deuterium case. Second, no molecules or molecular ion species are present. This reduces the number of species to be simulated with EIRENE and consequently a strong reduction of the computation time is observed. Results for the B2.5 standalone and B2.5-EIRENE coupled runs are presented respectively in sections 5.1 and 5.2.
In section 5.3, then, preliminary simulation results of B2.5-EIRENE coupled runs for a deuterium plasma are reported.

5.1 STANDALONE SIMULATIONS OF ARGON PLASMAS

The SOLPS code has been mainly used to simulate deuterium plasmas, both of tokamaks and linear devices. Here we will describe instead a plasma where the charged species is argon. Only the first charge state Ar^+ has been considered, since multiple ionizations can be neglected due to the low plasma temperature in GyM. As discussed in section 3.1, the multi-fluid nature of the code allows to include atomic species other than hydrogen isotopes as impurities. Impurities are usually simulated in order to understand their effects on nuclear fusion hydrogen isotopes plasmas. The possibility to simulate argon species, in particular, has been added to the SOLPS package in order to study the relieving effect this gas has on the heat fluxes impinging onto the first wall [82]. Thus, in principle the presence of this species has already been tested and applied. However, we found that the application of SOLPS-ITER to plasmas without

	Default value	Imposed value
'b2tnbf_xcur'	'0.0'	'0.0'
'b2tnbf_ycur'	'1.0'	'0.0'
'b2tlh0_flux_limit_style'	'2.0'	'0.0'
'b2tfnb_alpha'	'1.0'	'0.1'
'b2tlh0_alpha'	'1.0'	'0.1'

Table 4: Switches that has been modified from the default value, in order to run standalone simulation of an Ar plasma in GyM. To have a more specific description of the script functions we refer to [21].

hydrogen or its isotopes requires to set some switch parameters to non default values. In particular, the switches `'b2tnbf_xcur'` and `'b2tnbf_ycur'`, which define the value of the multiplier to the ion viscosities and inertial and anomalous currents in the poloidal and radial direction, have to be set to 0 (see table 4).

To approach the problem, we first performed standalone simulations, treating both Ar^+ and Ar as fluids, and neglecting pumping and puffing of neutral gas. This simplified situation is quite commonly adopted when test-case simulations has to be performed, e. g. see the AUG example presented in section 3.4. The use of this very simplified model, anyhow, implies that the evolution of the system is strongly affected by the imposed initial condition. Indeed, the total number of neutral and charged particles in the system is arbitrary fixed at the beginning of the simulation and, since no pumping or puffing exist, can not evolve in time. For this reason, this approach has been used to understand the numerical behaviour of the code, more that the evolution of the physical system. In particular, it has been used to understand issues related to the convergence of the code, make comparisons with previous version of the SOLPS, namely SOLPS 5.1, and study the role of space and time discretization.

5.1.1 *Convergence issues*

In this section we want to present the difficulties encountered to obtain convergence of the solutions of the B2.5 standalone case. It has been found that both inputs used to simulate GyM with the previous SOLPS 5.1 version [48] and SOLPS-ITER, provided in the `runs/examples/` folder, do not provide a converged solution.
The following attempts have been done to reach convergence of the code[1]:

1 In the following bullet points, some technical aspects of the code are mentioned. A reader that is not familiar with the code can skip this part without losing any important information.

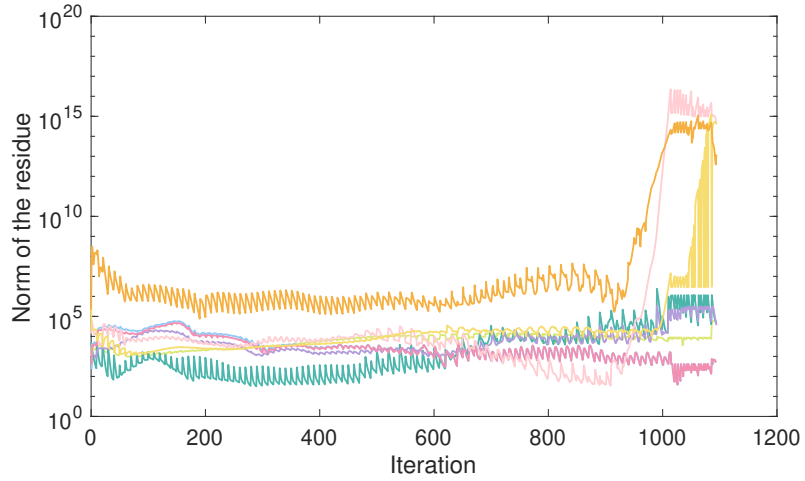

(a) *First not-converging result.*

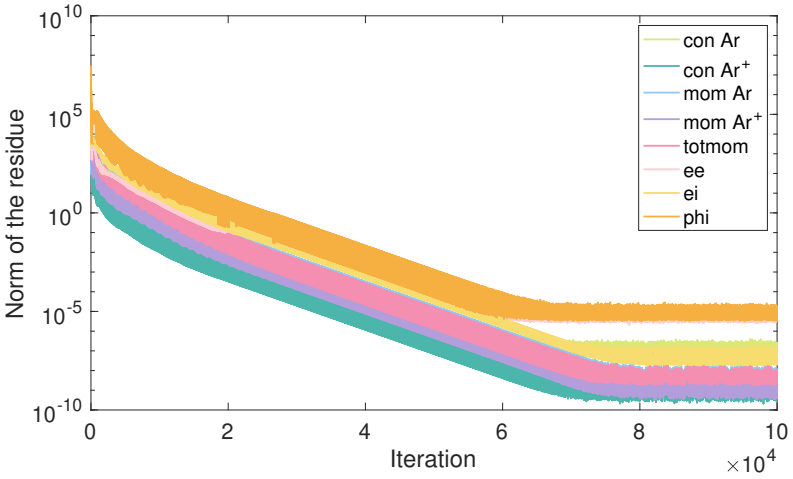

(b) *Converged result.*

Figure 32: Norm of the residue for GyM standalone Ar test-case.

- We started by running SOLPS-ITER code with input files of SOLPS 5.1 used in [48] to describe the same simplified physical situation of GyM on the new version of the code. Unfortunately, it was not possible to complete the simulation since, as we can see from figure 32a, many residues, in particular the one for the potential equation, rapidly increase after less than 1000 iterations. Although this diverging effect was not expected, it can be explained by the fact that the default set of switches in the `b2mn.dat` file for SOLPS-ITER code actually leads to a mixed treatment of the physical description of the 5.0/5.1 and 5.2/ITER versions[2] [21].

- In the `runs/examples/` folder there is a `b2mn.dat` input file, which contains all the switches added in SOLPS-ITER, not available in the previous versions of the code. Setting these switches to different values enables in principle to reproduce the behaviour of previous versions of the code. We have used both the `b2mn.dat_5.0`, to reproduce the SOLPS 5.1 behaviour, and the `b2mn.dat_5.2`, but even in these cases SOLPS-ITER does not converge.

- The successful strategy was to start from the `b2mn.dat` input file of a converged SOLPS 5.1 case. To this file, then, we have added one by one the new switches, setting their value so that the "old SOLPS 5.0 treatment" is implemented in the code.

Eventually, it was found that the main responsible for the non-converging behavior of the solutions, shown in figure 32a, is the `'b2tlh0_flux_limit_style'` switch. It controls how the flux limits for the neutrals thermal conductivity are computed. In particular, the new default treatment for SOLPS-ITER, first implemented by the St. Petersburg group for the SOLPS 5.2 code, applies the flux limit directly to the transport coefficients and not to the flux expressions [21]. In enforcing this something is probably not optimized for linear geometries, since a good converging behaviour can be obtained only if the old description is used.
It is not surprising that the problem is related in some sense to the fluid approximation of the neutral species. Indeed, it was evident since first applications of the SOLPS 5.1 code to GyM, that kinetic corrections to the neutrals fluid treatment are important due to the low plasma density and consequently long neutral mean free path, typical of this medium-flux machine. Limits to neutral fluxes must then be applied, according to what we have discussed in section 2.4.3. Considering equation (62), the value of the limiting factor α has been fixed to $\alpha = 0.1$ for both particle and energy neutral fluxes. This is done by means of the `'b2tfnb_alpha'` and `'b2tlh0_alpha'` switches [21], as shown in table 4.

2 We remember, according to table 2, that SOLPS 5.0 and SOLPS 5.1 mount the same version of the fluid code, and the same is true for SOLPS 5.2 and SOLPS-ITER.

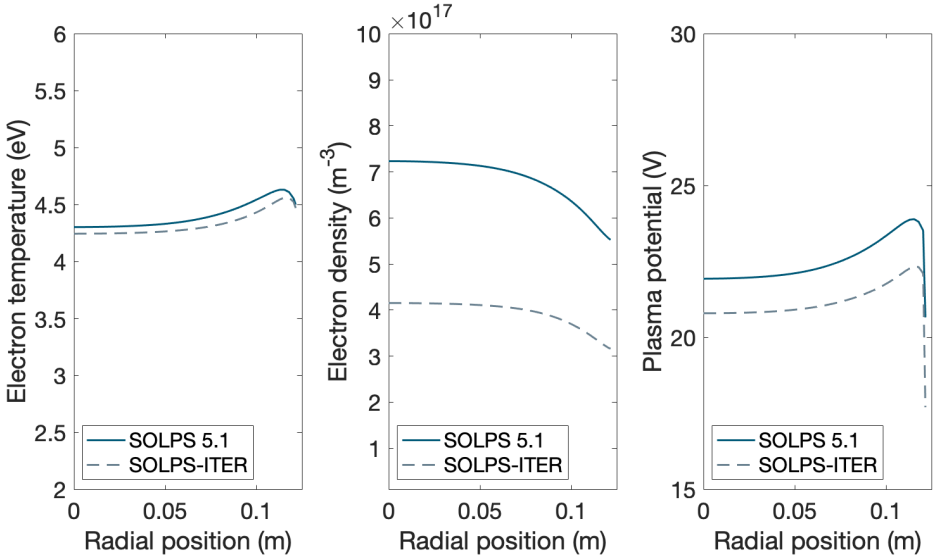

Figure 33: Comparison of electron temperature, density and plasma potential radial profiles simulated with SOLPS 5.1 and SOLPS-ITER.

The residuals behaviour introducing the new switches values for the neutral flux limits computation is shown in figure 32b. In this case, the maximum residual value is $\text{Res}_{max} \sim 1 \times 10^{-5}$.

5.1.2 *Comparison with SOLPS 5.1 simulations*

Having solved the convergence issues presented in section 5.1.1, we tried to compare the outputs of the two versions of the code SOLPS-ITER and SOLPS 5.1, starting from the same input files. The only difference in the two inputs is the presence of the `b2tlh0_flux_limit_style` switch in the SOLPS-ITER `b2mn.dat` to guarantee convergence. The other input parameters for the simulation are:

- **Initial conditions**: flat initial conditions are assumed both for electron and ion temperatures and plasma and neutral densities. The code allows to set separately only the density of the neutral species Ar and of each charged state, which in our case reduces to the first charge state Ar^+, while a homogeneous temperature can be set instead for both electrons and ions.

- **Boundary conditions**: at *EAST* and *WEST* boundaries, corresponding to the bases of the cylindrical chamber, *sheath boundary conditions* are imposed, as discussed in section 2.4.3; at the *SOUTH* boundary, cor-

Input parameter	**Value**
Magnetic field	$B = 600\,\mathrm{A}$
Initial densities	$n_{Ar} = 1 \times 10^{18}\,\mathrm{cm}^{-3}$ $n_{Ar^+} = 5 \times 10^{17}\,\mathrm{cm}^{-3}$
Initial temperatures	$T_e = T_i = 7\,\mathrm{eV}$
Total external power	$P_e = 1000\,\mathrm{W}$
Decay lengths	$\Lambda_{T_e} = \Lambda_{T_i} = \Lambda_n = \Lambda_\phi = 0.1\,\mathrm{m}$
Time step	$dt = 1 \times 10^{-5}\,\mathrm{s}$
Mesh size	$N_{iter} = 10000$

Table 5: Input parameters for the comparison of the outputs of SOLPS 5.1 and SOLPS-ITER and for the space-discretization analysis.

responding to the symmetry axis of the chamber, zero particle, momentum, energy and fluxes are set, together with zero plasma potential; at the *NORTH* boundary, exponentially decay profiles for the density, temperature and potential and zero parallel momentum flux are imposed. The corresponding *decay lengths* are indicated with Λ_n, Λ_{T_e}, Λ_{T_i} and Λ_ϕ.

- ◇ **External power absorbed**: the absorption of the total external power by the electrons of the plasma via electron cyclotron resonance heating is reproduced by an external source term in the electron temperature equation uses models described in section 4.3.2. The total external power is set to $P_{ext} = 1000\,\mathrm{W}$.

The same conditions apply to all the simulations discussed in the following. Specific values for each parameter will be specified for any simulations, and the ones considered here are reported in table 5. The B2.5 computational mesh is made of $n_x \times n_y = 200 \times 50$ cells, which is the same dimension originally used in SOLPS 5.1 simulations [48].
The results of the two simulations using SOLPS-ITER and SOLPS 5.1 are shown in figure 33. Here, the radial profiles for the electron temperature and density and plasma potential are displayed. They are taken ate the axial position corresponding to cell number $n_x = 100$.
Comparing the profiles of figure 33, one can see that the shape of the profiles is very similar in both cases. Quantitatively, differences in the electron temperature and plasma potential for the two versions are quite small, while a larger discrepancy of the plasma densities is evident.

5.1.3 *Effects of time discretization on the code performances*

The analysis presented in this section has the aim to investigate the effects of the dimension of the time step chosen on the simulation results. To do so, we performed four simulations, varying the time step to $dt = 1 \times 10^{-3}$ s, $dt = 1 \times 10^{-4}$ s, $dt = 1 \times 10^{-5}$ s and $dt = 1 \times 10^{-6}$ s but keeping constant the total simulated time. The total simulated time, indicated with $Time$, is given by the product of the time step at each iteration times the number of external iterations[3], $Time = dt \times N_{iter}$. In the simulations presented here, the simulated time is $Time = 0.1$ s, which is the same used in the comparison of the two SOLPS versions discussed in section 5.1.2. This means that the number of external iterations N_{iter} performed in the four simulations increases while the time step decreases, specifically from $N_{iter} = 100$ to $N_{iter} = 10000$.
The input parameters considered in this case are reported in table 6. As for simulation presented in section 5.1.2, the mesh used is the one used in SOLPS 5.1 simulations made of $n_x \times n_y = 200 \times 50$ cells. Results of the simulations are shown in figure 34. From this figure, one can infer that for $dt = 1 \times 10^{-5}$ s and $dt = 1 \times 10^{-6}$ s, a stationary solution is reached, since the profiles for the two cases are superimposed. These dt values are typical SOLPS time-step values [21]. For larger time-steps, instead, the solution does not reach convergence. This could also be seen from the evolution of the norms of the residuals (not shown here), which sufficiently small values, i. e. $Res_{max} \sim 1 \times 10^{-3}$ for $dt = 1 \times 10^{-5}$ s and $dt = 1 \times 10^{-6}$ s.

5.1.4 *Effects of space discretization on the code performances*

Finally, we performed an analysis of the effects of the grid size on the simulation results. The simulations presented in sections 5.1.2 and 5.1.3 have kept the same grid $n_x \times n_y = 200 \times 50$ originally used in the SOLPS 5.1 simulations. The dimensions of this grid have been chosen in agreement with available data regarding the simulation of the MPEX linear device with SOLPS 5.0 described in [63]. The cell size we have used here anyway is much smaller than the one usually adopted to model tokamaks, see e. g. the AUG grid used in section 3.4 and represented in figure 13. To understand if the grid resolution used is effectively too high, we performed three simulations reducing the number of cells in the grid: (a) $n_x \times n_y = 200 \times 50$, (b) $n_x \times n_y = 100 \times 25$ and (c) $n_x \times n_y = 75 \times 15$. For all three cases, the dimension of the cells in the axial and radial direction is not homogeneous and a more refined grid near the cylinder walls is considered, as discussed in section 4.2.2. The input parameter for the simulations are shown in table 5. Radial and axial profiles for electron temperature, density

3 In section 3.2, we had distinguished between internal iterations, which can be made within each and step to relax the equations solution and external iterations, which provide an increment of the time step.

Input parameter	**Value**
Magnetic field	$B = 600\,\mathrm{A}$
Initial densities	$n_{Ar} = 6.7 \times 10^{17}\,\mathrm{cm}^{-3}$ $n_{Ar^+} = 1 \times 10^{17}\,\mathrm{cm}^{-3}$
Initial temperatures	$T_e = T_i = 7\,\mathrm{eV}$
Total external power	$P_e = 1260\,\mathrm{W}$
Decay lengths	$\Lambda_{T_e} = \Lambda_{T_i} = \Lambda_n = \Lambda_\phi = 0.1\,\mathrm{m}$
$Totaltime = dt \times N_{iter}$	$Time = 0.1\,\mathrm{s}$

Table 6: Input parameters for the time-discretization analysis.

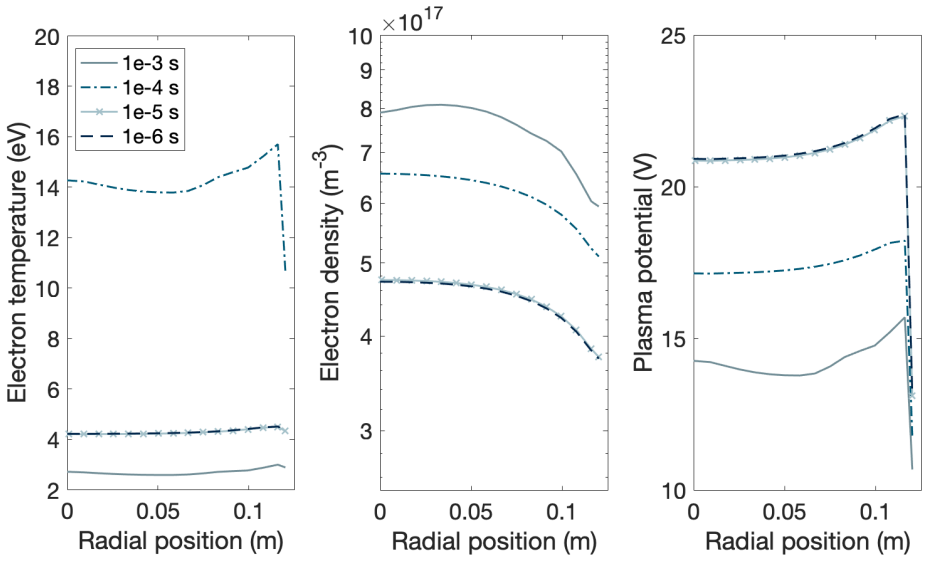

Figure 34: Comparison of radial profiles simulated with different time steps, dt but same simulated time. The four cases considered correspond respectively to (a) $dt = 1 \times 10^{-3}\,\mathrm{s}$ and $N_{iter} = 100$, (b) $dt = 1 \times 10^{-4}\,\mathrm{s}$ and $N_{iter} = 1000$, (c) $dt = 1 \times 10^{-5}\,\mathrm{s}$ and $N_{iter} = 10000$, (d) $dt = 1 \times 10^{-6}\,\mathrm{s}$ and $N_{iter} = 100000$.

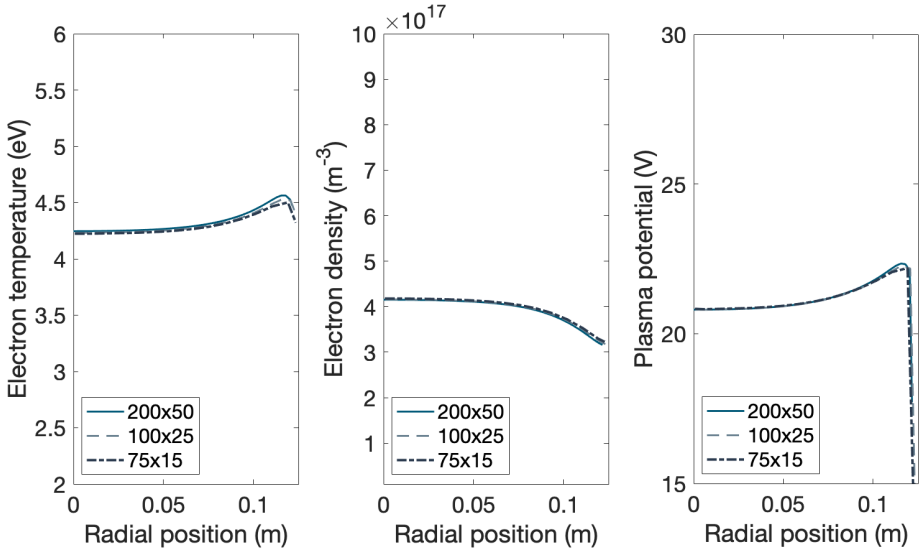

Figure 35: Comparison of radial profiles simulated with different grid sizes. The fhree cases considered correspond respectively to (a) $n_x \times n_y = 200 \times 50$, (b) $n_x \times n_y = 100 \times 25$ and (c) $n_x \times n_y = 75 \times 15$ meshes.

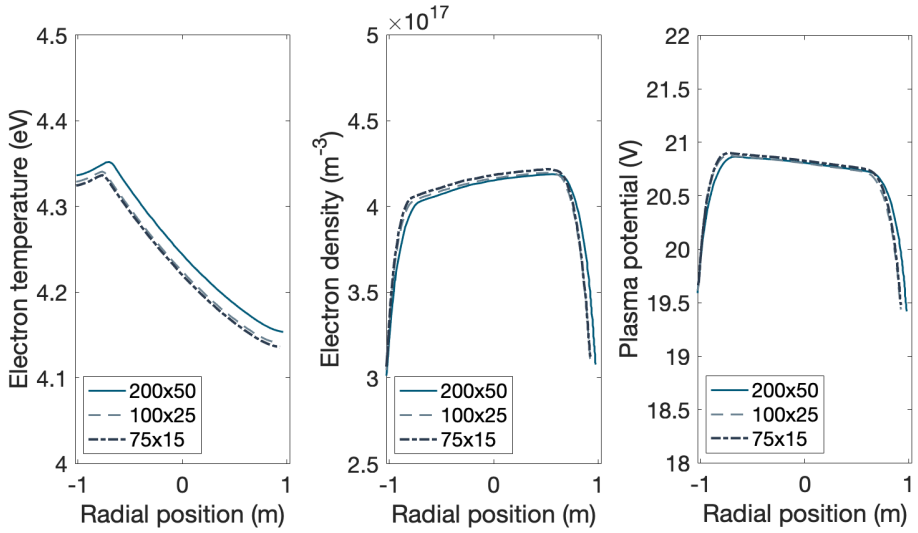

Figure 36: Comparison of axial profiles simulated with different grid sizes.

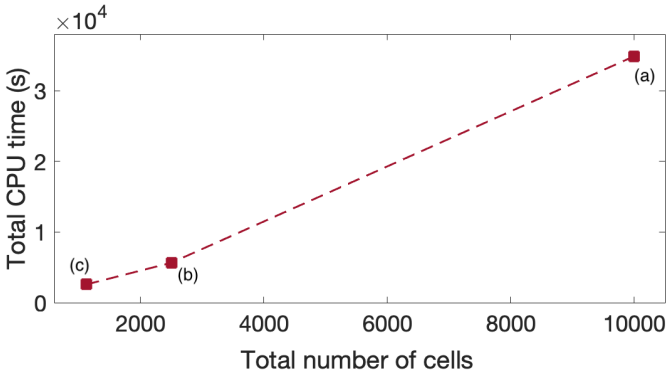

Figure 37: Total CPU time plotted against the total number of cells $n_x \times n_y$ in the mesh. The three red squares corresponds to (a) $n_x \times n_y = 200 \times 50$, (b) $n_x \times n_y = 100 \times 25$ and (c) $n_x \times n_y = 75 \times 15$.

and plasma potential are shown respectively in figures 35 and 36. From these figures, one can see that the effect of the grid discretization is essentially negligible for both radial and axial profiles of all the plasma quantities. What is not negligible, on the contrary, is the reduction in the computation time that can be obtained moving from a $n_x \times n_y = 200 \times 50$ to a $n_x \times n_y = 75 \times 15$ mesh. The total CPU time plotted against the total number of cells $n_x \times n_y$ is shown in figure 37. It is clear then that the benefits obtained by the reduction of the computation time largely overcome the small resolution gain with the $n_x \times n_y = 200 \times 50$ mesh. For this reason, in the following we will use the $n_x \times n_y = 75 \times 15$.

5.2 COUPLED SIMULATIONS OF ARGON PLASMAS

After the first B2.5 standalone simplified analysis, presented in section 5.1, in this section, we present the results obtained with the full B2.5-EIRENE coupled version of SOLPS-ITER. The performed simulations represent more physically relevant situations since the effects related to puffing and pumping of neutral species have been introduced. Before showing the results, we have to explain in more details how these two processes were modeled.
We will start considering the pumping process. In section 2.3.2, we introduced the recycling process of charged particles at the wall surface. This process is modeled in EIRENE defining a total recycling coefficient for each surface of the machine [18]. The `RECYCT` flag defined in the `block 6` of the `input.dat` file corresponds to the total probability of an incident particle to be re-emitted from the surface both as thermal or fast particle. This means that a flux `RECYCT` $\times\ Influx$ is re-emitted from a surface for any $Influx$ of particles of

any species directed toward the surface. `RECYCT` hence defines the sticking or absorption probability p_a of any surface

$$p_a = (1 - \texttt{RECYCT}) \tag{91}$$

meaning that, the fraction p_a of incident *atomic flux* is absorbed at the surface. The absorption probability p_a is also called *albedo* of the EIRENE surface and a $p_a \neq 1$ can be used to reproduce the effect of a pumping surface. Let $A\,(\mathrm{cm}^2)$ be the area of a surface seen by test particles, to which a given pumping speed $S\,(\mathrm{L\,s}^{-1})$ is to be assigned. Then the relationship between the experimental pumping speed for particles with temperature $T\,(\mathrm{K})$ and mass $m\,(\mathrm{u})$ and albedo $p_a = 1 - \texttt{RECYCT}$ is given by [18]

$$S = A \cdot (1 - \texttt{RECYCT}) \cdot 3.638 \cdot \sqrt{T/m} \tag{92}$$

Despite this formula, it is quite common to use the `RECYCT` flag as a free parameter, fixing it when a good agreement with experimental data is obtained [59]. Regarding the puffing of neutrals, in section 4.2.3, we have anticipated that a transparent *additional surface* was placed in correspondence of the gas nozzle, in order to simulate the external inflow of neutrals. From this surface, particles are launched by EIRENE with a uniform angular distribution from 0° to 5° with respect to its normal unit vector. The actual angular distribution is not known experimentally, anyhow it is reasonable to think that the dominant direction of a puffed particle is orthogonal to the basis of the cylinder, so that angles higher than 5° have been excluded. The flux strength of puffed particles has been set equal to the experimental value measured by the puffing system. It has to be specified in the `b2.neutrals.parameters` input file in units of particles s^{-1}. The gas puff can be clearly seen from the results of an EIRENE standalone simulation (§3.1), shown in figure 38.

Having introduced these last two elements of the modeling, the results of the coupled simulations can be presented. In particular we performed a sensitivity analysis of some relevant physical parameter, such as the pumping rate, the anomalous transport coefficients and the external absorbed power, to understand how they affect the behaviour of the plasma quantities. In section 5.2.1 results of this analysis are shown. Comparison of the simulation results with available experimental data is shown in section 5.2.2.

5.2.1 *Sensitivity analysis of code free parameters*

As we have explained in the previous sections, there are many free parameters in the code to be chosen concerning GyM modeling. In this section, we present the effects on some of them on the plasma parameters. In particular, we will consider: (a) the pumping speed, related to the `RECYCT` flag; (b) the

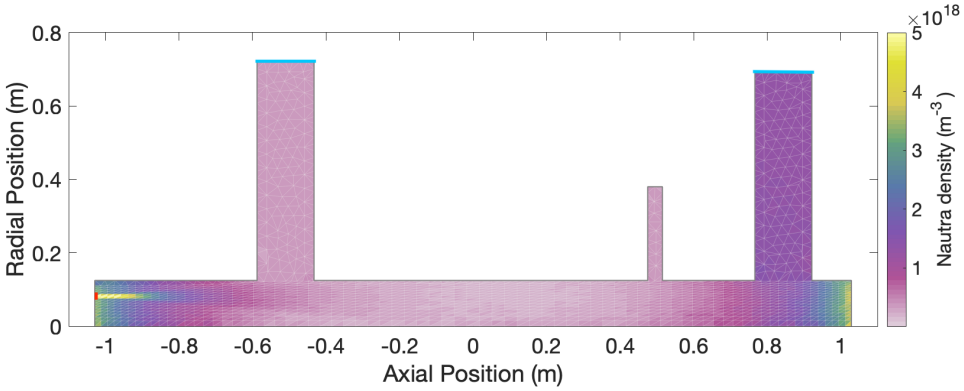

Figure 38: Neutral density (m^{-3}) simulated with the standalone version of EIRENE. The puffing segments is in colored in red on the *WEST* target and the pumping segments are in blue. The background plasma density to be provided to EIRENE has been obtained by a standalone fluid run with input parameters given in table 5.

radial anomalous transport coefficients, both related to density and pressure gradients; (c) the external power absorbed by electrons. The common input parameters used in these simulations are reported in table 7.
As discussed in section 3.4, convergence of the B2.5-EIRENE coupled simulations, can not be checked from the norms of the residuals. For these simulations, convergence has been monitored using the SOLPS-ITER `particle_balance.py` and `total_energy_balance_coupled` switches, which give respectively the particle and energy balances in the system. For the obtained results, the statistical fluctuations of the particle balance are limited to 0.5 %, without applying the solution average procedure discussed in section 3.4.

(a) **Variation of the `RECYCT` flag value**: as we have said in the introduction to this section, the surface albedo ($1-$`RECYCT`), representing the probability that a particle is absorbed by a surface, can be either fixed by means of the formula (92) or treated as a free parameter, in order to match the experimental data. In our simulations, the recycling probability has been varied from `RECYCT` $= 0.9$ to `RECYCT` $= 0.995$, in correspondence of the pumping segments. These two values correspond approximately to the `RECYCT` value obtained with equation (92), respectively considering the real circular area of the duct and the area of the annulus obtained rotating the top segment of the duct around the z-axis. The anomalous transport coefficients are fixed at $D_n = D_p = 0.75\,m^2\,s^{-1}$, also used in the standalone simulations presented in section 5.1. Results for the radial profiles of electron temperature, density, plasma potential and ion tem-

Input parameter	**Value**
Magnetic field	$B = 600\,\mathrm{A}$
Initial densities	$n_{Ar} = 1 \times 10^{18}\,\mathrm{cm}^{-3}$ $n_{Ar^+} = 1 \times 10^{17}\,\mathrm{cm}^{-3}$
Initial temperatures	$T_e = T_i = 7\,\mathrm{eV}$
Total external power	$P_e = 800\,\mathrm{W}$
Neutral Ar puffing	$\mathrm{Puff}_{\mathrm{Ar}} = 6.5 \times 10^{17}\,\mathrm{s}^{-1}$
Decay lengths	$\Lambda_{T_e} = \Lambda_{T_i} = \Lambda_n = \Lambda_\phi = 0.1\,\mathrm{m}$
Recycling probability	$RECYCT = 0.985$
Time-step	$dt = 1 \times 10^{-5}\,\mathrm{s}$
Number of iterations	$N_{iter} = 10000$

Table 7: Common input parameters for the coupled simulations. When a sensitivity analysis is performed, the corresponding parameter is let free to vary, according to the values reported in the text. All the other parameters are instead fixed at the value reported in this table.

perature are shown in figure 39. The general trend is that decreasing the albedo, electron density increases while electron temperature decreases. This is compatible with the fact that a decreasing albedo means a lower absorption probability for the neutral atoms, and so a higher Ar density in the plasma. This from one side allows to have a higher plasma density, since more neutrals are present to be ionized into $\mathrm{Ar}^+ + e^-$. On the other side it reduces the electron temperature because neutrals are injected into the plasma at ambient temperature and so they contribute to cool down the plasma.

(b) **Variation of the anomalous transport coefficients**: as we have discussed in section 2.4.3, at present no reliable theoretical model exists to infer the values of anomalous transport coefficients in the direction orthogonal to the magnetic surfaces. In absence of results from turbulence codes or experimental values, these are often treated as free parameters of SOLPS. In figure 40, the radial profiles for electron density and temperature, plasma potential and ion temperature are shown, considering different values for the anomalous transport coefficients D_p and D_n in equations (65) and (66). The latter are constant all over the plasma domain and go from $D_{p,n} = 0.5\,\mathrm{m}^2\,\mathrm{s}^{-1}$ to $D_{p,n} = 2.5\,\mathrm{m}^2\,\mathrm{s}^{-1}$. The general trend is that the electron density decreases faster going radially outward for higher diffusion coefficients. Consequently, in presence of a lower plasma density near the outer lateral boundary, the electron temperature peak is more intense in this case. Indeed, considering electron pressure

constant, temperature and density are inversely proportional according to $p_e \simeq k_B n_e T_e \simeq constant$.

(c) **Variation of the external power**: as discussed in section 4.3.2, in absence of a more detailed model describing the absorption of the radio-frequency wave in the plasma, the power absorption efficiency is also a free parameter. A sensitivity analysis of the effects of the variation of the total external power absorbed by electrons has been done and results are reported in figure 41. The power has been varied from 600 W to 2400 W, which corresponds respectively to 20 % and 80 % of the maximum RF source value currently available on GyM. The anomalous transport coefficients are fixed at $D_n = D_p = 1.5\,\mathrm{m^2\,s^{-1}}$. From figure 41, the dominant effect produced by the power absorbed by electrons is on the electron density. Indeed, the density increases almost linearly with the power, while the electron temperature decreases. This decrease in the electron temperature is related to the density increase by $p_e \simeq k_B n_e T_e \simeq constant$.

As a general comment, comparing figures 39, 40 and 41, it seems that the temperature and potential are strongly affected by the recycling coefficient, which in turn means that physically they are strongly affected by the presence of neutrals in the plasma. On the contrary the variation of the external power seems to mainly influence the plasma density, which increases almost linearly with it. Temperature and potential variations are instead much more limited. Finally, the anomalous transport coefficients mainly affect the shape of the radial profiles in the outermost region of the cylinder. Concerning ion temperature, it is in any case low since the only heating mechanism we are considering is ECR.

5.2.2 *Comparison with experimental data*

The last result we want to present concerning Ar simulations is the first comparison between SOLPS-ITER output and experimental data from Gym. Unfortunately, the available dataset relative to Ar plasmas on GyM machine is quite limited at the moment and so this comparison is far from being exhaustive and accurate. Nevertheless, the order of magnitude of the experimental data are correctly reproduced and partially also the qualitative radial profiles. Experimental data from GyM are acquired by means of a Langmuir probe, located almost at the center of the axial extension of the machine, as shown in figure 22. Langmuir probes allow to estimate electron density, temperature and plasma potential, as discussed in Appendix B. The probe is fixed on a shaft whose extension inside the plasma column can be varied so that radial profiles of the plasma quantities can be assessed. The experimental parameters of the Ar campaign on GyM are reported in table 8.

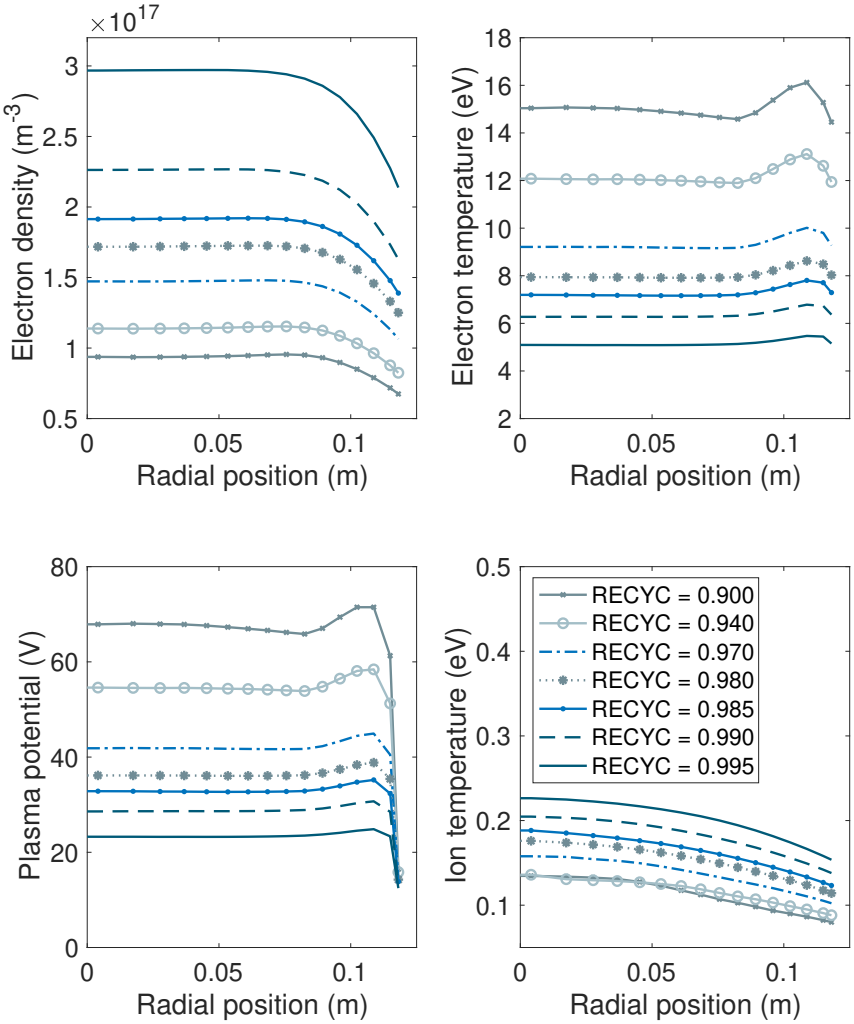

Figure 39: Radial profiles of electron temperature, density, plasma potential and ion temperature for different surface albedos.

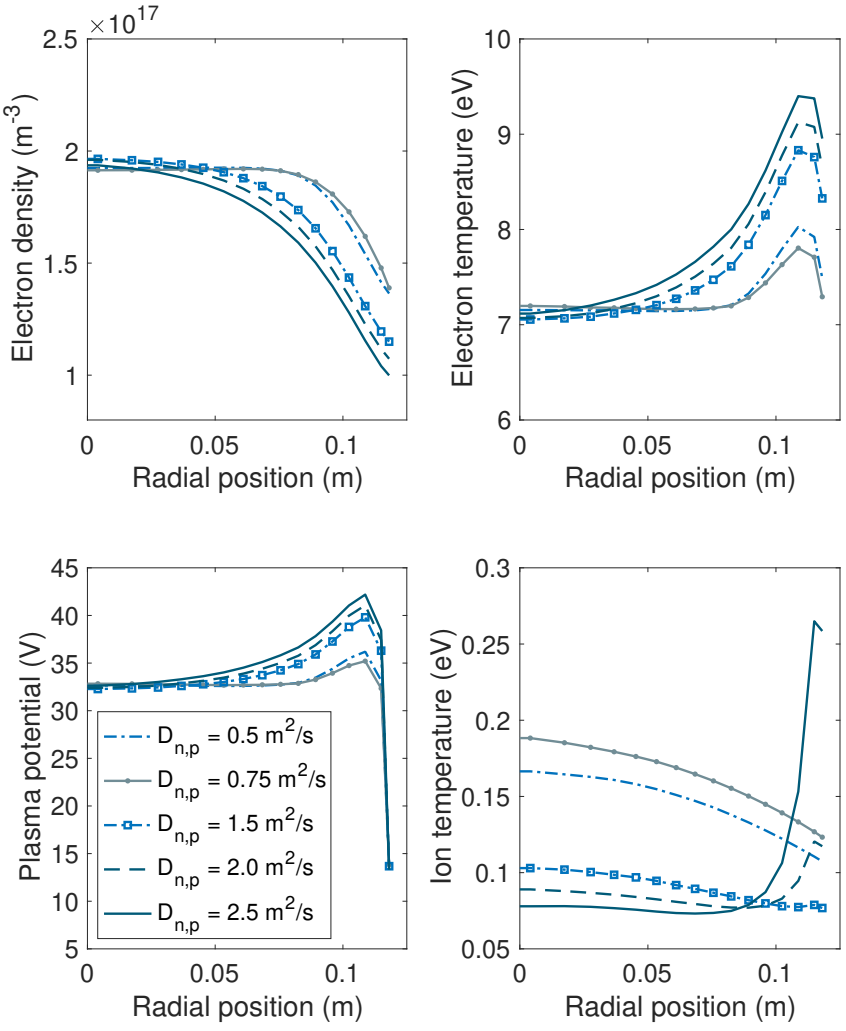

Figure 40: Radial profiles of electron temperature, density, plasma potential and ion temperature for different values of the anomalous transport coefficients D_p and D_n.

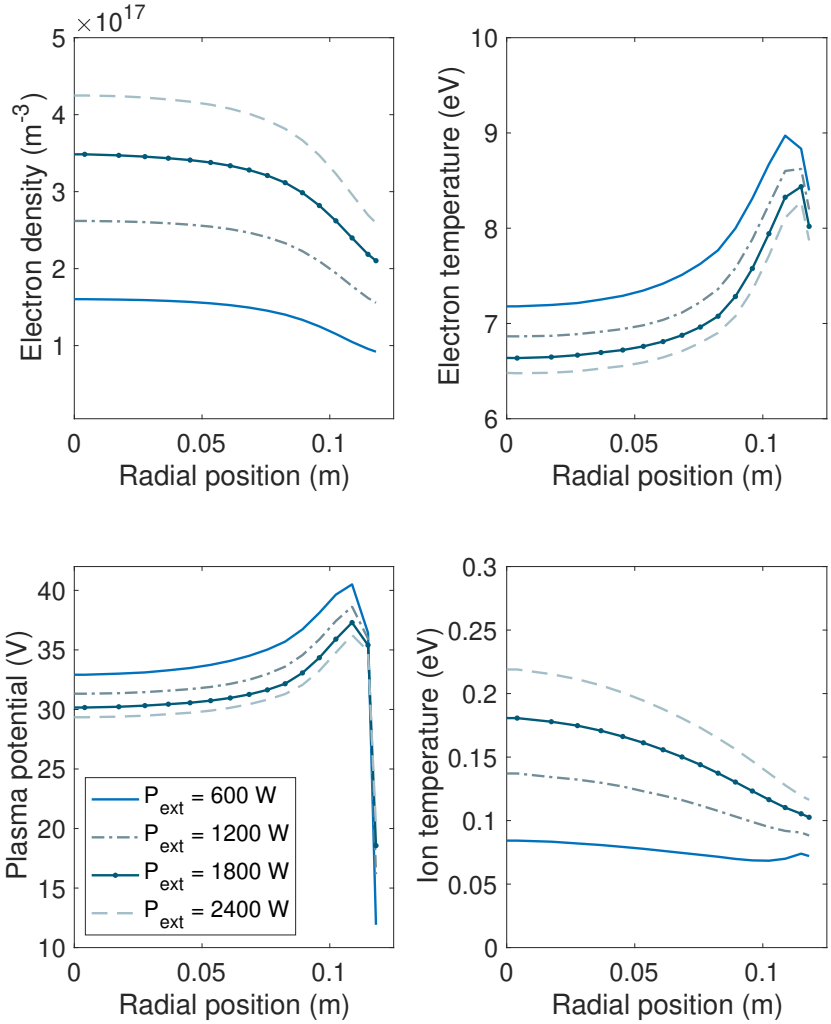

Figure 41: Radial profiles of electron temperature, density, plasma potential and ion temperature for different values of the absorbed power from the RF source.

Experimental parameter	**Value**
Magnetic field	$B = 600\,\mathrm{A}$
RF source power	$P_{RF} = 60\,\%\, P_{max} = 1800\,\mathrm{W}$
Neutral Ar puffing	$\mathrm{Puff_{Ar}} = 1\,\mathrm{sccm}_{N_2} \times 1.45 = 6.5 \times 10^{17}\,\mathrm{atoms\,s^{-1}}$
Neutral pressure	$P_{Ar} = 5.49 \times 10^{-5}\,\mathrm{mbar}$

Table 8: GyM experimental parameters for the Ar campaign. The puffing system is calibrated with N_2, so that the actual Ar flow rate must be corrected as $\mathrm{Puff_{Ar}} = \mathrm{Puff_{N_2}} \times 1.45$.

Two distinct analysis were performed: (a) the comparison between the simulated and experimental radial profiles of the plasma properties, estimated by changing the radial position of the probe head; (b) the comparison of the experimental temperature, density and potential values on the axis of GyM chamber, obtained for different powers of the radio-frequency source with simulated values corresponding to the same levels of absorbed power.

(a) *Radial profiles analysis.* Figure 42, shows the comparison between experimental data and the results of simulations described in section 5.2.1. Among all the results presented there, only those that better approximate the experimental values have been reported. As one can see, the density profile is almost exactly reproduced by the simulations but an overestimation within a factor two is observed. This is anyway a strong improvement with respect to the results obtained from previous simulations using SOLPS 5.1 [48], where the discrepancy in the plasma density was about a factor of 7. Concerning the electron temperature, the quantitative differences between simulations and experimental values are significantly smaller. Moreover, the temperature increase toward the outer border of the cylinder is captured by the simulations. On the contrary, the temperature increase in the central region is smaller in the simulations with low anomalous transport coefficients and it disappears for higher values of D_n and D_p. This issue can be related to the fact that we are probably imposing the wrong conditions on the *SOUTH* boundary, corresponding to the axis of the cylinder or also we are using the wrong radial profile for the external electron energy source. Lastly the simulated values for the plasma potential match quite well the experimental ones near the axis of the cylinder, while it is too low with respect to measured data near the outer border.

(b) *External power and power absorption efficiency.* Experimental data for different RF source values, 20 %, 40 %, 60 % and 80 % of the nominal 3 kW power, are available only for a fixed radial position of the Langmuir

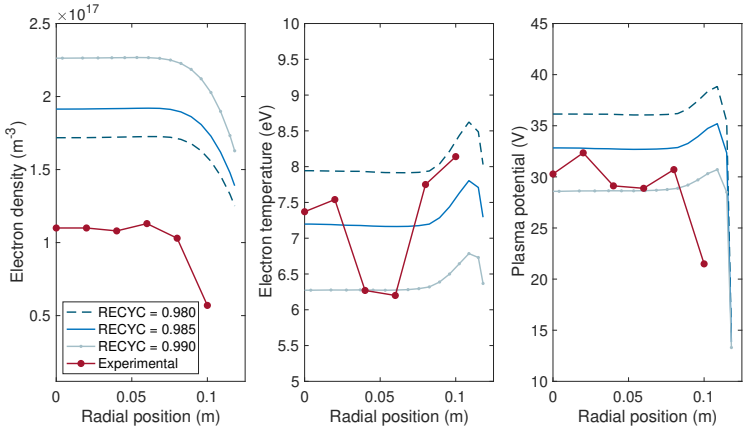

(a) *Experimental data VS albedos.*

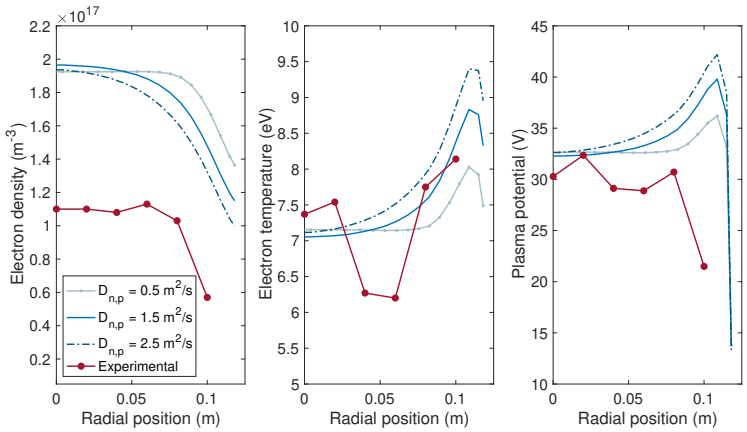

(b) *Experimental data VS anomalous transport coefficients.*

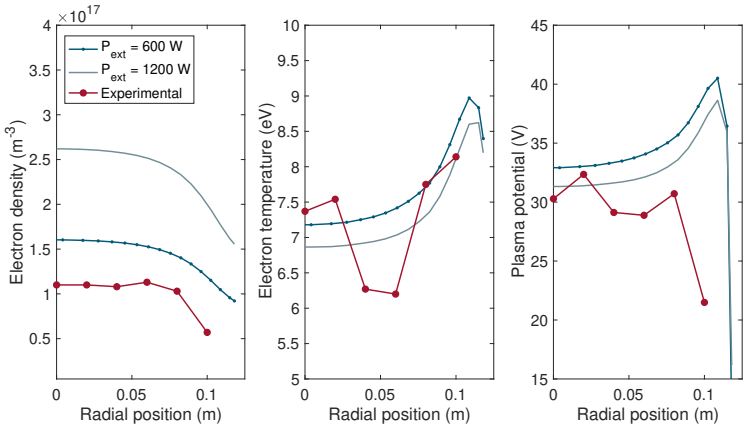

(c) *Experimental data VS external power.*

Figure 42: Comparison between SOLPS-ITER simulations and experimental data.

probe, corresponding to the axis of the cylinder, i. e. $R = 0$. Comments can be done already from the radial profiles in figure 42c. Concerning the electron density profiles, one can see that the best agreement between experimental and simulated data is obtained for low values of the simulated electron power source. The 600 W source profile, which better approximates the experimental curve, is obtained considering an absorbed power that is one third of the $P_{RF} = 1800\,\mathrm{W}$, actually emitted from the RF source when the set of experimental points were measured. In first approximation, we can model the absorption phenomenon introducing the adimensional coefficient η_a, which indicates the *power absorption efficiency*, i. e. the fraction of the total emitted power from the RF source, that is effectively absorbed by the plasma, $P_a = \eta_a P_{RF}$. As we have discussed in section 4.3.2, without a dedicated model for the wave propagation inside the vacuum chamber and the plasma, this parameter is unknown. A first estimation anyhow can be given comparing the experimental data with the results of our simulations. In figure 43, we have reported the comparison between measured and simulated values for the electron temperature and density on the axis of the cylinder, as a function of the power. The physical meaning of the power variable in abscissa is different for the two cases: indeed, simulated values refer to the *effective absorbed power*, while the experimental ones to the power emitted from the source. The linear increasing trend of the plasma density with the absorbed power, already pointed out from figure 41, is now clearly visible. Conversely, the experimental density growth with the source power is much more limited, as if the fraction of absorbed power decreases when a higher power is provided by the source. In figure 44 we have shown the approximated trend of the η_a parameter, computed as the ratio between the experimental and the simulated density $\eta_a = n_{exp}/n_{sim}$. From this figure, it can be inferred that only for low RF source level $\leq 20\,\%$ most of the energy is absorbed by the plasma, while for higher power levels the absorption efficiency saturates around $30 - 40\,\%$. The validation of these results has to be done by means of dedicated experimental campaigns.

5.3 COUPLED SIMULATIONS OF DEUTERIUM PLASMAS

Finally, the last section of this thesis work is dedicated to the discussion of results obtained from a B2.5-EIRENE coupled simulation performed considering a deuterium plasma. Contrary to what was done for Ar plasmas (§5.1 and §5.2), no sensitivity analysis of the code free parameters is done. In this sense, this last part of the work has to be thought as a preliminary study, in order to prove the feasibility to apply the SOLPS-ITER code to simulate deuterium plasmas in medium-flux linear devices, such as GyM, and enlighten the limits.

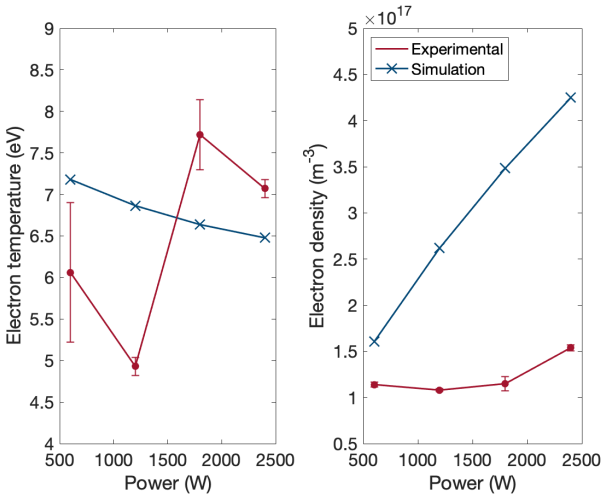

Figure 43: Electron temperature and density at the center of the machine as a function of power. The power variable represents the emitted power from the RF source, P_{RF}, when considering the experimental points, while concerning the simulations it has to be considered as the effective power absorbed by the plasma, P_a.

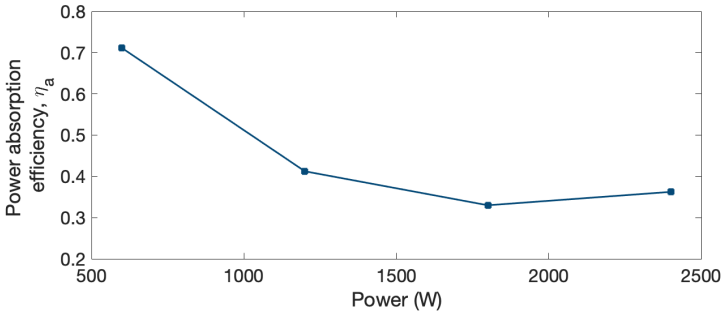

Figure 44: Power absorption efficiency η_a as a function of the power. This curve has been computed as the ratio between the experimental to the simulated density $\eta_a = n_{exp}/n_{sim}$.

In section 5.3.1, the results of the coupled B2.5-EIRENE simulation for D plasma is presented and compared with the experimental data. In light of what we have said on the aim of this D simulation, section 5.3.2 is dedicated to the discussion of the main limits which affect deuterium plasma simulations with SOLPS in medium-flux devices.

5.3.1 *Analysis of the results*

In this section the results of the D plasma coupled simulation are presented. The same geometry and boundary conditions used for the Ar simulations were used, with exception of the values of the electron temperature and density decay lengths Λ_{T_e} and Λ_n. Atomic and molecular processes considered in the simulations were suitably adapted to take into account most of the reactions shown in table 1. A higher neutral puffing rate was imposed, again fixing this parameter around the experimental value. The values of the input parameters used in this simulation are given in table 9.
The increased atomic and molecular complexity of this simulation reflects on a much higher computational cost: each Monte Carlo iteration, in fact, takes almost two order of magnitude more time to be performed than in case of a simpler Ar simulation. For this reason, only $N_{iter} = 5000$ iterations were performed. As we will see, this reflects on the statistical fluctuations in the solution which is higher in this case. Anyway, the degree of convergence of the simulation was checked through the overall particle and energy balance, as discussed in section 3.4, and fluctuations in the particle balance within $\sim 3\,\%$ were obtained. This value, although should be reduced for a detailed description increasing the number of iterations, can be considered sufficiently good for a first explorative analysis.

Radial profiles for electron density, temperature and plasma potential and the axial profiles for electron density, temperature and parallel velocity are shown in in figures 45 and 46, respectively. In figure 45, moreover, the experimental profiles obtained with the parameters reported in table 10, are shown. A set of 4 experimental points for each radial position was taken during the campaign. The error-bars shown in figure 45 represents the standard deviation of each set of measures. However, these are only a part of the overall experimental error, since the probe intrinsic error is not taken into account.
As one can see from the comparison of simulations and experiments, also in this case the order of magnitude of the experimental points is correctly reproduced by the code. Moreover, as it has been found for the Ar simulations, the code overestimates the plasma density within a factor of 2. The electron temperature and plasma potential are correctly estimated in the region around $r = R_{GyM}/2 \simeq 0.06\,\mathrm{m}$, while they are underestimated both near the axis of the machine and the outer border. Following the results shown in figure 40 for

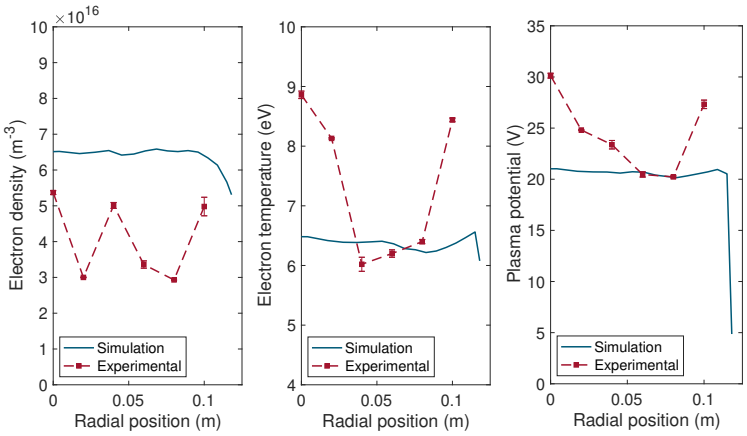

Figure 45: Results of the coupled simulation for deuterium plasma compared with experimental data. The error-bars on the experimental points are computed as the standard deviation of the available experimental measure, ~ 4 measures per point.

the Ar simulations, anyway, an increase of the temperature and potential in the outer region of the machine can be obtained in principle considering higher anomalous transport coefficients D_n and D_p.

5.3.2 *Considerations on D_2^+ mean free path*

We conclude the analysis of SOLPS simulations pointing out the main limits we have identified in the modeling of deuterium plasmas in GyM linear device with B2.5-EIRENE. As discussed in section 2.5, SOLPS package has been already applied to different linear devices to simulate deuterium plasmas. All these machines, anyway, have been designed to produce higher particle fluxes than the one that can be reached with the present RF source in GyM. Furthermore, the value of the particle flux, and consequently of the plasma density, strongly affect the legitimacy of many approximations made by the code (§3.3.3).
Here we want to check *a posteriori* the validity of the *test ions static approximation* described in section 3.3.3. As discussed, within this approximation, D_2^+ ions are considered *short-lived species*, meaning that after their formation from ionization of D_2 molecules, their motion inside the plasma is not followed and the next collision leading to the ion dissociation is supposed to happen at the location of birth. In this section, the soundness of this approximation in the frame of GyM plasma modeling is addressed, computing the D_2^+ mean free path and comparing it with the grid size used in the simulation. The static approximation is satisfied if the mean free path is smaller than the cell size along the plasma column.

Input parameter	**Value**
Magnetic field	$B = 600\,\mathrm{A}$
Initial densities	$n_D = 1 \times 10^{18}\,\mathrm{cm}^{-3}$ $n_{D^+} = 3 \times 10^{16}\,\mathrm{cm}^{-3}$
Initial temperatures	$T_e = T_i = 8\,\mathrm{eV}$
Total external power	$P_e = 800\,\mathrm{W}$
Neutral Ar puffing	$\mathrm{Puff_{Ar}} = 5 \times 10^{19}\,\mathrm{molecules\,s}^{-1}$
Decay lengths	$\Lambda_{T_e} = \Lambda_n = 0.05\,\mathrm{m} \quad \Lambda_{T_i} = \Lambda_\phi = 0.1\,\mathrm{m}$
Anomalous transport coefficients	$D_n = D_p = 0.75\,\mathrm{m}^2\,\mathrm{s}^{-1}$
Recycling probability	$RECYCT = 0.990$
Time-step	$dt = 1 \times 10^{-5}\,\mathrm{s}$
Number of iterations	$N_{iter} = 5000$

Table 9: Input parameters for the D coupled simulation.

Experimental parameter	**Value**
Magnetic field	$B = 600\,\mathrm{A}$
RF source power	$P_{RF} = 40\,\%P_{max} = 1200\,\mathrm{W}$
Neutral Ar puffing	$\mathrm{Puff_D} = 34.5\,\mathrm{sccm}$
Neutral pressure	$P_D \simeq 1.5 \times 10^{-4}\,\mathrm{mbar}$

Table 10: Gym experimental parameter for the D campaign.

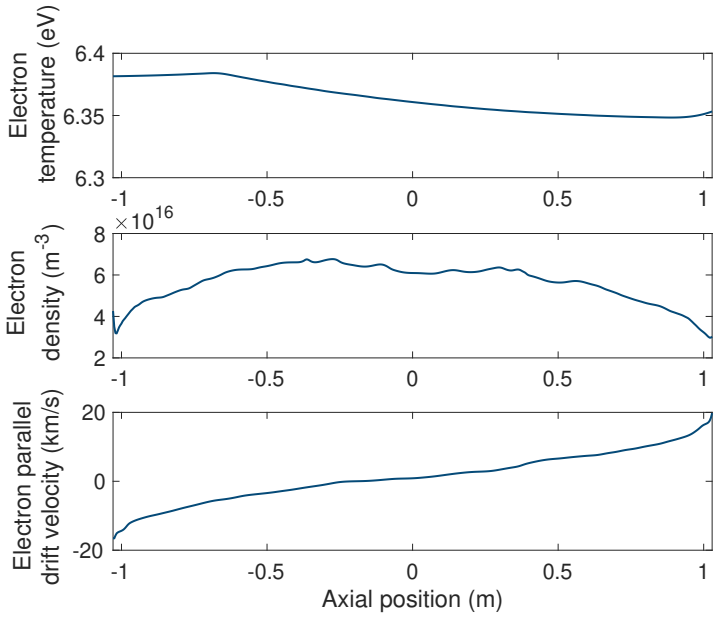

Figure 46: Axial profiles for the electron temperature, density and parallel velocity obtained from the coupled simulation. These profiles were used to compute the D_2^+ mean free path as discussed in section 5.3.2.

The D_2^+ mean free path is estimated rewriting the integral in equation (80) for the collision frequency as

$$\nu_t = \sum_k^3 n_b \langle \sigma_k v_{rel} \rangle = n_b \langle \sigma_t v_{rel} \rangle \tag{93}$$

where n_b is the background plasma density, and the three reaction rates considered to obtain the *total reaction rate* $\langle \sigma_t v_{rel} \rangle$ are related to H_2^+ dissociative ionization, dissociation and recombination shown in figure 12. Substituting this expression for the collision frequency, into equation (79) for the macroscopic cross section, one obtains that the D_2^+ mean free path is given by

$$\lambda_{D_2^+} \simeq \frac{|\mathbf{V}_\parallel|}{n_b \langle \sigma_t v_{rel} \rangle} \tag{94}$$

where the electron velocity has been approximated with its parallel component. Before showing the results obtained for the GyM machine, we want to validate the consistency of this method, comparing the results obtained from equation (94) with available literature results. To do so, we evaluated the axial mean free path profile for the Pilot PSI linear machine [40]. Results of this benchmark are shown in figure 47a. As one can see, both qualitative and quantitative agreements are good.
To compute the D_2^+ mean free path in GyM by means of equation (94), we considered the axial profiles for electron temperature, density and velocity shown

	Pilot-PSI	**GyM**
Electron temperature T_e	$\sim 2\,\mathrm{eV}$	$\sim 8\,\mathrm{eV}$
Electron density n_e	$\sim 1 \times 10^{-20}\,\mathrm{m}^{-3}$	$\sim 4 \times 10^{-16}\,\mathrm{m}^{-3}$
Parallel velocity $\lvert V_\parallel \rvert$	$\sim 5\,\mathrm{km\,s}^{-1}$	$\sim 12\,\mathrm{km\,s}^{-1}$

Table 11: Comparison between typical deuterium plasma parameters of Pilot-PSI and GyM.

in figure 46. The reaction rates were computed using the numerical fits given in the AMJUEL database [19], as discussed in section 2.3.2. Comparison of the results for GyM and Pilot-PSI are shown in figure 47b. This figure is instructive because it points out the almost exact proportionality between the mean free path and the plasma density, $\lambda_{D_2^+} \propto n_b^{-1}$. This can not be directly inferred from equation (94), since also the reaction rate in principle depends on the background plasma density. Anyway, if one compares the average values of the density, reported in table 11, and the mean free path values, difference of four orders of magnitude in the plasma density corresponds almost exactly to four orders of magnitude difference in the $\lambda_{D_2^+}$.

In figure 48, we have reported the axial variation of the D_2^+ mean free path in comparison with the electron density and temperature gradients and the grid size. Concerning the density gradient, the statistical fluctuations which affect this simulation, as discussed in section 5.3.1, are here clearly visible. Moving to the more relevant result, comparing the dotted black line for the grid size and the solid blue one for $\lambda_{\mathrm{D}_2^+}$, it is clear that only in a very small region of the domain, around the center of the machine, the value of the D_2^+ mean free path is lower than the dimension of the grid cells. Consequently, the static approximation that was used in the simulation presented in section 5.3.1 is partially satisfied throughout most of the plasma domain. To better assess the effects of the static approximation on the simulation results, it should be useful to tray to relax this approximation computing test ion transport.

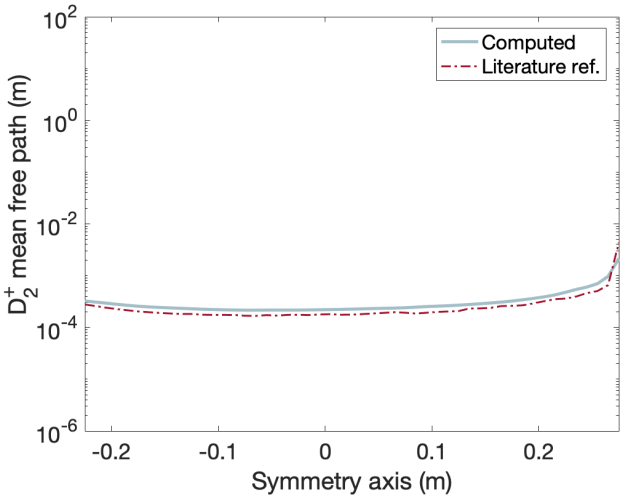

(a) *Benchmark of the D_2^+ mean free path in Pilot-PSI from [40].*

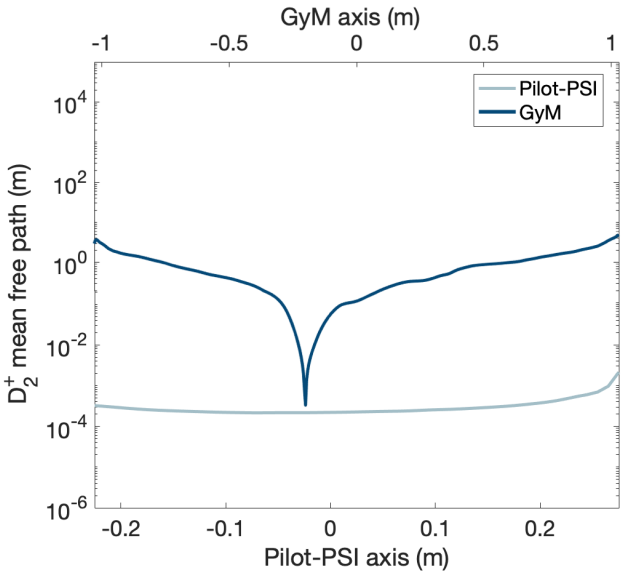

(b) *Comparison of the D_2^+ mean free path for Pilot-PSI and for GyM.*

Figure 47: D_2^+ mean free path in Pilot-PSI and GyM linear devices. The cusp around $Z \simeq -0.2\,\mathrm{m}$ in GyM profile for $\lambda_{D_2^+}$ is due to the change in the direction of the electron parallel velocity around that axial position (see figure 46). This peaked behaviour is enhanced by the logarithmic scale.

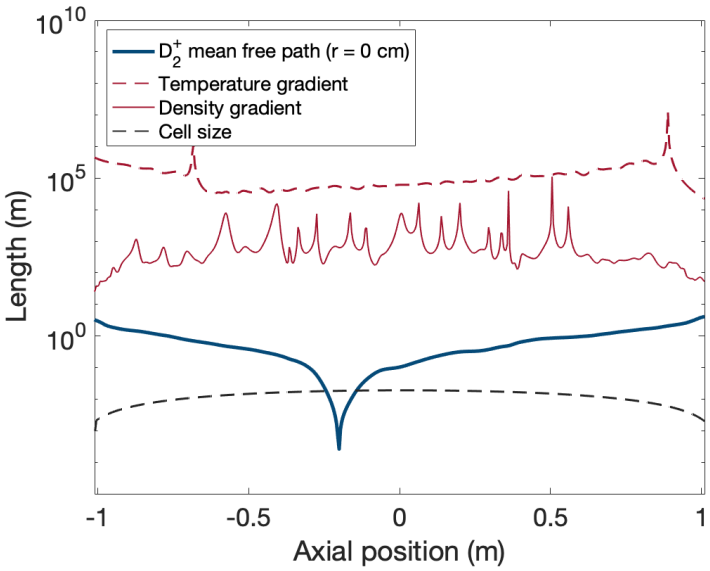

Figure 48: D_2^+ mean free path in GyM, compared to the other relevant lengths. In particular, the electron temperature gradient ∇T_e, the electron density gradient ∇n and the grid size are considered.

6

CONCLUSIONS AND PERSPECTIVES

In this thesis work, the SOLPS-ITER edge transport code was used to simulate GyM linear plasma device. To our knowledge, works on the application of this code version to a linear device have not been published yet, even though the interest of the fusion community to the application of this kind of boundary transport codes to linear machines is increasing in recent years. This thesis work, then, represents one of the first attempts to simulate nuclear fusion relevant plasma in linear devices, through the application of the latest version of the SOLPS package.
After a brief introduction to the subject of nuclear fusion in chapters 1 and 2, the SOLPS code for boundary plasma transport has been described in chapter 3 referring to its application to tokamaks. Benchmark simulation of the Asdex Upgrade (AUG) device have been performed, using the input files available among the examples provided by the code developers. These simulations were used to discuss the convergence behaviour of the code and compare standalone and coupled simulation outputs. In chapters 4 and 5, the attention has moved to linear devices. First, the GyM machine was introduced and several issues related to its modeling have been discussed. Due to the strong anisotropy in the transport of charged particles in a magnetic field, the computational mesh for the fluid code must have two sides of its rectangular cells aligned to the magnetic field lines. For this reason, we have discussed how the magnetic equilibrium configuration was computed under the hypothesis of ideal MHD and how the computational mesh was built. The modeling of the plasma source, which exploits electron cyclotron resonance mechanisms to generate and heat up the plasma, has also been addressed. Part of this work, was based on previous application of the SOLPS 5.1 code to GyM [48]. Anyhow, an improved awareness about the mesh construction procedure and source modeling has been acquired. In chapter 5, the results of the simulations have been presented. In this thesis work, SOLPS-ITER was used in B2.5 standalone and B2.5-EIRENE coupled modes to simulate argon and deuterium plasmas. B2.5 standalone Ar simulations were performed to test mainly numerical aspects of the code: convergence issues, comparisons between SOLPS 5.1 and SOLPS-ITER outputs and sensitivity the code to temporal and spatial discretization were analyzed. With B2.5 EIRENE coupled Ar simulations, instead, sensitivity analysis of many physical code parameters has been performed to asses their effects on the plasma parameters. In particular behaviour of the electron temperature, density and plasma potential following a variation of the pumping absorption, transport coefficients and external power has been investigated.

More complex plasmas generated from molecular D_2 gas have also been simulated. Only B2.5-EIRENE coupled mode was used in this case, exploitiong the full potential of the code to simulate involved atomic and molecular processes happening in collisions between the different species.

The following specific conclusions can be drawn from this work:

- ◇ The application of the SOLPS-ITER code to linear devices is possible and stationary solutions were obtained for both standalone and coupled cases. However, the optimization of the code for tokamak devices does not guarantee that the default inputs which allows convergence in toroidal geometry, produces converged solutions in the linear case.

- ◇ Sensitivity analysis of many physical parameters was performed for argon plasmas, using the B2.5-EIRENE coupled mode. From this analysis, we have seen that: increase of the neutral density, obtained by changing the pumping speed, strongly reduces electron temperature and plasma potential; the effects of anomalous radial transport coefficients is mainly related to the shape of the radial profiles of plasma quantities; increase of the absorbed power produces higher plasma density and lower electron temperature and potential.

- ◇ Comparison between coupled Ar simulation results and the available experimental data shows that electron temperature and plasma potential are qualitatively and quantitatively reproduced by the code. As regards the electron density, discrepancy less than a factor of 2 are observed. This accuracy can be for sure increased, once the code free parameters have been fixed and more extensive and complete set of experimental data have been produced.

- ◇ The SOLPS-ITER code has been used to successfully simulate the medium-flux deuterium plasma produced of GyM. The regime of densities reached in this machine is ~ 4 orders of magnitude lower than typical plasma densities of the other linear devices simulated with the SOLPS code. Nevertheless, this thesis work shows that solutions with a good quantitative agreement with experimental data have been obtained without optimization of the code free parameters. Moreover, these encouraging conclusions have been reached even if the soundness of the static approximation of test ions made by EIRENE is only partially satisfied.

Starting from the results provided by this thesis work, both experimental and theoretical developments can be contemplated.
From the experimental point of view, this machine is currently employed mainly to study surface modifications and erosion due to the action of the plasma on suitably fusion-relevant targets and to investigate the mechanisms of ammonia

formation in presence of nitrogen impurities in deuterium and hydrogen plasmas. On the contrary, only limited sets of experimental data on the plasma parameter exist at present. In order to improve the code capability to reproduce GyM measured data, an extended and reliable experimental characterization of the Gym plasma is required. Indeed, many of the code free parameters can be fixed from the comparison of the simulation results and the experimental points. To this aim, the existing GyM diagnostic system, i. e. Langmuir probes and the optical emission spectroscopy, should be used to asses electron temperature, density and plasma potential for different radial and axial positions in the chamber and varying experimental pressure and power conditions. In addition, new diagnostic systems should be studied and designed in order to evaluate the anomalous transport coefficients.
Moreover, the alternative magnetic field configurations presented in section 4.4, have never been experimentally tested on the machine. Both experimental and numerical characterization of the plasma parameters should be performed in theses cases. The comparison of simulation results for different magnetic configurations with the corresponding experimental data is important to test the code versatility. Moreover, they offer alternative options which could be used to optimize GyM plasma parameters.
Among the theoretical aspects that should be more deeply studied, a detailed investigation of the RF wave propagation and absorption in GyM plasmas can help to improve the simulations accuracy. Indeed, this would allow to better model the intensity and shape of the absorbed energy from the external RF source, which has we have seen strongly influence plasma parameters.
As regards aspects related to the SOLPS-ITER code, the effects of the static approximation of test ions should be investigated in order to correctly simulate deuterium plasmas and partial relaxation of this approximation should be considered.
The optimization of the code performances to simulate the GyM machine is also important to exploit such a numerical tool with predictive purposes. This aspect, which can be developed starting from this first promising results, could be used to perform predictive numerical simulations to foreseen the plasma characteristics that new device configurations allow to reach. In particular, special interest is related to the possibility to foreseen plasma parameters expected from the installation of a new 28 GHz gyrotron source that is planned to be installed on GyM.

Considering aspects more relating to the framework of international nuclear fusion research, it is clear that the exploitation of the SOLPS-ITER code is of primary interest to simulate both linear devices and tokamaks. Specifically concerning linear machines, this code can be used to study divertor relevant phenomena such as plasma detachment and the transport of plasma impurities eroded from the PFCs. These studies should be performed also considering

other linear devices, with flux and density regimes different from GyM, which can reproduce the plasma characteristics of present day and future tokamaks SOLs. Moreover, transport codes like SOLPS-ITER offer the possibility to be coupled to turbulence or plasma-material interaction codes, for dedicated studies on edge physics and PWI. Regarding the coupling with turbulence codes, it would allow to obtain the anomalous transport coefficients for the cross-field diffusion of particles and heat in a consistent way. The coupling with PWI codes, instead would allow to investigate the effects of plasma-material interaction also from the "material point of view". These code can be used to help the interpretation of results of these experimental campaigns devoted to the exposure of fusion relevant materials. In the context of the coupling of these kind of numerical codes, the geometry simplifications offered by linear devices should be considered of major interest in order to focus on the physical phenomena of interest.

In conclusion, the present work may represent a starting point for future, deeper numerical studies on plasma transport in linear devices, aimed to extend the knowledge in the field of plasma edge transport in tokamaks, relevant for nuclear fusion applications.

APPENDIX

A

ADDITIONAL ASPECT ON PLASMA POWER BALANCE

In this Appendix, additional aspects related to the plasma power balance in a nuclear fusion reactor are presented. In particular, derivation of the power balance equation and the Q factor expressions in terms of plasma quantities, is given. For a more complete derivation of the relationship between Q and Q_E we refer to [27].

The thermal power gained by the plasma can be represented by two terms: the external power P_{ext} and the power produced by fusion reactions. Concerning the latter, the fraction that is kept by the plasma is only the power associated to the alpha particles P_α. Neutrons in fact rapidly escape from the plasma, being electrically neutral. The losses instead can be described in first approximation by *Brehemsstrahlung* radiation P_R and heat conduction P_Q. In steady state, then, the following power balance per unit volume must be verified:

$$P_{ext} + P_\alpha = P_R + P_Q \tag{95}$$

The power associated to α particles, Brehemsstrahlung radiation and heat conduction can be directly related to plasma quantities. To do that, we consider a D-T plasma in which positive and negative charged particle densities are equal, $n_e \simeq n_i \equiv n$ and where the two populations of ions have densities equal to half the total plasma density n. From equation (8), we can write:

$$P_\alpha = \frac{n^2}{4} \langle \sigma v \rangle_{DT} E_\alpha \tag{96}$$

where the α energy per fusion reaction E_α is 3.5 MeV, as already mentioned. The power radiated by Brehemsstrahlung can be written as [27]:

$$P_R = c_B Z_{eff}^2 n^2 T^{1/2} \tag{97}$$

where c_B is a constant and the effective charge Z_{eff} is equal to 1 for D-T plasmas. However, the interaction of the plasma with the vessel structures leads to the production of impurities which increase the effective atomic number Z_{eff}, thereby enhancing radiation losses. Finally, heat conduction in the approximation of a steady state plasma can be expressed as:

$$P_Q = \frac{3nT}{\tau_E} \tag{98}$$

here τ_E is the energy confinement time and represents the e-folding relaxation time of the plasma energy due to heat conduction.

Referring to equation (95), some general considerations about the possibility to sustain a steady-state fusion reaction are usually made. In particular, we are now interested in self-sustained fusion reaction, meaning that we will neglect the power supplied by external sources.
First, neglecting the power losses due to conduction we have what is called the *ideal ignition condition*. In this case to have a self-sustained plasma we must have $P_\alpha > P_R$, and using equation (96) and equation (97) we can define the *ideal ignition temperature*:

$$T_{id} = \frac{\langle \sigma v \rangle_{DT}^2 \, E_\alpha}{4 c_B} \tag{99}$$

which represents the lower limit that must be exceeded to have any fusion yield. From the definition in equation (99), it is easy to understand why D-T fusion is much more feasible than D-D fusion. Substituting into (99) the correct values for $\langle \sigma v \rangle$ and E, we obtain $T_{id}^{DT} = 4.4\,\mathrm{keV}$, while for D-D reactions $T_{id}^{DD} = 32\,\mathrm{keV}$.
The second consideration allows us to introduce the so-called *Lawson criterion* and to define the condition for the plasma *ignition*. We will consider the steady state power balance of equation (95), again without external heating, but considering heat conduction losses. A self-sustained plasma requires $P_\alpha > P_R + P_Q$. Again substituting equations (96), (97), we obtain:

$$n\tau_E \geq \frac{12T}{\langle \sigma v \rangle \, E_\alpha - 4 c_B T^{1/2}} \tag{100}$$

the factor $n\tau_E$ is called *Lawson parameter* and if we plot it as a function of temperature, for the relevant case of D-T reaction we can see that it attains a minimum value for $T \simeq 25\,\mathrm{keV}$. Considering this value of temperature, we obtain from equation (100):

$$n\tau_E \geq 2 \times 10^{14}\,\mathrm{s\,cm^{-3}} \tag{101}$$

which is the so-called *Lawson criterion* [44].
Lastly, a simple and explicit form for the physics gain factor Q as a function of the plasma parameters $Q = Q(n\tau_E, T)$ is given. The *total power out* is given by $P_{out} = (P_n + P_R + P_Q)V$, where $P_n = (E_n/E_\alpha)P_\alpha = 4P_\alpha$ and V is the total plasma volume. Similarly, the total external power supplied is $P_{in} = P_{ext}V$, hence

$$Q = \frac{4P_\alpha + P_R + P_Q - P_{ext}}{P_{ext}} \tag{102}$$

Substituting the expression for P_{ext} from equation (95), we obtain $Q = P_f/P_{ext} = (P_\alpha + P_n)/P_{ext} = 5P_\alpha/(P_R + P_Q - P_\alpha)$. If for simplicity Bremsstrahlung is neglected, substituting equation (96) for P_α and equation (98) for P_Q, then finally leads to the following expression for Q:

$$Q = 5\frac{n\tau_E}{(n\tau_E)_{id} - n\tau_E} \quad \text{where} \quad (n\tau_E)_{id} \equiv \frac{12T}{\langle \sigma v \rangle_{DT} \, E_\alpha} \tag{103}$$

The interesting regime for a steady state power reactor is defined by a Q value in the regime $0 < Q < \infty$, or in terms of $n\tau_E$ for $n\tau_E \leq (n\tau_E)_{id}$.

B

LANGMUIR PROBES

The *Langmuir probe* is probably the simplest diagnostic method to measure plasma properties, like electron temperature, density and plasma potential [53]. It consists essentially of a small metallic object, biased and introduced into the plasma. Plasma properties can be estimated by measuring the current which flows through the probe for different values of applied voltage. Although it is very simple to be realized, a Langmuir porbe is an intrusive, not remote, technique and the probe must be carefully designed so as not to interfere with the plasma nor be destroyed by it. Worse than that, the interpretation of the *current-voltage curves* presents many difficulties related to the fact that the electrons and ions are not monoenergetic and often have very different temperatures [52]. Comparisons with other measurement techniques in tokamaks show that the agreement can be to within a factor of 2 or better, for both T_e and n_e [75].

In section 2.3.1 we have discussed some properties of the electrostatic sheath implicitly assuming that the surface in contact with the plasma is *electrically isolated*, of *floating*. We have said that whenever a solid object is inserted into the plasma, the so-called *floating potential* ϕ_f, i. e. the difference between the *plasma potential* ϕ_p and the potential of the floating solid surface, spontaneously arises to preserve a divergence-less current density, $\nabla \cdot \mathbf{j} = 0$. It can be easily shown [74] that, equating the electron and ion fluxes at the surface, $\Gamma_w^e = \Gamma_w^i$, the floating potential is

$$\frac{e\phi_f}{T_e} = 0.5 \log \left[\left(2\pi \frac{m_e}{m_i} \right) \left(1 + \frac{T_i}{T_e} \right) \right] \tag{104}$$

To understand the working principles of a Langmuir probes, we have to understand the effects of an external bias ϕ_B applied to the object in contact with the plasma. First a net current is drawn through the external circuit, so that $\Gamma_w^e \neq \Gamma_w^i$. When the probe is biased at a potential that is much more negative than the plasma potential, the electrons are repelled from the surface and the probe collect the so called *ion saturation current* I_{sat}^i [52].

$$I_{sat}^i = 0.6 e n_i \sqrt{\frac{T_e}{m_i}} A_{probe} \tag{105}$$

Increasing the probe voltage, ions start to be repelled and the ion current varies with ϕ_B according to

$$I^i(\phi_B) = \begin{cases} -I_{sat}^i \exp\left[e(\phi_p - \phi_B)/T_i\right] & \phi_B < \phi_p \\ -I_{sat}^i & \phi_B \leq \phi_p \end{cases} \tag{106}$$

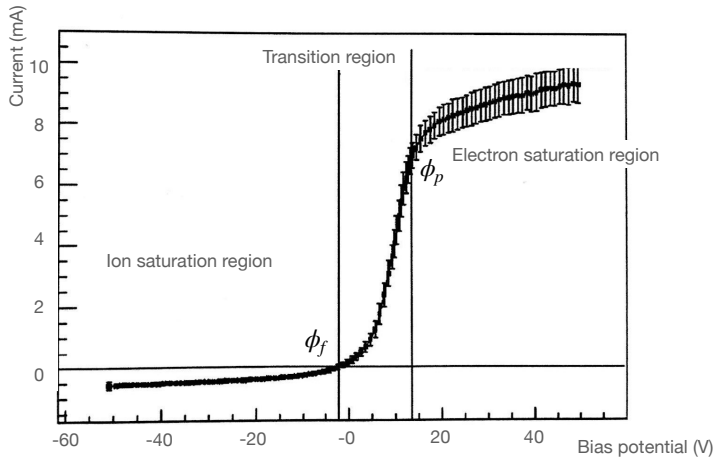

Figure 49: Langmuir probe characteristic.

The opposite, of course, happens for electrons: when the biasing potential is much higher than ϕ_p, the collected current is named *electron saturation current* I^e_{sat} and is given by [52]

$$I^e_{sat} = \frac{1}{4} e n_e \sqrt{\frac{8T_e}{\pi m_e}} A_{probe} \tag{107}$$

Reducing the external voltage, the electron current decreases as

$$I^e(\phi_B) = \begin{cases} I^e_{sat} \exp\left[-e(\phi_p - \phi_B)/T_e\right] & \phi_B \leq \phi_p \\ I^e_{sat} & \phi_B > \phi_p \end{cases} \tag{108}$$

It is clear from equations (105) and (107), that the electron saturation current is much larger than the one for the ions.

The *Langmuir probe characteristic*, shown in figure 49, is the curve obtained plotting the current measured by the probe as a function of the biasing potential $I = I(\phi_B)$. The current seen by the probe is, the sum of the electron and ion currents, $I(\phi_B) = I^i(\phi_B) + I^e(\phi_B)$. From this figure we can clearly distinguish three regions: (1) the *ion saturation region*, on the left, characterized by a small negative current I^i_{sat}; (2) increasing the biasing potential, electrons start to be collected, even if they are retarded by the biasing potential, producing a rapid increase in the collected current. This region is usually called *transition region*; (3) when $\phi_B \geq \phi_p$, the *electron saturation region* is reached.
According to what we have said in section 2.3.1 and also at the beginning of this Appendix, the floating potential ϕ_f corresponds to a null current in the

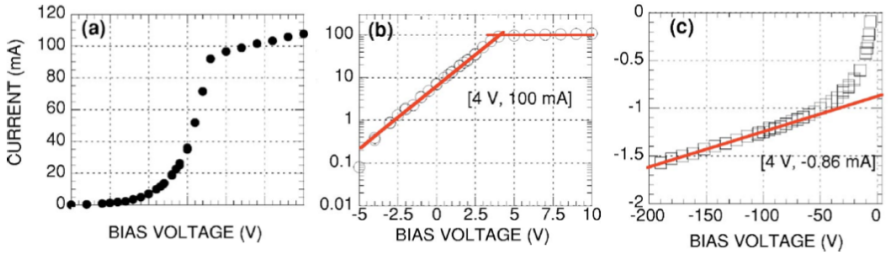

Figure 50: Enlargement of different regions of a Langmuir probe characteristic from [52]. (a) Total current. The negative ions saturation current is imperceptible with this resolution. (b) Transition region. The electron temperature T_e can be estimated from the logarithm of $I(\phi_B)$ using equation (110) in the transition region. (c) Enlargement of the ion saturation region.

plasma, i. e. $I(\phi_B = \phi_f) = I^i(\phi_B) + I^e(\phi_B) = 0$. Hence from equations (106) and (108)

$$\phi_f = \phi_p + \left(\frac{T_e}{e}\right) \log\left(0.6\sqrt{\frac{2\pi m_e}{m_i}}\right) \tag{109}$$

Inverting equation (109), the plasma potential can be estimated. Then the electron temperature T_e can be computed as the slope of the curve in the *transition region* in box (b) figure 50:

$$T_e = \frac{e(V_{t,2} - V_{t,1})}{\log\left(I_{t,2}/I_{t,1}\right)} \tag{110}$$

and the electron and ion densities are consequently computed from equations (105) and (107). For what concerns the ion temperature, T_i, the difference in the masses between electrons and ions which, as we have said, reflects on the different saturation current intensities makes impossible to measure this quantity with this diagnostic method.

C

CURVILINEAR COORDINATE SYSTEM FOR PLASMA EDGE

As we have seen in section 3.3.1, there are two possible coordinate systems adopted to describe plasma edge physics in tokamak geometry. They are the *dynamical frame* $(\mathbf{e}_\parallel, \mathbf{e}_\perp, \mathbf{e}_r)$ and the *geometrical frame* $(\mathbf{e}_\theta, \mathbf{e}_r, \mathbf{e}_\phi)$, in B2.5 indicated as (x, y, z). The two coordinate systems are shown in figure 16.
In this Appendix, we want to describe the fundamental coordinate transformations required to rewrite the Braginskii equations from cartesian to curvilinear reference frames.

The local position of a point $\mathbf{s}$ in the cartesian reference frame is written as

$$\mathbf{s} = x\mathbf{e}_x + y\mathbf{e}_y + z\mathbf{e}_z \tag{111}$$

where $\mathbf{e}_x$, $\mathbf{e}_y$ and $\mathbf{e}_z$ are the three cartesian orthonormal basis vectors. The same position can be specified using an *orthogonal curvilinear coordinates* (q_1, q_2, q_3), for which the local direction of the coordinate axes is generally different in each point of the space. In this case, we define the *local basis vectors in covariant form* $\mathbf{h}_i$ as

$$\mathbf{h}_i = \frac{\partial \mathbf{s}}{\partial q_i} \tag{112}$$

These vectors, although represent a licit basis for the description of the system in curvilinear coordinates, are not in general convenient when dealing with physical problems. This is related to the fact that vectors $\mathbf{h}_i$ are not in general dimensionless nor normalized to one, meaning that if we want to use them to write the vector $\mathbf{A}$ as[1]

$$\mathbf{A} = a_i \mathbf{h}_i \tag{113}$$

where $\mathbf{A}$ has a defined physical dimension, e. g. velocity, it is not guarantee that the three components a_1, a_2 and a_3 have as dimensions velocities. It is clear then, that to have a more immegiate physical description of the problem, it is convenient to introduce the corresponding normalized reference frame, where each component represents the effective length of the vector in a given direction. If we divide the local bases vector $\mathbf{h}_i$ for the corresponding *Lamè coefficient* $h_i = |\mathbf{h}_i|$, we obtain the local *unit-basis vector* $\mathbf{e}_i = \mathbf{h}_i / h_i$ and

$$\mathbf{A} = \tilde{a}_i \mathbf{e}_i \tag{114}$$

1 Here and in the following Einstein notation is used, so that summation over repeated indexes is understood.

is written in the so-called *physical components* $\tilde{a}_i$ with the correct physical dimensions. Moreover, comparing equation (112) and (114) and substituting the definition of unit-basis vector $\mathbf{e}_i = \mathbf{h}_i/h_i$, we have that $\tilde{a}_i = h_i a_i$.
We can also introduce the *metric tensor* of the system defined as

$$g_{ij} = \mathbf{h}_i \cdot \mathbf{h}_j = h_i h_j \tag{115}$$

It is clear that, for an orthogonal basis, diagonal metric coefficients are the only non null elements of the metric tensor and they are equivalent to the *Lamè coefficients*, $h_i = \sqrt{g_{ii}}$. Finally we define

$$\sqrt{g} \equiv \sqrt{g_{11} g_{22} g_{33}} = h_1 h_2 h_3 \tag{116}$$

These are essentially all the elements needed to understand the form of the Braginskii equations in curvilinear toroidal geometry.
Here in the following we report also, without proof, the general curvilinear form of the differential operators which appear in the fluid equations. In the discussion presented in section 3.3.1, we always consider physical components and so there we omit the $\sim$ above each of them.

- ◇ Gradient of a scalar function Φ

$$\nabla\Phi = \frac{1}{h_i}\frac{\partial\tilde{\Phi}}{\partial q_i}\mathbf{e}_i \tag{117}$$

- ◇ Divergence of a vector field $\mathbf{A}$

$$\nabla \cdot \mathbf{A} = \frac{1}{\sqrt{g}}\frac{\partial}{\partial q_i}\left(\frac{\sqrt{g}}{h_i}\tilde{a}_i\right) \tag{118}$$

BIBLIOGRAPHY

[1] ADAS. *Atomic Data and Analysis Structure*. URL: http://www.adas.ac.uk/documentation.php/.

[2] U.S. Energy Information Administration. *Annual Energy Review*. URL: https://www.eia.gov/totalenergy/data/annual/.

[3] M. Baelmans. "Code improvements and applications of a two-dimensional edge plasma model for toroidal fusion devices." PhD thesis. Katholieke Universiteit Leuven, 1993.

[4] M. Baelmans, P. Börner, M. Blommaert, K. Ghoos, and W. Dekeyser. *Error assessment and code speed-up for SOLPS-ITER*. 2017. URL: https://core.ac.uk/download/pdf/154965661.pdf.

[5] M. Baeva, W.J. Goedheer, N.J. Lopes Cardozo, and D. Reiter. "B2-EIRENE simulation of plasma and neutrals in MAGNUM-PSI." In: *Journal of Nuclear Materials* 363-365 (2007). Plasma-Surface Interactions-17, pp. 330 –334.

[6] R. Balescu. *Transport processes in plasmas*. Vol. 1. Elsevier Science Publishers B. V, 1988.

[7] J. Bohdansky. "A universal relation for the sputtering yield of monatomic solids at normal ion incidence." In: *Nuclear Instruments and Methods in Physics Research Section B: Beam Interactions with Materials and Atoms* 2.1 (1984), pp. 587 –591.

[8] L. Boltzmann. *Weitere Studien über das Wärmegleichgewicht unter Gasmolekülen*. 1872.

[9] B. J. Braams. "Radiative Divertor Modelling for ITER and TPX." In: *Contributions to Plasma Physics* 36.2-3 (), pp. 276–281.

[10] B. J. Braams. "Computational Studies in Tokamak Equilibrium and Transport." PhD thesis. Rijksuniversiteit, Utrecht, 1986.

[11] S. I. Braginskii. "Transport Processes in a Plasma." In: *Reviews of Plasma Physics* 1 (1965), p. 205.

[12] H. Bufferand et al. "Numerical modelling for divertor design of the WEST device with a focus on plasma–wall interactions." In: *Nuclear Fusion* 55.5 (2015), p. 053025.

[13] S. Carli, R.A. Pitts, X. Bonnin, F. Subba, and R. Zanino. "Effect of strike point displacements on the ITER tungsten divertor heat loads." In: *Nuclear Fusion* 58.12 (2018), p. 126022.

[14] R. Chodura. "Plasma–wall transition in an oblique magnetic field." In: *The Physics of Fluids* 25.9 (1982), pp. 1628–1633.

[15] Nuclear Regulatory Commission. *Backgrounder on Tritium, Radiation Protection Limits, and Drinking Water Standards*. URL: https://www.nrc.gov/reading-rm/doc-collections/fact-sheets/tritium-radiation-fs.html.

[16] D. Coster, X. Bonnin, and M. Warrier. "Extensions to the SOLPS edge plasma simulation code to include additional surface interaction possibilities." In: *Physica Scripta* 2006 (May 2006), p. 9.

[17] Reiter D. *The EIRENE Code User Manual*. 1992.

[18] Reiter D. *The EIRENE Code User Manual*. Oct. 2018. URL: http://www.eirene.de/eirene.pdf.

[19] Reiter D. *The data file AMJUEL: Additional Atomic and Molecular Data for EIRENE*. Oct. 2018. URL: http://www.eirene.de/html/amjuel.html.

[20] Reiter D. *The data file HYDHEL: Atomic and Molecular Data for EIRENE based upon: Janev, Langer, Evans, Post, "Elementary Processes in Hydrogen-Helium Plasmas"*. Oct. 2018. URL: http://www.eirene.de/html/amjuel.html.

[21] A.S. Kukushkin M. Stanojevic X. Bonnin S. Voskoboynikov D.P. Coster O. Wenisch. *SOLPS-ITER User Manual*.

[22] Bonnin X. W. Lisgo S. A. Pitts R. Brunner D. Labombard B. L. Terry J. Dekeyser W. "SOLPS-ITER Modeling of the Alcator C-Mod Divertor Plasma." In: *Plasma and Fusion Research* 11 (Aug. 2016), pp. 1403103–1403103.

[23] EIRENE. *Atomic&Molecular Databases*. URL: http://www.eirene.de/html/a-m_data.html.

[24] EUROfusion. *The demonstration power plant: DEMO*. URL: https://www.euro-fusion.org/programme/demo/.

[25] Caneses J. F. "Helicon wave propagation and plasma equilibrium in high-density hydrogen plasma in converging magnetic fields." PhD thesis. Australian National University, 2015.

[26] George S. Fishman. *Monte Carlo: Concepts, Algorithms and Applications*. New York, NY, USA: Springer Verlag, 1996.

[27] J. P. Freidberg. *Plasma Physics and Fusion Energy*. 1st ed. Cambridge University Press, 2007. Chap. 4, pp. 69–73.

[28] J. P. Freidberg. *Ideal MHD*. 1st ed. Cambridge University Press, 2014.

[29] W Fundamenski. "Parallel heat flux limits in the tokamak scrape-off layer." In: *Plasma Physics and Controlled Fusion* 47.11 (2005), R163–R208.

[30] K. Ghoos, W. Dekeyser, G. Samaey, P. Börner, and M. Baelmans. "Accuracy and convergence of coupled finite-volume / Monte-Carlo codes for plasma edge simulations of nuclear fusion reactors." In: *Journal of Computational Physics* 322 (June 2016). DOI: 10.1016/j.jcp.2016.06.049.

[31] P. Helander and D.J. Sigmar. *Collisional Transport in Magnetized Plasmas*. Cambridge Monographs on Plasma Physics. Cambridge University Press, 2005.

[32] Betti R. Hurricane O.A. "Inertial-confinement fusion with lasers." In: *Nature Physics* 12 (May 2016), p. 435.

[33] A. D. Sakharov I. E. Tamm. *Theory of a Magnetic Thermonuclear Reactor, Part I, II and III*. 1991.

[34] J. D. Jackson. *Classical electrodynamics*. 3rd ed. New York, NY: Wiley, 1999.

[35] Langer W. D. Evans K. Post D. E. Janev R. K. *Elementary processes in hydrogen-helium plasmas: cross sections and reaction rate coefficients*. Springer series on atoms and plasmas. Springer, 1987.

[36] R. Janev and D. Reiter. *Collision Processes of Hydrocarbon Species in Hydrogen Plasmas: I. Methane Family*. URL: http://www.eirene.de/report_3966.pdf.

[37] R. Janev and D. Reiter. *Collision Processes of Hydrocarbon Species in Hydrogen Plasmas: II. Ethane and Propane Families*. URL: http://www.eirene.de/report_4005.pdf.

[38] Y. M. Jeon. "Development of a free-boundary tokamak equilibrium solver for advanced study of tokamak equilibria." In: *Journal of the Korean Physical Society* 67.5 (2015), pp. 843–853.

[39] K. Jesko, Y. Marandet, H. Bufferand, J.P. Gunn, H.J. van der Meiden, and G. Ciraolo. "Soledge2D- simulations of the Pilot-PSI linear plasma device compared to experimental data." In: *Contributions to Plasma Physics* 58.6-8 (2018), pp. 798–804.

[40] K. Ješko, Y. Marandet, H. Bufferand, J. P. Gunn, H. J. van der Meiden, and G. Ciraolo. "Studying divertor relevant plasmas in the Pilot-PSI linear plasma device: experiments versus modeling." In: *Plasma Physics and Controlled Fusion* 60.12 (2018), p. 125009.

[41] K. S. Krane. *Introductory Nuclear Physics*. John Wiley & Sons, 1987. Chap. 14, pp. 528–553.

[42] A.S. Kukushkin, H.D. Pacher, and R.A. Pitts. "Characteristics of divertor detachment for ITER conditions." In: *Journal of Nuclear Materials* 463 (2015). PLASMA-SURFACE INTERACTIONS 21, pp. 586 –590.

[43] A.S. Kukushkin, H.D. Pacher, V. Kotov, D. Reiter, D.P. Coster, and G.W. Pacher. "Effect of the dome on divertor performance in ITER." In: *Journal of Nuclear Materials* 363-365 (2007). Plasma-Surface Interactions-17, pp. 308 –313.

[44] J. D. Lawson. "Some Criteria for a Power Producing Thermonuclear Reactor." In: *Proceedings of the Physical Society B* 70 (Jan. 1957), pp. 6–10.

[45] A. W. Leonard. "Plasma detachment in divertor tokamaks." In: *Plasma Physics and Controlled Fusion* 60.4 (2018), p. 044001.

[46] E.M. Lifshitz, L.P. Pitaevskii, J.B. Sykes, and R.N. Franklin. *Physical Kinetics*. Vol. 10. Course of theoretical physics. Elsevier Science, 1995.

[47] Baelmans M. "Code improvements and applications of a two-dimensional edge plasma model for toroidal devices." PhD thesis. Katholieke Universiteit Leuven, 1994.

[48] Sala M. *Interaction between fusion-like boundary plasmas and nanostructured tungsten*. 2017.

[49] R. Marchand and M. Dumberry. "CARRE: a quasi-orthogonal mesh generator for 2D edge plasma modelling." In: *Computer Physics Communications* 96.2 (1996), pp. 232 –246.

[50] G.F. Matthews. "Plasma detachment from divertor targets and limiters." In: *Journal of Nuclear Materials* 220-222 (1995). Plasma-Surface Interactions in Controlled Fusion Devices, pp. 104 –116.

[51] Hazeltine R. D. Meiss J. D. *Plasma Confinemnet*. Addison-Wesley Publishing Company, 1992.

[52] R. L. Merlino. "Understanding Langmuir probe current-voltage characteristics." In: *American Journal of Physics* 75 (Dec. 2007), pp. 1078–1085.

[53] H. M. Mott-Smith and Irving Langmuir. "The Theory of Collectors in Gaseous Discharges." In: *Phys. Rev.* 28 (4 1926), pp. 727–763.

[54] D. Naujoksy. *Plasma-Material Interaction in Controlled Fusion*. Springer, 2006.

[55] D. R. Nicholson. *Introduction to Plasma Theory*. John Wiley & Sons, 1983.

[56] N. Ohno. "Plasma detachment in linear devices." In: *Plasma Physics and Controlled Fusion* 59.3 (2017), p. 034007.

[57] Ongena, J. "Fusion: A true challenge for an enormous reward." In: *EPJ Web of Conferences* 98 (2015), p. 05004.

[58] ITER Organization. *ITER - the way to new energy*. URL: https://www.iter.org.

[59] L. W. Owen, J. F. Caneses, J. Canik, J. D. Lore, C. Corr, B. Blackwell, X. Bonnin, and J. Rapp. "B2.5-Eirene modeling of radial transport in the MAGPIE linear plasma device." In: *Plasma Sources Science and Technology* 26.5 (2017), p. 055005.

[60] Decoster A. Markowich P.A. Perthame B. *Modeling of Collisions*. Èditiones scientifiques et médicales Elsevier, 1998.

[61] D.E. Post, R. Behrisch, and North Atlantic Treaty Organization. Scientific Affairs Division. *Physics of plasma-wall interactions in controlled fusion*. NATO ASI series: Physics. Plenum Press, 1986.

[62] J. Rapp et al. "The Material Plasma Exposure eXperiment MPEX: Predesign, development and testing of source concept." In: May 2015, pp. 1–8.

[63] J. Rapp, L.W. Owen, X. Bonnin, J.F. Caneses, J.M. Canik, C. Corr, and J.D. Lore. "Transport simulations of linear plasma generators with the B2.5-Eirene and EMC3-Eirene codes." In: *Journal of Nuclear Materials* 463 (2015). PLASMA-SURFACE INTERACTIONS 21, pp. 510 –514.

[64] D. Reiter, M. Baelmans, and P. Börner. "The EIRENE and B2-EIRENE Codes." In: *Fusion Science and Technology* 47.2 (2005), pp. 172–186.

[65] T.D. Rognlien, J.L. Milovich, M.E. Rensink, and G.D. Porter. "A fully implicit, time dependent 2-D fluid code for modeling tokamak edge plasmas." In: *Journal of Nuclear Materials* 196-198 (1992). Plasma-Surface Interactions in Controlled Fusion Devices, pp. 347 –351.

[66] V. Rozhansky, E. Kaveeva, P. Molchanov, I. Veselova, S. Voskoboynikov, D. Coster, G. Counsell, A. Kirk, and S. Lisgo. "New B2SOLPS5.2 transport code for H-mode regimes in tokamaks." In: *Nuclear Fusion* 49.2 (2009), p. 025007.

[67] V.A Rozhansky, S.P Voskoboynikov, E.G Kaveeva, D.P Coster, and R Schneider. "Simulation of tokamak edge plasma including self-consistent electric fields." In: *Nuclear Fusion* 41.4 (2001), pp. 387–401.

[68] Boyd T. J. M. Sanderson J. J. *The Physics of Plasmas*. Cambridge University Press, 2003. Chap. 2, pp. 12–41.

[69] Boyd T. J. M. Sanderson J. J. *The Physics of Plasmas*. Cambridge University Press, 2003. Chap. 1, pp. 7–9.

[70] R. Schneider, X. Bonnin, K. Borrass, D. Coster, H. Kastelewicz, D. Reiter, V. Rozhansky, and B. Braams. "Plasma Edge Physics with B2-Eirene." In: *Contrib. Plasma Phys.* 46 (Feb. 2006), pp. 3–191.

[71] V.D. Shafranov. In: *JETP Lett.* 33 (1957), p. 710.

[72] R. Simonini, A. Taroni, M. Keilhacker, G. Radford, J. Spence, G. Vlases, M.L. Watkins, and S. Weber. "Modelling impurity control at JET." In: *Journal of Nuclear Materials* 196-198 (1992). Plasma-Surface Interactions in Controlled Fusion Devices, pp. 369 –373.

[73] L. Spitzer. "The Stellarator Concept." In: *The Physics of Fluids* 1.4 (1958), pp. 253–264.

[74] P. C. Stangeby. *The Plasma Boundary in Magnetic Fusion Devices*. Taylor & francis, 2000.

[75] P.C. Stangeby and G.M. McCracken. "Plasma boundary phenomena in tokamaks." In: *Nuclear Fusion* 30.7 (1990), pp. 1225–1379.

[76] T. H. Stix. *Waves in Plasmas*. 1st ed. AIP-Press, 1992.

[77] M.V. Umansky, T.D. Rognlien, M.E. Fenstermacher, M. Borchardt, A. Mutzke, J. Riemann, R. Schneider, and L.W. Owen. "Modeling of localized neutral particle sources in 3D edge plasmas." In: *Journal of Nuclear Materials* 313-316 (2003), pp. 559 –563.

[78] Kotov V., Detlev R., and Andrey S. K. "Numerical study of the ITER divertor plasma with the B2-EIRENE code package." In: (Nov. 2007). URL: http://www-brs.ub.ruhr-uni-bochum.de/netahtml/HSS/Diss/KotovVladislav/diss.pdf.

[79] M. Wang. "Irradiated Assisted Corrosion of Stainless Steel in Light Water Reactors - Focus on Radiolysis and Corrosion Damage." In: (June 2013).

[80] R.C. Wieggers. "B2.5-Eunomia simulations of Pilot-PSI." PhD thesis. Department of Applied Physics, 2012.

[81] S. Wiesen et al. "The new SOLPS-ITER code package." In: *Journal of Nuclear Materials* 463 (2015). PLASMA-SURFACE INTERACTIONS 21, pp. 480 –484.

[82] L.Y. Xiang, M. Wischmeier, D. Coster, M. Bernert, H.Y. Guo, G.N. Luo, and ASDEX Upgrade team. "Modeling of argon seeding in ASDEX Upgrade H-mode plasma with SOLPS5.0." In: *Nuclear Materials and Energy* 12 (2017). Proceedings of the 22nd International Conference on Plasma Surface Interactions 2016, 22nd PSI, pp. 1146 –1151.

[83] D. R. Zhang, Y. P. Chen, X. Q. Xu, and T. Y. Xia. "Self-consistent simulation of transport and turbulence in tokamak edge plasma by coupling SOLPS-ITER and BOUT++." In: *Physics of Plasmas* 26.1 (2019), p. 012508.

[84] V.M. Zhdanov and G.A. Tirskii. "The use of the moment method to derive the gas and plasma transport equations with transport coefficients in higher-order approximations." In: *Journal of Applied Mathematics and Mechanics* 67.3 (2003), pp. 365 –388.